University of New Mexico
UNM Digital Repository

Physics & Astronomy ETDs | Electronic Theses and Dissertations

7-9-2009

InAs quantum dot vertical-cavity lasers

Alexander R. Albrecht

Follow this and additional works at: https://digitalrepository.unm.edu/phyc_etds

Recommended Citation

Albrecht, Alexander R.. "InAs quantum dot vertical-cavity lasers." (2009). https://digitalrepository.unm.edu/phyc_etds/2

This Dissertation is brought to you for free and open access by the Electronic Theses and Dissertations at UNM Digital Repository. It has been accepted for inclusion in Physics & Astronomy ETDs by an authorized administrator of UNM Digital Repository. For more information, please contact disc@unm.edu.

Alexander R. Albrecht

Candidate

Physics and Astronomy

Department

This dissertation is approved, and it is acceptable in quality and form for publication on microfilm:

Approved by the Dissertation Committee:

, Chairperson

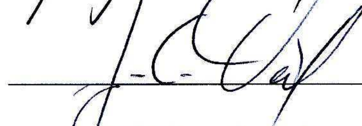

Accepted:

Dean, Graduate School

Date

InAs Quantum Dot Vertical-Cavity Lasers

by

Alexander R. Albrecht

M.S., Physics, University of New Mexico, 2001

DISSERTATION

Submitted in Partial Fulfillment of the
Requirements for the Degree of

Doctor of Philosophy
Physics

The University of New Mexico

Albuquerque, New Mexico

May, 2009

©2009, Alexander R. Albrecht

Dedication

To my parents.

Acknowledgments

The research presented in this dissertation would not have been possible without the help from countless people, first and foremost my advisor, Prof. Kevin J. Malloy. I thank him for his insight, guidance, support and great deal of patience over the years.

I would like to thank the other members of my dissertation committee, Prof. Ganesh Balakrishnan, Prof. Jean-Claude Diels, and Prof. Mansoor Sheik-Bahae for their help — especially during the last part of this work — and their constructive comments about this manuscript.

This dissertation would not have been possible without the assistance from Prof. Andreas Stintz, who not only grew every single semiconductor sample investigated, but also taught me a lot about MBE growth and maintenance in the process.

Prof. James A. Lott is acknowledged for sharing his expertise on the subject and even sponsoring a visit to his laboratory.

Special thanks to Prof. Luke F. Lester for providing the BBO crystal used in the frequency-doubling experiments.

Several members of Prof. Malloy's research group deserve credit: Felix T. Jaeckel for his assistance in countless projects, from custom electronics and setups to programming and proofreading. Chi Yang for his help during long hours of cleanroom work. Thanks also to previous students Dr. Thomas J. Rotter, Dr. Alexander A. Ukhanov, Dr. P. Dan Popescu, and Dr. Giovanni P. Donati for passing on their knowledge from years of experience.

My thanks go to the fantastic CHTM staff: Ron Kay for designing and building several pieces of quality electronics and saving big amounts of time and money by repairing others. Beth Fuchs, Karen DeZetter, Douglas Wozniak, and Steven Wawrzyniec for keeping the cleanroom running. Dan Bryant and crew for keeping the building in perfect shape and supplying the labs with any utilities imaginable. Finally, the team in the front office for keeping money and orders flowing in the right direction.

InAs Quantum Dot

Vertical-Cavity Lasers

by

Alexander R. Albrecht

ABSTRACT OF DISSERTATION

Submitted in Partial Fulfillment of the
Requirements for the Degree of

Doctor of Philosophy
Physics

The University of New Mexico

Albuquerque, New Mexico

May, 2009

InAs Quantum Dot

Vertical-Cavity Lasers

by

Alexander R. Albrecht

M.S., Physics, University of New Mexico, 2001

Ph.D., Physics, University of New Mexico, 2009

Abstract

Edge-emitting semiconductor lasers with self-assembled InAs quantum dot (QD) active regions have demonstrated excellent device performance, including low sensitivity to operating temperature and record-low thresholds. In this dissertation, the application of QDs in vertical-cavity lasers (VCLs) is investigated. QDs can reach an emission wavelength up to 1300 nm on GaAs substrate.

Key design and device processing issues are discussed and vertical-cavity surface-emitting lasers (VCSELs) with both optical and electrical excitation are fabricated. VCSEL diodes with distributed Bragg reflectors (DBRs) formed by selective wet oxidation of AlAs, as well as standard GaAs/AlGaAs mirrors were processed. The latter performed better due to an increased number of QD layers in the cavity.

Continuous wave (CW) operation of InAs QD VCSEL diodes with 1 mW output power and threshold current densities below 500 Acm^{-2} were achieved.

Replacing one of the DBRs with an external spherical mirror, vertical-external-cavity surface-emitting lasers (VECSELs) allow the lateral dimensions of the device active region to be increased significantly, yielding high output power while still retaining single mode operation. Pumped by widely available high power diode lasers, QD VECSELs with CW output powers close to 400 mW were demonstrated with threshold pump power densities below 1 kWcm^{-2}.

Since the VECSEL cavity extends into free space, additional optical components can be integrated. By using a non-linear β-Barium Borate (BBO) inside the cavity, we were able to frequency-double the QD emission to produce visible red light, which could be utilized for the red channel of full-color laser projection applications. Despite suboptimal cavity design and minimal heatsinking, output powers over 10 mW at a wavelength of 630 nm were achieved.

Contents

List of Figures **xiii**

List of Tables **xxi**

Glossary **xxii**

1 Introduction **1**

References **4**

2 Design Considerations for Quantum Dot Vertical-Cavity Lasers **6**

2.1 Introduction 6

2.2 Use of Quantum Dots in Vertical-Cavity Active Regions 7

2.2.1 InAs Quantum Dots 7

2.2.2 Strain 9

2.2.3 Threshold Gain Estimate 14

2.3 DBR Design 15

2.3.1 Semiconductor DBR 16
2.3.2 Dielectric DBR 20
2.3.3 Oxide DBR 21
2.4 Conclusions 28

References 29

3 Quantum Dot Vertical-Cavity Surface-Emitting Laser 32

3.1 Introduction 32
3.2 Optically Pumped VCSEL 34
3.2.1 Design 35
3.2.2 Processing 35
3.2.3 Experimental Setup 36
3.2.4 Experimental Results 38
3.3 Oxide DBR Electrically Injected VCSEL 41
3.3.1 Design 41
3.3.2 Processing 44
3.3.3 Experimental Setup 48
3.3.4 Experimental Results 51
3.4 Semiconductor DBR Electrically Injected VCSEL 53
3.4.1 Design 53

3.4.2 Processing 56

3.4.3 Experimental Setup 57

3.4.4 Experimental Results 59

3.5 Conclusions 69

References **72**

4 Quantum Dot Vertical-External-Cavity Surface-Emitting Laser **75**

4.1 Introduction 75

4.2 VECSEL Design 77

4.2.1 Gain Mirror 78

4.2.2 External Cavity 81

4.3 Experimental Results 85

4.3.1 Optical Wafer Characterization 85

4.3.2 Output Power Characteristics 87

4.3.3 Spectral Properties 96

4.3.4 Lasing Mode 99

4.3.5 Polarization 100

4.3.6 Temperature Dependent Properties 102

4.3.7 Tuning by Position on the Wafer 107

4.3.8 Intra-Cavity Frequency Doubling 110

4.4 Conclusions 115

References **117**

5 Conclusions **121**

A ICP Reflectance Monitor **124**

A.1 Introduction 124

A.2 Reflectometry 125

A.3 Experimental Setup 126

A.4 Examples 127

A.5 Standard Operating Procedure 130

References **132**

B Oxidation Furnace Standard Operating Procedure **133**

C Silicon CCD Spectral Response **138**

List of Figures

2.1 Photoluminescence spectra of DWELL layers at for different wavelengths. 8

2.2 Temperature dependence of peak luminescence wavelength from the 1250 nm (at room temperature) QD sample. The solid line indicates a linear fit with a slope of 0.4 nmK^{-1}. 9

2.3 Critical thickness h_c for $Ga_{1-x}In_xAs$ grown on GaAs substrate. . . . 10

2.4 Calculated reflectance spectrum for 27 period GaAs/AlAs DBR at 1300 nm. 17

2.5 Reflectance measurement during ICP etch of semiconductor DBR showing non-uniformity of layer thickness due to drift in MBE growth rates. 19

2.6 Calculated reflectance spectrum for seven period MgF_2/ZnSe DBR at 1300 nm. 20

2.7 Photomicrograph of damage to a dielectric DBR due to the incident focused pump laser. 22

2.8 Calculated reflectance spectrum for seven period AlO_x/GaAs DBR at 1300 nm. 23

2.9 Schematic diagram of wet oxidation system. 24

2.10 Layer structure of a digital alloy graded interface from GaAs to AlAs. The red dots indicate the average composition for each period. . . . 25

2.11 Photomicrograph of oxidation front (appears green in this image as result of the Nomarski interference contrast microscopy technique used) at the corner of a cleaved sample. 26

2.12 Oxidation rate from 30 minute oxidation as function of Al content in the AlGaAs layer for both wet oxidation systems. 27

3.1 Refractive index n and calculated electric field $|E|^2$ for the optically pumped VCSEL sample. The digitally graded DBR interfaces have been omitted for clarity. 36

3.2 Modeled and measured reflectance spectra for optically pumped VCSEL sample after oxidation. 37

3.3 Schematic diagram of optically pumped VCSEL setup. 38

3.4 Optically pumped VCSEL output power as function of incident pump power, both corrected for the losses at the beam splitter, at a heatsink temperature of 10°C. 39

3.5 Optically pumped VCSEL lasing spectra for different pump powers at a heatsink temperature of 10°C. 40

3.6 Maximum optically pumped VCSEL output power as function of the heatsink temperature. 40

3.7 Optically pumped VCSEL lasing spectra for different heatsink temperatures. 41

3.8 Refractive index n and calculated electric field $|E|^2$ for electrically injected oxide DBR VCSEL. The digital alloys and graded interfaces have been omitted for clarity. 42

3.9 Layer structure and index of refraction profile of oxide DBR VCSEL cavity. The digital alloys and graded interfaces have been omitted for clarity. 43

3.10 Schematic diagrams of VCSEL processing steps. 46

3.11 Schematic diagrams of VCSEL processing steps. 47

3.12 Photomicrographs of oxidation test samples. 49

3.13 Photomicrograph of oxidized test structure, the numbers included on the sample indicate mesa size in micron. 50

3.14 Photomicrograph of oxide DBR VCSEL diode after processing. . . . 50

3.15 Output power and voltage as function of current for oxide DBR VCSEL test structure (no top DBR). 52

3.16 Electroluminescence spectrum from oxide DBR VCSEL test structure (no top DBR). 52

3.17 Refractive index n and electric field $|E|^2$ of the semiconductor DBR VCSEL sample. 55

3.18 Refractive index n and electric field $|E|^2$ of the semiconductor DBR VCSEL sample, magnified view of cavity, showing placement of the DWELL layers. 55

3.19 IR ($\lambda > 900$ nm) photomicrograph of semiconductor DBR VCSEL oxide aperture. 57

3.20 Photomicrograph of two semiconductor DBR VCSEL diodes after processing. 58

3.21 SEM image of wire-conded semiconductor DBR VCSEL array. . . . 58

3.22 FTIR reflectance spectra as function of the position on the semiconductor DBR VCSEL wafer. 60

3.23 Wavelength of cavity mode as function of position on the wafer, measured radially from the center of the wafer. 61

3.24 Photomicrograph of two VCSEL devices, with the right one lasing. The dark, out of focus object in the top right corner is the probe tip used to inject the current. 62

3.25 Photomicrograph of VCSEL device operating below threshold. The size of the oxide aperture is clearly visible. 62

3.26 Output power and voltage as function of current for 4 μm^2 aperture device from wafer A. 63

3.27 Lasing spectra for 4 μm^2 aperture device from wafer A. 63

3.28 Output power and voltage as function of current for 240 μm^2 aperture device 25 mm from the center of wafer A. 65

3.29 Lasing spectra for 240 μm^2 aperture device 25 mm from the center of wafer A. 65

3.30 Output power and voltage as function of current for 225 μm^2 aperture device 32 mm from the center of wafer A. 66

3.31 Lasing spectra for 225 μm^2 aperture device 32 mm from the center of wafer A. 66

3.32 Output power and voltage as function of current for 18 μm^2 aperture device from wafer B. 67

3.33 Lasing spectra for 18 μm^2 aperture device from wafer B. 67

3.34 Threshold current density j_{th} as function of current aperture area for a number of devices from both wafers. 68

3.35 VCSEL output power vs. current for [110] and [$1\overline{1}0$] polarization direction, showing a roughly 20:1 ratio. 69

3.36 VCSEL output power vs. current for heatsink temperatures from 0°C to 75°C. 70

4.1 Schematic diagram of a VECSEL. 77

4.2 Refractive index n and electric field $|E|^2$ of the 4x3 DWELL sample. Note that only four of the 30 bottom DBR pairs are shown. 80

4.3 Refractive index n and electric field $|E|^2$ of the 12 DWELL RPG sample. Note that only four of the 30 bottom DBR pairs are shown. 80

4.4 Dimensions of the VECSEL cavity. 81

4.5 Calculated beam waist w_1 as function of cavity length d for a $R = 25$ mm external mirror and a wavelength of $\lambda = 1250$ mm. 84

4.6 Calculated beam waist w_1 as function of cavity length d for a $R = 250$ mm external mirror and a wavelength of $\lambda = 1250$ mm. 84

4.7 Reflectance spectra for the external mirrors/output couplers used in VECSEL experiments. 85

4.8 Comparison between calculated and measured reflectance spectra as well as PL spectrum measured at room temperature and low excitation power for 4x3 DWELL VECSEL. 86

4.9 FTIR reflectance spectra as function of the position on the 4x3 DWELL VECSEL wafer. 88

4.10 VECSEL output power vs. pump power for Ti:Sapphire pumped operation for the 4x3 DWELL sample. 90

4.11 VECSEL output power vs. pump power for Ti:Sapphire pumped operation for the RPG sample. 90

4.12 VECSEL output power vs. pump power for diode-pumped operation for the 4x3 DWELL sample and 99.5% external mirror. 91

4.13 VECSEL output power vs. pump power for diode-pumped operation for the RPG sample and 99.5% external mirror. 91

4.14 VECSEL output power vs. pump power for diode-pumped operation for the 4x3 DWELL sample and 99.0% external mirror. 92

4.15 VECSEL output power vs. pump power for diode-pumped operation for the RPG sample and 99.0% external mirror. 92

4.16 Lasing spectra for the RPG structure at 0°C, using the 99.0% external mirror, for different pump power levels. 97

4.17 Photographs of the fundamental VECSEL lasing mode. The plots are cross-sections through the intensity maximum with Gaussian fits. 99

4.18 Photographs of higher order VECSEL lasing modes created by slightly adjusting pump spot or external mirror location. 101

4.19 VECSEL output power vs. pump power for [110] and [$1\bar{1}0$] polarization direction, showing a roughly 100:1 ratio. 102

4.20 VECSEL output power vs. pump power for the 4x3 DWELL sample and 99.0% external mirror at different temperatures. 103

4.21 VECSEL output power vs. pump power for the RPG sample and 99.0% external mirror at different temperatures. 103

4.22 VECSEL threshold power density at different temperatures. 104

4.23 VECSEL differential efficiency at different temperatures. 105

4.24 Maximum VECSEL output power at different temperatures. 106

4.25 Lasing spectra from RPG VECSEL at 1.28 W pump power for different heatsink temperatures. 106

4.26 VECSEL spectra for different positions across the wafer of the 4x3 DWELL sample. 108

4.27 VECSEL spectra for different positions across the wafer of the RPG sample. 108

4.28 VECSEL output power vs. pump power for different positions across the wafer of the 4x3 DWELL sample. 109

4.29 VECSEL output power vs. pump power for different positions across the wafer of the RPG sample. 109

4.30 VECSEL lasing wavelength as a function of position on the wafer. . 110

4.31 Maximum VECSEL output power as a function of position on the wafer. 110

4.32 Schematic drawing of SHG area overlaid on a photograph of IR lasing mode in the VECSEL cavity without BBO crystal present. 112

4.33 VECSEL IR and SH output power vs. pump power for the RPG structure. 113

4.34 Spectrum of SH output at 630 nm. 113

4.35 Possible VECSEL cavity design for efficient SHG. 114

A.1 Schematic diagram of laser beam reflected of sample surface and internal interfaces. Note that the actual measurement is performed under normal incidence, the angle was added for clarity. 126

A.2 Schematic diagram of ICP reflectance monitor. 127

A.3 26 AlAs/GaAs DBR pairs designed for a wavelength of 1250 nm showing non-uniformity of layer thickness due to drift in MBE growth rates. 128

A.4 Simulation for AlAs/GaAs DBR designed for 980 nm. 129

A.5 Reflectance measurements from etching two different thickness MnAs layers on top of GaAs substrate. While no simulation was available, it seems quite clear, where the metallic MnAs layer ends and the substrate starts. Also, since sample A requires a longer etch, it can be inferred that its MnAs thickness is greater than in sample B. . . 129

C.1 Spectral response of Si CCD used in the Ikegami ICD-4220 camera. 138

List of Tables

2.1 Comparison of average In content and critical thickness for DWELL layers with QD emission of 1250 nm and 1300 nm. 12

2.2 Comparison of average In content $\overline{x}$, cavity thickness L, and critical thickness h_c for different arrangements of k DWELL layers in a $l\lambda/2$ cavity. 13

2.3 Comparison of confinement factor and threshold gain per QD layer for different arrangements of three DWELL layers at 1300 nm and twelve DWELL layers at 1250 nm. 15

4.1 Summary of VECSEL lasing parameters extracted from Figs. 4.10–4.15. Values for a heat sink temperature of 0°C are shown in blue, for 20°C in red. 93

B.1 Historical documents suggest that these temperature controller setting result in the given temperatures, with good uniformity throughout the furnace. 137

Glossary

Abbreviations

a.u.	Arbitrary units
AR	Antireflection
BBO	β-Barium Borate
CW	Continuous wave
DBR	Distributed Bragg reflector
DFB	Distributed feedback (laser)
DI	Deionized (water)
div	Division
DPSS	Diode pumped solid-state (laser)
DWELL	Dots-in-a-well
FTIR	Fourier transform infrared (spectrometry)
ICP	Inductively coupled plasma (etcher)

IR	Infrared
MBE	Molecular beam epitaxy
ND	Neutral Density (filter)
PECVD	Plasma-enhanced chemical vapor deposition
PL	Photoluminescence
PR	Photoresist
QD	Quantum dot
QW	Quantum well
RHEED	Reflection high-energy electron diffraction
RPG	Resonant periodic gain
SEM	Scanning electron microscope
SESAM	Semiconductor saturable absorber mirror
SH	Second harmonic
SHG	Second harmonic generation
SMF	Single-mode fiber
TE	Thermoelectric (cooler)
VCL	Vertical-cavity laser
VCSEL	Vertical-cavity surface-emitting laser
VECSEL	Vertical-external-cavity surface-emitting laser
XRD	X-ray diffraction

Roman symbols

A, B, C, D	Components of the transmission matrix
a	Lattice constant
a_0	Lattice constant of substrate
b	Magnitude of Burgers vector
c	Speed of light
d	Length of external cavity
d_{QD}	Thickness of InAs quantum dot layer
d_{QW}	Thickness of quantum well
e	Electron charge
E	Electrical field strength
f	Lattice misfit
g_{th}	Threshold gain
h	Planck's constant
h_c	Critical thickness
I	Current
I_P	Pump intensity
j_{th}	Threshold current density
k	Number of DWELL layers

l	Cavity length in units of $\lambda/2n$
L	Cavity length in VCSELs, subcavity length in VECSELs
n	Index of refraction
n, p	Doping concentration
N	Number of photons
m	Number of DBR pairs
P	Pump power
P_{th}	Threshold power density
q	Complex beam parameter
R	Radius of curvature of external mirror
R_{gm}	Geometric mean of mirror reflectance values
R_{DBR}	Reflectance of DBR stack
$\mathbf{T}$	Transmission matrix
w	Gaussian beam waist
x	Material composition
x_{QD}	Material composition of quantum dot
x_{QW}	Material composition of quantum well
$\overline{x}$	Average material composition
x, y, z	Cartesian coordinates

Greek symbols

α — Absorption coefficient

α_{diff} — Diffraction loss

α_{in} — Internal loss

β — Angle between Burgers vector and dislocation line

Γ — Confinement factor

θ — Phase-matching angle

λ — Wavelength

λ_b — In-plane angle between Burgers vector and dislocation line

ν — Poisson ratio

Chapter 1

Introduction

Vertical-cavity surface-emitting lasers (VCSELs) were first proposed and fabricated in the late 1970s [1]. In contrast to the more common edge-emitting lasers, they have an extremely small cavity volume, requiring high optical gain and/or high mirror reflectivity, and in turn achieve extremely low threshold currents. VCSELs can be fabricated monolithically, allow for the fabrication of one- or two-dimensional arrays, which can be tested on wafer scale before separating the devices. The short cavity length results in wide spacing of cavity modes, therefore devices operate in a single longitudinal mode with a low divergence circular beam [2]. The development of GaAs based VCSELs [3] sparked rapid progress due to a variety of possible emission wavelengths from AlGaAs or GaInAs quantum wells (QWs). At the same time, AlGaAs/GaAs distributed Bragg reflectors (DBRs) could be monolithically fabricated on the substrate, which not only allowed for highly reflective mirrors because of the relatively large variation in refractive index, but also injection of current through the low electrical resistance DBRs [4].

The idea to use quantum confined structures like quantum wires or quantum dots (QDs) as gain materials in semiconductor lasers was first presented in 1976 [5].

Self-assembled growth of InAs QDs by molecular beam epitaxy (MBE) [6] was a key element in manufacturing dense arrays of uniform QDs. By embedding the dots in a well (DWELL) of higher bandgap GaInAs, device performance was significantly improved in the late 1990s, resulting in — at that time — record-low threshold current densities for any semiconductor lasers [7]. Other advantages of QD active regions include low temperature sensitivity, small linewidth enhancement factor, as well as the ability to extend the lasing wavelength for GaAs-based structures to 1300 nm [8].

Using a QD active region in a VCSEL promises to combine the advantages of both, creating a device with low threshold current, low temperature sensitivity, and good modulation properties at a wavelength of 1300 nm. This is desirable for fiber-optic communications, since the dispersion in optical fibers is at its minimum in that wavelength range. First promising results, including pulsed operation of a 1300 nm QD VCSEL, were published by other groups in 2000 [9], shortly before the beginning of this work.

Another interesting application is the generation of red light: While emission wavelengths of 675 nm and longer have been achieved in the GaInP/AlGaInP/GaAs material system [10], the human eye is more sensitive to shorter wavelengths between 600 and 650 nm. With QDs, 1200–1300 nm emission can be generated and then frequency-doubled using a nonlinear optical crystal. VCSELs typically do not have the required output powers for practical applications, like full-color laser projection systems, due to their limited lateral dimensions. By replacing the top DBR of a VCSEL with a concave mirror in some distance, a vertical-external-cavity surface-emitting laser (VECSEL) is created [11], where the lateral mode size is controlled by the radius of curvature of the external mirror and its distance from the active region. Not only does that increase the output power significantly, it also allows the nonlinear crystal to be placed inside the laser cavity, where the higher optical

intensities greatly increase the efficiency of frequency doubling.

In this dissertation, some implications of the incorporation of QDs in vertical-cavity lasers (VCLs) are discussed in chapter 2, including the amount of strain introduced by growing multiple InAs DWELL layers, and different material choices for DBRs are compared. Chapter 3 focuses on QD VCSELs. Optically pumped devices are designed and successfully tested. Layer structure and mask design for an electrically injected VCSEL diode with oxide DBRs and associated processing steps are discussed. An all semiconductor approach is also investigated, which allows for faster device processing. Two different VECSEL wafers and their performance are compared in chapter 4, including experiments with frequency-doubling. Conclusions are summarized in chapter 5.

References

[1] H. Soda, K.-i. Iga, C. Kitahara, and Y. Suematsu. GaInAsP/InP Surface Emitting Injection Lasers. *Japanese Journal of Applied Physics*, 18:2329–2330, December 1979.

[2] K. Iga, F. Koyama, and S. Kinoshita. Surface emitting semiconductor lasers. *Quantum Electronics, IEEE Journal of*, 24(9):1845–1855, Sep 1988.

[3] K. Iga, S. Kinoshita, and F. Koyama. Microcavity GalaAs/GaAs surface-emitting laser with $I_{th} = 6$ mA. *Electronics Letters*, 23(3):134–136, 29 1987.

[4] S. A. Chalmers, K. L. Lear, and K. P. Killeen. Low resistance wavelength-reproducible p-type (Al,Ga)As distributed Bragg reflectors grown by molecular beam epitaxy. *Applied Physics Letters*, 62(14):1585–1587, 1993.

[5] Raymond Dingle, Charles Howard Henry. Quantum effects in heterostructure lasers. US Patent Number 3982207, September 1976.

[6] L. Goldstein, F. Glas, J. Y. Marzin, M. N. Charasse, and G. Le Roux. Growth by molecular beam epitaxy and characterization of InAs/GaAs strained-layer superlattices. *Applied Physics Letters*, 47(10):1099–1101, 1985.

[7] G. Liu, A. Stintz, H. Li, K.J. Malloy, and L.F. Lester. Extremely low room-temperature threshold current density diode lasers using InAs dots in $In_{0.15}Ga_{0.85}As$ quantum well. *Electronics Letters*, 35(14):1163–1165, Jul 1999.

[8] D. L. Huffaker, G. Park, Z. Zou, O. B. Shchekin, and D. G. Deppe. 1.3 μm room-temperature GaAs-based quantum-dot laser. *Applied Physics Letters*, 73(18):2564–2566, 1998.

[9] J.A. Lott, N.N. Ledentsov, V.M. Ustinov, N.A. Maleev, A.E. Zhukov, A.R. Kovsh, M.V. Maximov, B.V. Volovik, Zh.I. Alferov, and D. Bimberg. InAs-InGaAs quantum dot VCSELs on GaAs substrates emitting at 1.3 μm. *Electronics Letters*, 36(16):1384–1385, 2000.

[10] Jennifer Hastie, Stephane Calvez, Martin Dawson, Tomi Leinonen, Antti Laakso, Jari Lyytikäinen, and Markus Pessa. High power CW red VECSEL with linearly polarized TEM00 output beam. *Opt. Express*, 13(1):77–81, 2005.

[11] M. Kuznetsov, F. Hakimi, R. Sprague, and A. Mooradian. High-power (>0.5-W CW) diode-pumped vertical-external-cavity surface-emitting semiconductor lasers with circular TEM00 beams. *Photonics Technology Letters, IEEE*, 9(8):1063–1065, Aug. 1997.

Chapter 2

Design Considerations for Quantum Dot Vertical-Cavity Lasers

2.1 Introduction

Semiconductor devices with QD gain media were first realized using regrowth on patterned substrates [1], however the etch process resulted in poor material quality due to structural defects. Self-assembled growth by MBE of InAs QDs on GaAs substrate [2] dramatically improved the device performance [3]. By embedding the QDs in a strained GaInAs quantum well [4] carrier capture into the QDs is greatly increased. This led to edge-emitting lasers with vastly improved properties, including lower threshold current densities than any other semiconductor laser at the time [5].

In an edge-emitting laser, the light travels along the gain medium in a cavity that is typically several 100 μm to a few mm long. In this configuration, even a single DWELL layer can provide enough gain to support lasing. In a vertical cavity, the

emission is perpendicular to the QD layer, limiting the amount of gain that can be achieved in one round trip. To overcome this, the number of active layers can be increased, and at the same time, the mirror loss is decreased by using highly reflective DBRs instead of the cleaved facets used in edge-emitting lasers.

In section 2.2, some design considerations for QD active regions in VCLs will be discussed, while section 2.3 focuses on possible DBR materials and their implications on device design and manufacturing.

2.2 Use of Quantum Dots in Vertical-Cavity Active Regions

2.2.1 InAs Quantum Dots

When InAs with a lattice constant of 6.0583 Å is grown on GaAs with a substantially lower lattice constant of 5.6533 Å, only a very thin layer can be grown before too much strain accumulates. It was found that under certain growth conditions the strain is not relieved by forming dislocations, but rather by entering a three-dimensional growth regime [2], referred to as Stranski-Krastanov growth [6]. The InAs "islands" formed in this growth mode are called self-assembled QDs with dimensions on the order of a few nanometers. The band-offset and the small dimensions lead to few, well separated energy levels per dot, resulting in 3D confinement of carriers and a much reduced density of states compared to bulk semiconductors or even quantum wells. This promises advantages for QD-based lasers, like low transparency and threshold current densities as well as reduced temperature sensitivity.

The emission wavelength of the dots can be influenced by carefully tuning several parameters during crystal growth, including the amount of InAs deposited, the com-

position of the surrounding material, and the growth temperature. Previous work [7] has shown that placing the QDs inside an GaInAs QW greatly increases performance due to improved carrier capture and reduced thermionic emission at higher temperatures. At the same time, the wavelength is shifted to the technologically important 1250 – 1300 nm range.

Fig. 2.1 shows photoluminescence spectra from two test samples: The first is for an emission wavelength of 1250 nm. A total of 2.56 monolayers of InAs were deposited inside a 7 nm $Ga_{0.85}In_{0.15}As$ QW at a growth temperature of 480°C. For the 1300 nm sample, the InAs amount was increased to 2.67 monolayers inside a 8.2 nm QW, grown at 470°C.

The temperature dependence of the VCL gain medium is of great importance in the laser design. To determine the wavelength shift of the QD gain peak, temperature dependent photoluminescence experiments were performed on the 1250 nm QD sample. Peak wavelength as function of sample temperature is plotted in Fig. 2.2. The linear fit to the data indicates a slope of 0.4 nmK^{-1}, which agrees with the

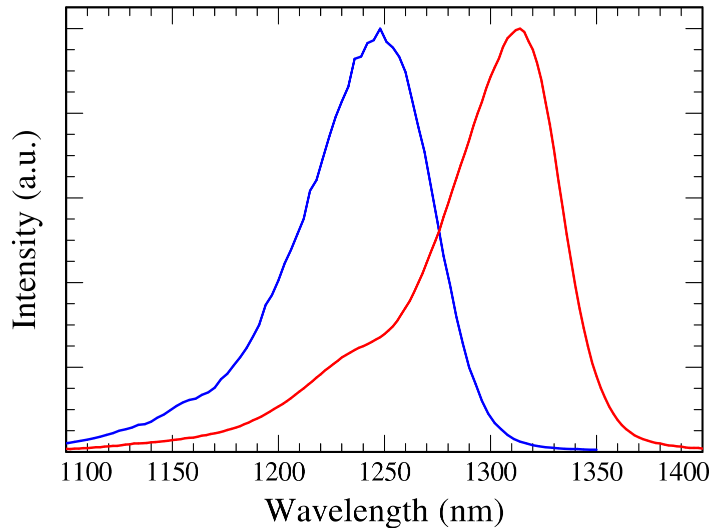

Figure 2.1: Photoluminescence spectra of DWELL layers at for different wavelengths.

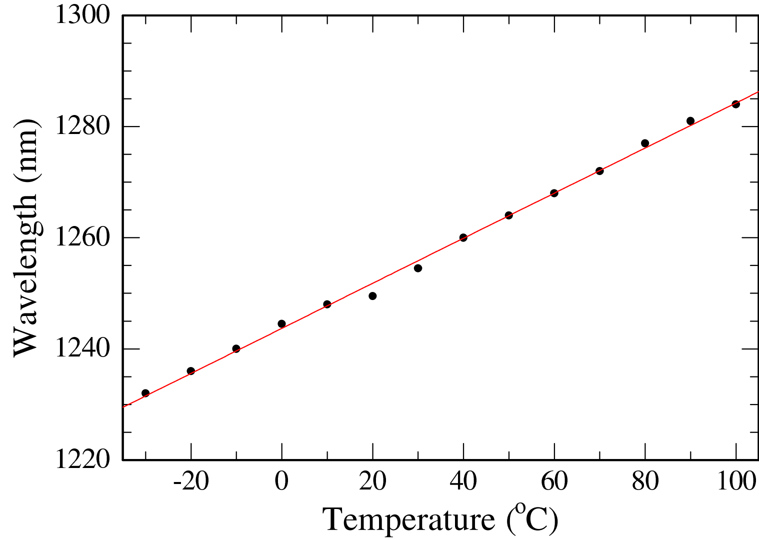

Figure 2.2: Temperature dependence of peak luminescence wavelength from the 1250 nm (at room temperature) QD sample. The solid line indicates a linear fit with a slope of 0.4 nmK^{-1}.

bandgap shrinkage of InAs.

2.2.2 Strain

Strain caused by the lattice mismatch between the GaAs substrate and InAs is essential for the formation of the QDs. However, if too much mechanical strain accumulates, it becomes thermodynamically favorable to form structural defects (dislocations) in the epitaxial film, significantly reducing material quality. These defects enhance non-radiative recombination processes and degrade device performance.

Thermodynamic equilibrium considerations of the energies of a strained coherent interface compared to the formation of dislocations, as proposed by Matthews and Blakeslee [8], lead to an equation for the critical thickness $h_{c,M\&B}$, beyond which

misfit dislocations are expected to form [9]:

$$h_{c,M\&B} = \frac{b}{8\pi f \cos\lambda_b}\left(\frac{1-\nu\cos^2\beta}{1+\nu}\right)\ln\left(\frac{4h_{c,M\&B}}{b}\right) \tag{2.1}$$

Here, β is the angle between the Burgers vector and the dislocation line, $b\cos\lambda_b$ is the component of the Burgers vector at the in-plane angle λ_b to the dislocation line that acts to relieve the lattice misfit. ν is the Poisson ratio, defined as the negative of the ratio between the lateral and longitudinal strains when the material is subjected to uniaxial longitudinal stress. For an epitaxial layer with lattice constant a grown on a substrate of lattice constant a_0, the lattice misfit is

$$f = \frac{a-a_0}{a_0} \tag{2.2}$$

In our case, the substrate is GaAs, with a lattice constant of $a_0 = 5.6533$ Å and Poisson ratio $\nu = 0.312$ [10]. The lattice constant of $Ga_{1-x}In_xAs$ is $a = a_0 + 0.405x$ Å. Assuming a dislocation with $\lambda_b = \beta = 60°$, Eq. 2.1 can numerically be solved as a function of the In content x. The result is plotted in Fig. 2.3 using a black line.

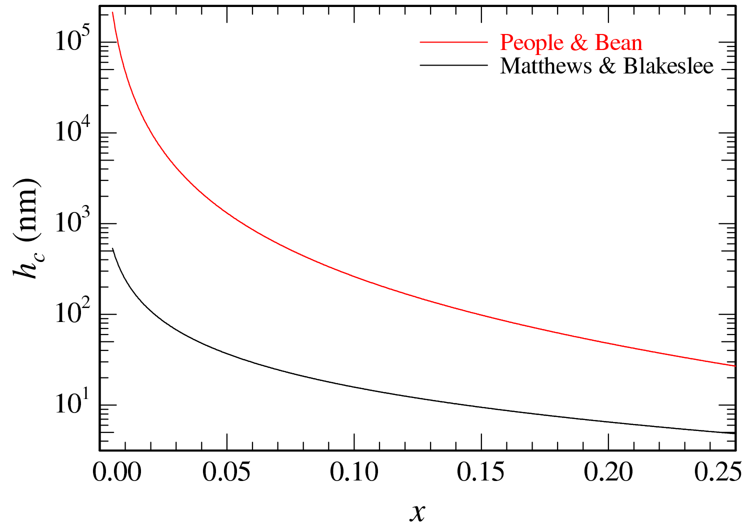

Figure 2.3: Critical thickness h_c for $Ga_{1-x}In_xAs$ grown on GaAs substrate.

For small misfits it has been found that even layers far beyond the critical thickness predicted by Matthews and Blakeslee can be grown defect-free. To better model this behavior, People and Bean [11] took a different approach, which considers the energy associated with the generation of interfacial misfit dislocations. The expression for the critical thickness in this case becomes

$$h_{c,P\&B} = \frac{b^2}{12\sqrt{2}\pi a f^2}\left(\frac{1-\nu}{1+\nu}\right)\ln\left(\frac{h_{c,P\&B}}{b}\right) \tag{2.3}$$

and is shown as the red line in Fig. 2.3.

For an analysis of strain and critical thickness in our laser structure, we first consider a DWELL layer: During MBE growth, a thin layer of InAs is deposited first, followed by the first part of the GaInAs QW. The dots are then formed by deposition of more InAs, and after a short growth interruption capped by the remainder of the QW. We can calculate the average In content $\overline{x}_{DWELL}$ as

$$\overline{x}_{DWELL} = \frac{x_{QD}d_{QD} + x_{QW}d_{QW}}{d_{QD} + d_{QW}} \tag{2.4}$$

where $x_{QD} \equiv 1$ and d_{QD} is the total amount of InAs deposited, and x_{QW} is the composition of the QW and d_{QW} its total thickness. We can then check with Eq. 2.1, how the thickness of the DWELL layer $d_{DWELL} = d_{QD} + d_{QW}$ compares to the critical thickness for an GaInAs layer of composition $\overline{x}_{DWELL}$.

The exact composition of a DWELL layer depends on the desired wavelength of the QD emission, and has been optimized using several test structures. The values for typical DWELL layers for a wavelength λ of 1250 nm and 1300 nm, as well as the corresponding values of the critical thickness are shown in table 2.1.

While the DWELL layers exceed the critical thickness predicted by the Matthews and Blakeslee model, experience has shown that good material quality can still be maintained, in agreement with the People and Bean theory. But it also becomes clear that placing two or more DWELL layers too close together would result in

λ (nm)	1250	1300
x_{QW}	0.15	0.15
d_{QW} (nm)	7.0	8.2
d_{QD} (nm)	0.77	0.81
$\overline{x}_{DWELL}$	0.234	0.226
d_{DWELL} (nm)	7.77	9.01
$h_{c,M\&B}$ (nm)	5.29	5.53
$d_{DWELL}/h_{c,M\&B}$	1.47	1.63
$h_{c,P\&B}$ (nm)	32.0	35.0
$d_{DWELL}/h_{c,P\&B}$	0.24	0.26

Table 2.1: Comparison of average In content and critical thickness for DWELL layers with QD emission of 1250 nm and 1300 nm.

severe strain in the structure, likely causing defects, which in turn would ruin device performance. It was found that a GaAs barrier of 15 nm between adjacent DWELL layers was sufficient to maintain good crystalline quality when stacking up to three QD layers on top of each other.

In VCL design, there is an additional constraint on the position of the gain medium: The optical mode inside the device forms a standing wave pattern between the mirrors. Gain needs to be placed at the antinodes of the intensity for optimum performance. So, instead of placing a larger number of DWELL layers at one field maximum, the gain can also be placed at adjacent antinode, at an interval of $\lambda/2$ optical path length. To compare these two possibilities and their effect on the strain in the device, the thickness and average In composition for each case can be calculated. As examples, three QD layers with an emission wavelength of 1300 nm are chosen, either all together at the center of a $\lambda/2$ cavity, or spread out in a $3\lambda/2$ design. In addition, twelve QD layers at 1250 nm, either in four groups of three, or single layers in a $12\lambda/2$ cavity. With GaAs as the barrier material, the average In content $\overline{x}$ for

k QD layers in a $l\lambda/2$ cavity is

$$\overline{x} = \frac{k(x_{QD}d_{QD} + x_{QW}d_{QW})}{l(\lambda/2n)} \tag{2.5}$$

where n is the effective index of refraction, which is approximately that of pure GaAs. The results are shown in table 2.2.

In all cases, the average In composition accumulated from the DWELL layers is high, and the cavity length exceeds the critical thickness in the Matthews and Blakeslee model. The cases with only one QD layer per $\lambda/2$ are slightly closer to the critical thickness, hinting toward better material quality. People and Bean predict a much larger critical thickness, with all cavity configurations below critical thickness, but again favors the cases with a single DWELL layer at each antinode. In some cases, however, it might not be desirable to increase the cavity length, especially for electrical devices, where carrier injection efficiency might be adversely affected.

λ (nm)	1300		1250	
k	3	3	12	12
l	1	3	4	12
$\overline{x}$	0.0319	0.0107	0.0299	0.0100
L (nm)	190	571	730	2191
$h_{c,M\&B}$ (nm)	63	226	68	244
$L/h_{c,M\&B}$	3.02	2.53	10.7	8.98
$h_{c,P\&B}$ (nm)	3611	41410	4241	48442
$L/h_{c,P\&B}$	0.053	0.014	0.172	0.045

Table 2.2: Comparison of average In content $\overline{x}$, cavity thickness L, and critical thickness h_c for different arrangements of k DWELL layers in a $l\lambda/2$ cavity.

2.2.3 Threshold Gain Estimate

The confinement factor Γ describes the overlap of the optical field intensity $|E|^2$ with the gain medium. It can be factorized into the coordinates as follows:

$$\Gamma = \Gamma_x \Gamma_y \Gamma_z \tag{2.6}$$

In a VCSEL with a laterally homogeneous epitaxial structure, both Γ_x and $\Gamma_y = 1$ and we are left with the longitudinal confinement factor Γ_z defined as [12]

$$\Gamma_z \equiv \frac{\int_{active} E(z)^2 dz}{\int_L E(z)^2 dz} \tag{2.7}$$

where L is the length of the cavity, excluding the DBR mirrors.

The dimensions for the active gain layers in QD lasers are not well defined. While it has been suggested that it is not meaningful to define a certain thickness [13], theoretical calculations show that the dipole transition matrix element of QDs is similar to that of a corresponding bulk InAs layer [14]. The total thickness of InAs deposited in each QD layer will therefore be used in our calculations. Even if this assumption is not completely correct, it only influences absolute values and not comparisons between different active region designs.

From an evaluation of round trip gain and loss in the device, an equation for the threshold gain g_{th} of a VCSEL can be derived [15]:

$$\Gamma_z g_{th} = \alpha_{in} + \Gamma_z \alpha_{diff} + \frac{1}{L} \ln\left(\frac{1}{R_{gm}}\right) \tag{2.8}$$

where R_{gm} is the geometric mean of the top and bottom DBR reflectivity and α_{in} is the total internal loss of the laser cavity. If the cavity is not doped, α_{in} will be small and can be neglected. The diffraction loss α_{diff} usually dominates in VCSELs, especially for very small lateral device dimensions. In order to get an estimate for the threshold gain, we will consider a large diameter device here and neglect diffraction losses as well.

Confinement factors for the active region designs investigated in section 2.2.2 have been calculated and are shown in table 2.3. To calculate threshold gain, mirror reflectivities are needed, see section 2.3 for different DBR design options. For the case of the 3 DWELL layers, reflectance values of 99.9% and 99.99% for the top and bottom DBRs have been assumed, reasonable values for a VCSEL, which will be discussed in chapter 3. For the 12 DWELL example, values of 99.0% and 99.97% were chosen, applicable to the case of VECSELs as in chapter 4.

The confinement factors have been calculated using the above assumptions for the dimensions of QDs. Since the value for the threshold gain g_{th} is strongly dependent on the absolute value of the confinement factor, these values might not be completely correct, but they allow a comparison of the different designs. The values shown are normalized by the total number k of DWELL layers.

λ (nm)	1300		1250	
k	3	3	12	12
l	1	3	4	12
Γ_z	0.0229	0.0084	0.0230	0.0085
$\Gamma_z g_{th}/k$ (cm^{-1})	9.7	3.2	5.9	2.0
g_{th}/k (cm^{-1})	422	382	257	232

Table 2.3: Comparison of confinement factor and threshold gain per QD layer for different arrangements of three DWELL layers at 1300 nm and twelve DWELL layers at 1250 nm.

2.3 DBR Design

Due to the low gain from the extremely thin active layers of a VCL, the mirrors needed to achieve lasing typically require more than 99% reflectivity. This is realized

by a multi-layer DBR design using $\lambda/4$ optical thickness layers of alternating low (n_1) and high (n_2) index of refraction materials. The reflectance for an ideal DBR at the design wavelength with m pairs is [16]

$$R_{DBR} = \left[\frac{1-(n_1/n_2)^{2m}}{1+(n_1/n_2)^{2m}}\right]^2 \tag{2.9}$$

The value of R_{DBR} increases with larger ratio of index of refraction between the materials, or with a larger number of DBR periods. Also of interest is the spectral width $\Delta\lambda$ of the high-reflectivity or stop band of a DBR, which is given by [17]

$$\Delta\lambda = \frac{2\lambda\Delta n}{\pi n_{eff}} \tag{2.10}$$

where $\Delta n = n_2 - n_1$ and $n_{eff} = 2(1/n_1 + 1/n_2)^{-1}$. Eq. 2.10 reduces to

$$\Delta\lambda = \frac{\lambda}{\pi}\left(\frac{n_2}{n_1} - \frac{n_1}{n_2}\right) \tag{2.11}$$

The width of the DBR stop band increases with increasing ratio of n_2 to n_1, as does the magnitude of the peak reflectance.

Different possible mirror material combinations as well as their effect on device growth, processing, and performance are discussed in the following sections.

2.3.1 Semiconductor DBR

The most common choice of materials for DBRs on GaAs substrate are GaAs and AlAs. The materials are almost perfectly lattice-matched, the growth in MBE or MOCVD reactors is well understood, and the refractive index contrast is fairly high when compared to other material systems. For a wavelength of 1300 nm, the index of refraction is $n_2 = 3.41$ for GaAs and $n_1 = 2.91$ for AlAs. A calculated reflectance spectrum for a typical semiconductor DBR is shown in Fig. 2.4.

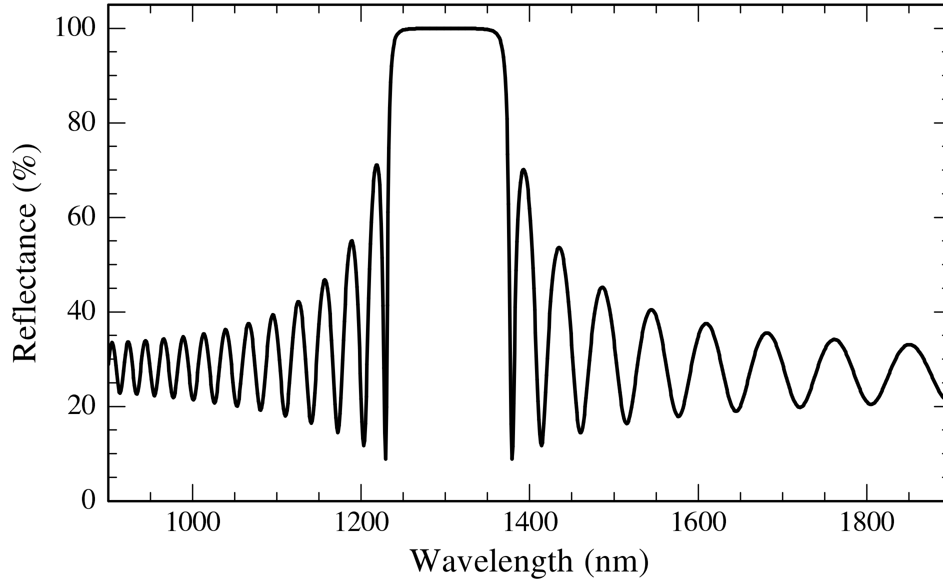

Figure 2.4: Calculated reflectance spectrum for 27 period GaAs/AlAs DBR at 1300 nm.

In a conservative design, this requires 36 pairs for the bottom DBR, yielding a reflectance value of $R_{DBR} = 99.98\%$, and 27 periods for the top (output) DBR of a VCSEL, with $R_{DBR} = 99.92\%$, respectively. This adds up to a total thickness of approximately 13 μm which — for MBE growth — is quite significant. At typical growth rates of around 1 μm per hour, this totals more than 12 hours of growth for the mirrors alone.

During extended MBE growth the flux of the different materials can drift, resulting in changing growth rates and therefore thickness of the layers. This drift is determined by measuring reflection high-energy electron diffraction (RHEED) oscillations before and after growth of a mirror test sample. In addition, the absolute thickness of the alternating layers is measured by X-ray diffraction (XRD) and optical reflectance measurements. Using these results, the cell temperatures are adjusted to yield the correct thickness, and — if necessary — ramped during growth to compensate for drift. Repeating the RHEED measurements before and after the actual

laser growth gives immediate feedback about the current structure and can be used to correct drift for subsequent growth runs.

When characterizing the final device structure using either XRD or Fourier transform infrared (FTIR) reflectance measurements, the signal contains information about the layer structure up to several micron under the surface. But with the available simulation software it is not easily possible to extract information about how the layer thickness of the DBR changes throughout the device. We found that a better way to judge the DBR uniformity vertically throughout the device is by etching it in the inductively coupled plasma (ICP) etcher while in-situ monitoring the reflectance at a single fixed wavelength. The construction and principle of operation of the reflectance measurement system is discussed in appendix A. Obviously, this technique is destructive and time consuming, so it was not carried out for every sample or for different positions on the wafer. In some cases, however, when device processing requires ICP etching of the sample anyway, this measurement provides unique information without much added effort — it actually helps in finding the correct time to end the etch process at the desired depth.

Fig. 2.5 shows an example of such an etch and reflectance signal for 25 periods of a semiconductor DBR. The simulation is based on a DBR wavelength of 1280 nm and reflectance measurement with a HeNe laser [1] ($\lambda_{\mathrm{HeNe}} = 633$ nm). In this case, the DBR layers are just over $\lambda_{\mathrm{HeNe}}/2$ thick, resulting in just more than half an oscillation of the reflectance signal per layer. This is evident in the extra feature of the signal after each layer. At the begin of the ICP etch, the measured reflectance follows the simulation very well, indicating a good match of the layer thickness to the model. After about 2 μm the predicted extra peaks are no longer discernible, indicating that the layers are now $\leq \lambda_{\mathrm{HeNe}}/2$ in thickness. Careful simulations suggest that by the end of the etch the DBR wavelength is reduced by about 2.3% to 1250 nm.

[1] A HeNe laser was used during early tests of the ICP reflectance setup. It has since been replaced by a more compact diode laser emitting at 650 nm.

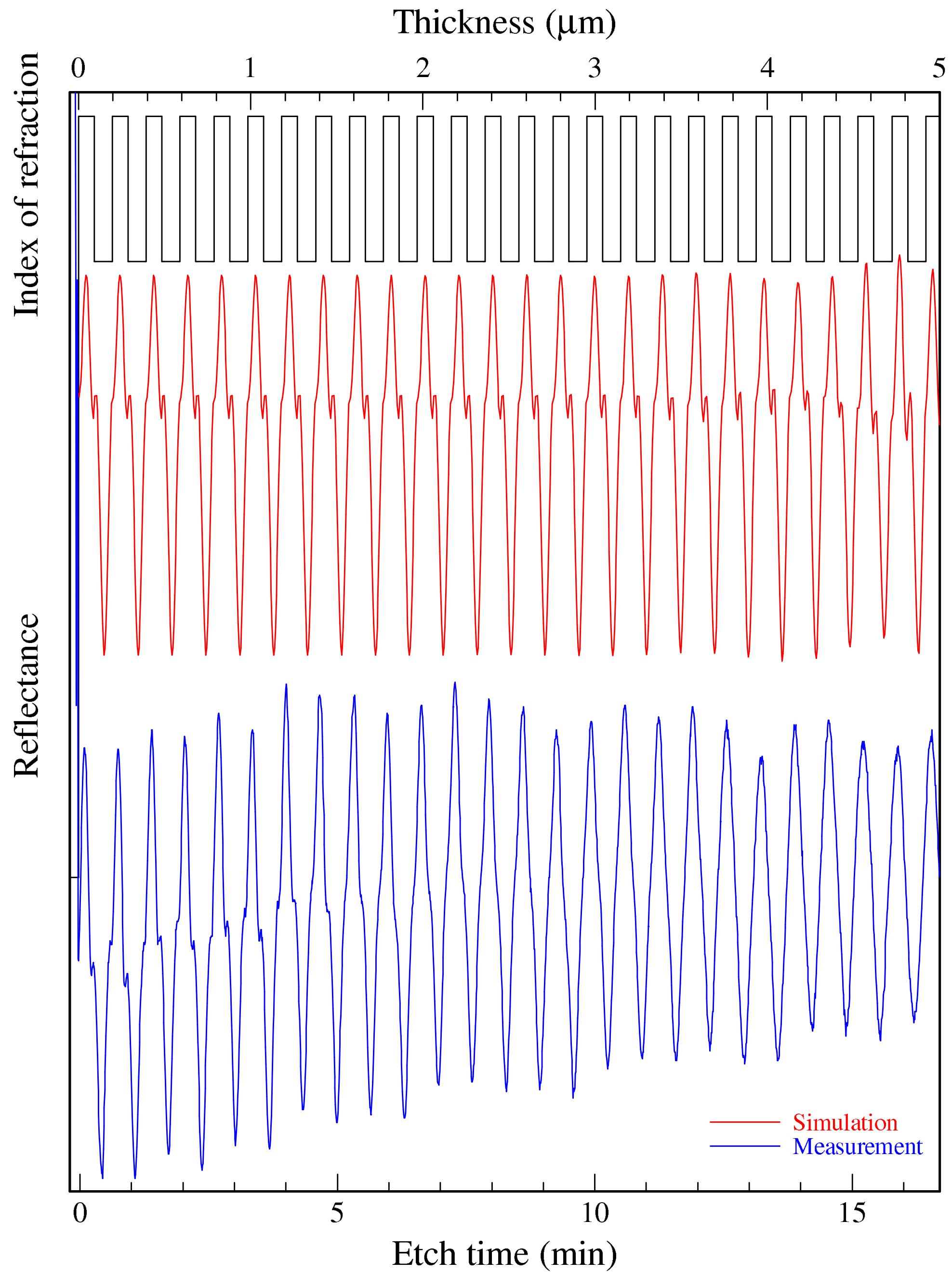

Figure 2.5: Reflectance measurement during ICP etch of semiconductor DBR showing non-uniformity of layer thickness due to drift in MBE growth rates.

2.3.2 Dielectric DBR

Another approach for high reflectivity mirrors is to deposit a dielectric DBR onto the active region after the MBE growth. Materials with higher difference in index of refraction can be chosen, significantly reducing the number of periods required. This has been successfully employed in visible [18] and IR [19] VCSELs.

Suitable materials which can be deposited in our electron beam evaporator are MgF_2 ($n_1 = 1.38$) and ZnSe ($n_2 = 2.49$). For use as a top DBR in a VCSEL this reduces the number of DBR pairs to seven with $R_{DBR} = 99.90\%$ and a thickness of about 2.5 μm. A reflectance spectrum of a dielectric DBR is shown in Fig. 2.6. Note that the higher index step not only results in a smaller number of DBR periods, but also broadens the stop-band significantly.

But even with the reduced thickness and fewer layers when compared to a MBE-grown semiconductor DBR, the deposition is still challenging. Deposition rates of

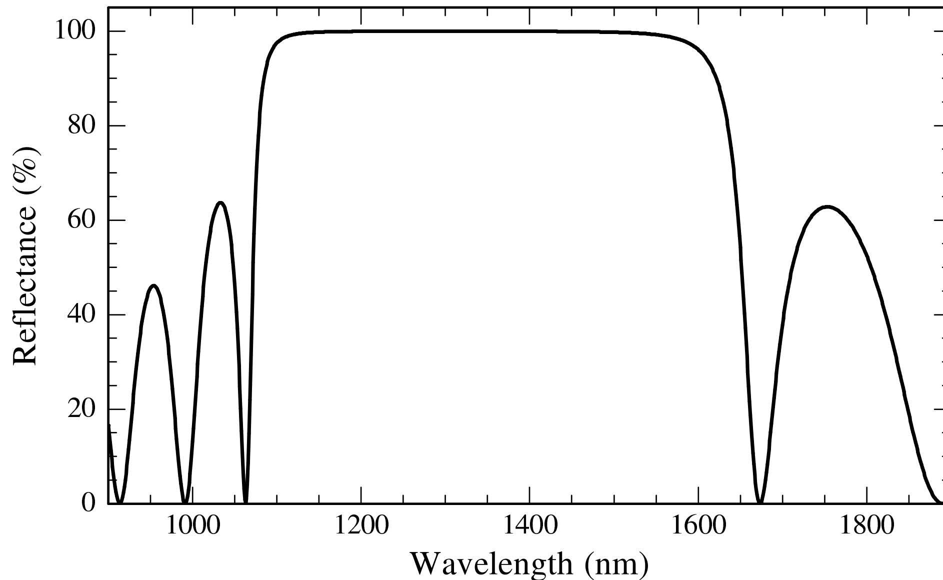

Figure 2.6: Calculated reflectance spectrum for seven period MgF_2/ZnSe DBR at 1300 nm.

$1-2$ μm per hour are common, resulting in 1-2 hours of deposition time. For our single gun machine, each material change requires a slow cool down, switch of material crucible, and careful heating of the new material, taking up a total of about 20 minutes per change. This alone adds up to almost five hours, making each dielectric DBR an all day job. In addition, deposition rates are not very well controlled and need to be determined with several calibration runs.

In comparison with semiconductor DBRs, there are a few disadvantages of dielectric DBRs: Since the materials are insulators, dielectric mirrors cannot be used to supply current to electrically injected devices. In addition, the thermal conductivity is lower than in the case of semiconductors, so more attention has to be paid to heatsinking.

The main problem with our dielectric DBRs was the low quality of the material, on close inspection with an optical microscope the samples were covered with material spatter and small air inclusions. This is probably the reason for the low damage threshold of the dielectric DBRs observed in optical pumping experiments. When a focused Ti:Sapphire beam was scanned across the sample, sparks were visible emerging from the focal spot and the DBR surface was permanently damaged, when inspected under an optical microscope (Fig. 2.7).

2.3.3 Oxide DBR

The discovery of controlled oxidation of epitaxial AlAs layers [20] at elevated temperatures in a humid environment offers another possibility for DBRs [21]: The oxide formed has an index of refraction of approximately $n_1 = 1.55$ at 1300 nm. As the oxidation process is extremely selective, with a negligible oxidation rate for layers of $Al_xGa_{1-x}As$ with $x < 0.9$, the entire DBR can be grown monolithically using MBE with the oxidation carried out after the growth. $\lambda/4$ thick GaAs ($n_2 = 3.41$) serves

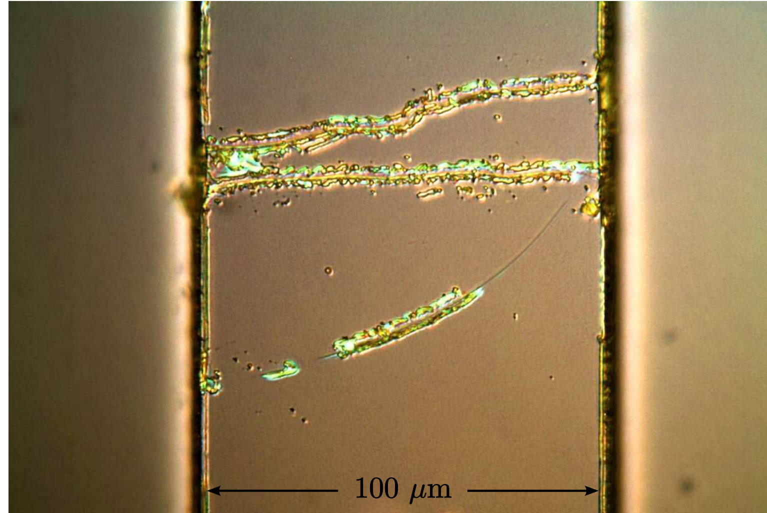

Figure 2.7: Photomicrograph of damage to a dielectric DBR due to the incident focused pump laser.

as the high index layers, alternating with AlAs layers of a thickness which, after subsequent oxidation, will result in $\lambda/4$ optical thickness of AlO_x. Since the contrast in index of refraction is even higher than in the case of dielectric DBRs, a seven period oxide DBR has a maximum reflectance of $R_{DBR} = 99.99\%$ over an even wider wavelength range. A calculated reflectance spectrum is shown in Fig. 2.8.

Oxidation System and Procedure

The water required for the selective oxidation of AlAs is not part of usual semiconductor processing equipment, so custom built systems were used. A schematic diagram of a oxidation furnace is shown in Fig. 2.9. The sample is introduced into a quartz tube on a graphite holder and pushed to the center of the furnace using a quartz rod. The tube is purged with N_2 while the sample is allowed to stabilize at the set temperature, typically 425°C. Then the gas flow is switched over to the steam generator, a flask of deionized (DI) water held at a constant temperature of

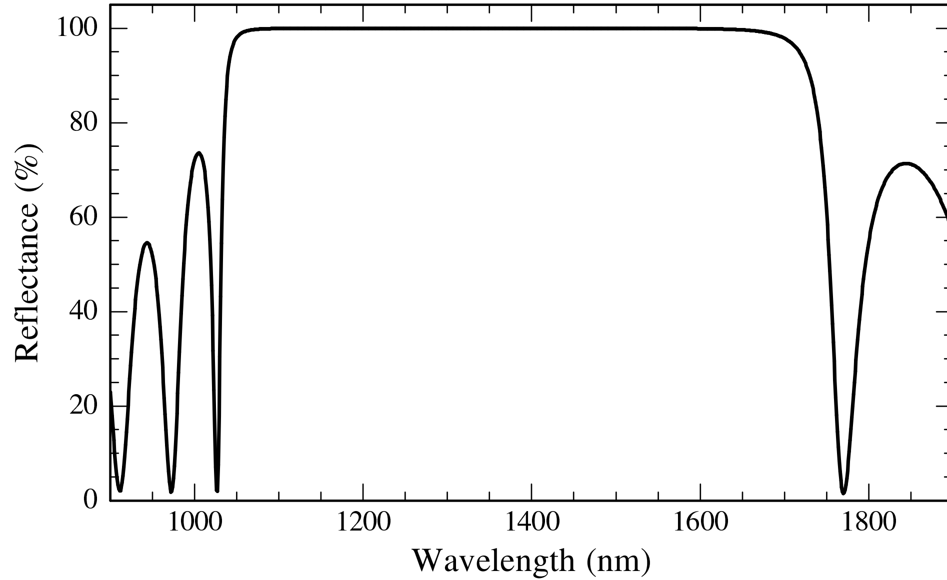

Figure 2.8: Calculated reflectance spectrum for seven period AlO_x/GaAs DBR at 1300 nm.

90°C. N_2 is released at the bottom of the water container and while rising to the top becomes saturated with water vapor. This mixture is then introduced into the furnace where it flows across the sample and the oxidation reaction takes place. After the desired oxidation time has passed, the flow is once again switched over to dry N_2. The oxidized device structure is then removed from the furnace, preferably after allowing it to cool in the N_2 environment. The complete standard operating procedure used for oxidation is reproduced in appendix B.

In this work, two different oxidation furnaces were used: One was a converted liquid-phase epitaxy system with two inch diameter quartz tubes in a Thermco furnace. Due to the small tube and the sample holder design, the sample size is limited to about 15 mm. The second was newly built by Zia Laser Inc. and installed inside the CHTM cleanroom. A four inch diameter tube and specially designed sample holder plates can accommodate entire two inch wafers or any smaller size samples.

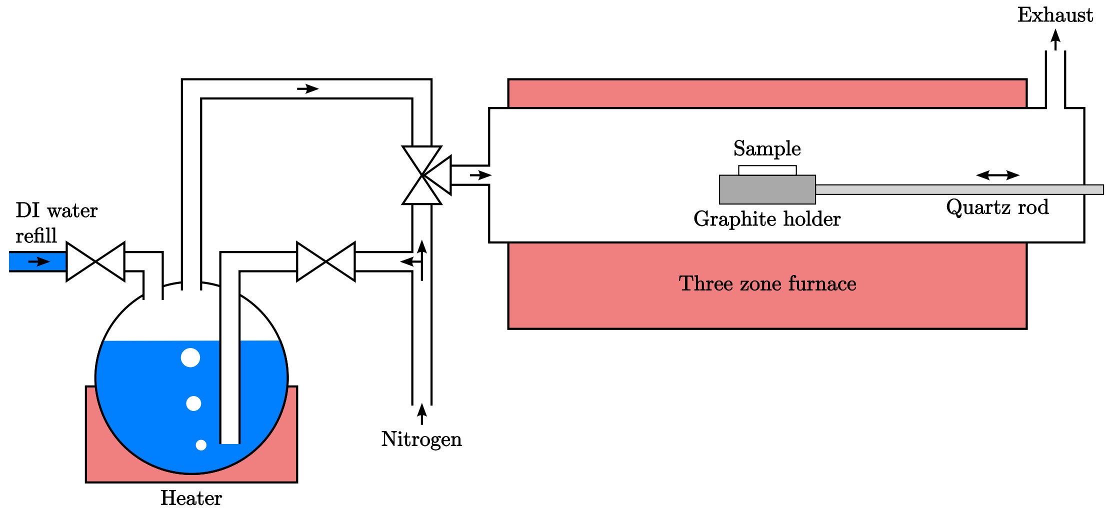

Figure 2.9: Schematic diagram of wet oxidation system.

The new system also results in more reproducible conditions, since the furnace is kept at operating temperature continuously, and the flow of the N_2 carrier gas is controlled using a mass flow controller instead of a flow tube meter.

More advanced wet oxidation systems [22] allow for in-situ monitoring of the oxidation process. The sample is placed inside a vacuum chamber on top of a heater close to a window to allow real time observation with an optical microscope. Steam is introduced into the chamber at low enough pressure to prevent condensation on the cold window, which would obstruct the view of the oxidation progress in the sample. Unfortunately, due to time constraints and a lack of available components, we never constructed such a system.

Mechanical Stability of AlO_x

The wet oxidation of AlAs not only lowers the index of refraction of the material, it also leads to a reduction in the layer thickness [23]. In experiments with pure AlAs, we found this shrinkage to be roughly 10% of the original layer thickness.

The resulting mechanical stress on the structure can cause problems like cracking or delamination of top device layers. To reduce these effects, we decided to compositionally grade the transitions between GaAs and AlAs.

Since a continuous change in the composition of a random alloy is very hard to achieve in MBE growth, the grade was realized as a digital alloy of GaAs and AlAs. The layer structure of the digital grade is shown in Fig. 2.10. Since half the thickness of the grade is GaAs, the other half AlAs, the corresponding adjustments were made to the DBR layers in the design to accommodate the additional thickness of the graded region. DBRs grown using this technique showed no measurable change in reflectance and the mechanical strength of the structure proved adequate for mirrors processed into stripes of 100 μm width.

For small mesas it has been shown [24] that even $Al_{0.98}Ga_{0.02}As$ shows a significant improvement in mechanical stability over pure AlAs, due to reduced shrinkage of the

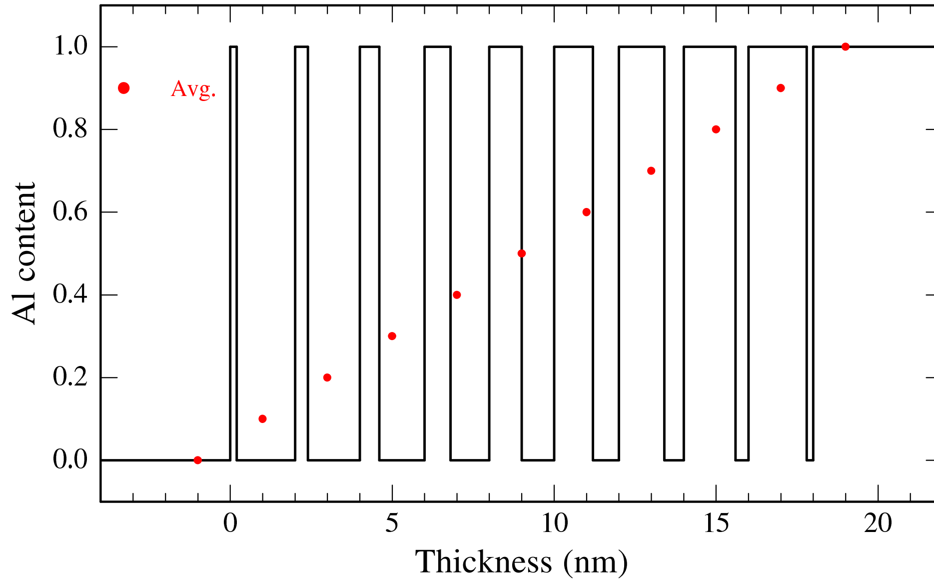

Figure 2.10: Layer structure of a digital alloy graded interface from GaAs to AlAs. The red dots indicate the average composition for each period.

DBR layers during oxidation. Even better performance was achieved by using a digital instead of a random alloy of identical composition [25].

Oxidation Rate Characterization

The rate at which the oxidation proceeds depends on many factors: Material composition, layer thickness, furnace temperature, water content and flow rate of N_2 carrier gas. For a quick characterization, small pieces cleaved from a wafer of suitable layer structure can be oxidized. If the AlGaAs or AlAs layer is not covered by too much GaAs or other material, the extent of the oxide is visible under a Nomarski or IR microscope. An example photomicrograph is shown in Fig. 2.11.

Since the layer thickness is usually fixed ($\lambda/4$), the composition of the AlGaAs layer can be changed to adjust the lateral oxidation rate to the device dimensions.

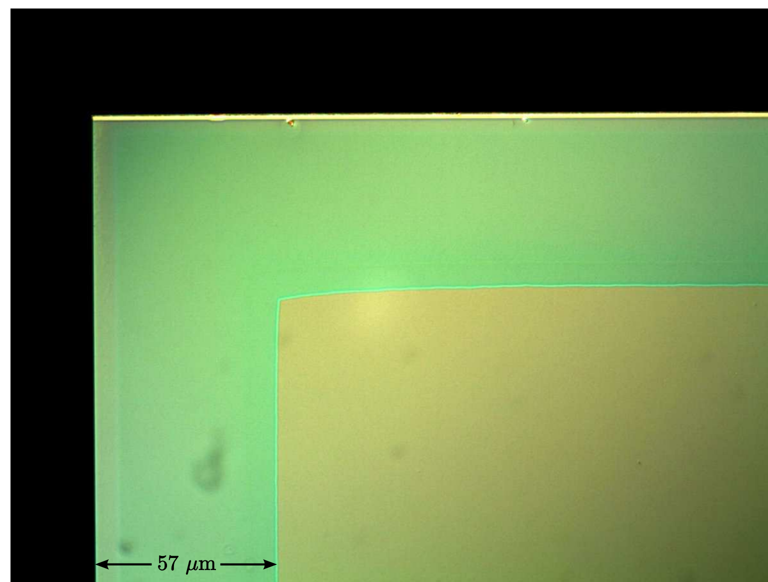

Figure 2.11: Photomicrograph of oxidation front (appears green in this image as result of the Nomarski interference contrast microscopy technique used) at the corner of a cleaved sample.

The oxidation rate is very sensitive to the composition of the AlGaAs layer, so several digital alloy samples were MBE-grown for characterization. The oxidation rates averaged from two separate 30 minute oxidation runs as a function of the Al content are shown in Fig. 2.12. The same experiment was carried out on both wet oxidation systems. The Zia Laser furnace produced approximately 30% higher oxidation rates, likely due to the slightly higher temperature (435°C vs. 425°C in the Thermco furnace). The optical and mechanical properties of the resulting oxide were indistinguishable.

Since the oxidation rate is not constant with time, the numbers from Fig. 2.12 can only be used as a guide to estimate required times for processing. The exact oxidation time required was determined in a calibration run of the same wafer and same geometry on the day of device processing.

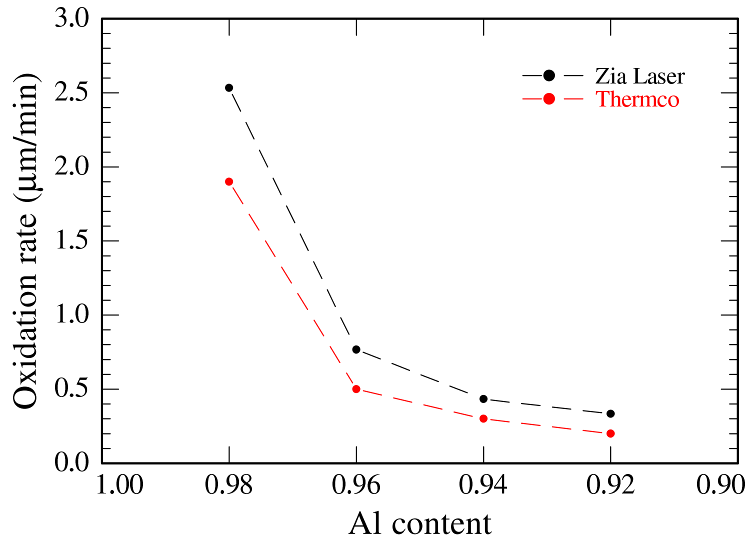

Figure 2.12: Oxidation rate from 30 minute oxidation as function of Al content in the AlGaAs layer for both wet oxidation systems.

2.4 Conclusions

The growth parameters to reach an emission wavelength of 1250 – 1300 nm from InAs QDs were discussed, together with the temperature dependence of the gain peak, which follows the bandgap shrinkage of bulk InAs.

Strain introduced due to the lattice-mismatch between InAs and GaAs was quantified for single DWELL layers and the different cavity designs. Confinement factors for the different active regions were compared and values for threshold gain required in the different structures were estimated. If only a single layer is placed in each $\lambda/2$ cavity segment, strain is reduced and — based on the assumption of negligible loss in the cavity — threshold gain is lowered. However, such thick device structures are likely not practical for electrical injection.

Possible material choices for the design of DBRs have been discussed. The most common approach on GaAs substrates is to use semiconductor based GaAs/Al(Ga)As mirrors. MBE growth of these structures can be challenging due to growth rate drift during the long time required to grow the large number of mirror pairs.

A higher difference in index of refraction between the two materials in the DBR reduces the number of layers needed and at the same time widens the spectral bandwidth of the mirror, ideal for the broad emission spectrum of QDs. Dielectric MgF_2/ZnSe mirror stacks were manufactured, but suffered from a low optical damage threshold, likely due to impurities incorporated during deposition.

DBRs formed by selective wet oxidation of AlAs combine the high reflectivity of dielectric DBRs with well controlled MBE growth of the structure. An oxidation system was designed and characterized. Consideration was given to the mechanical stability of the mirrors, which was improved by adding a small amount of Ga to the oxidation layer and/or digitally grading the interfaces between the materials.

References

[1] Yasuyuki Miyamoto, Ming Cao, Yasushi Shingai, Kazuhito Furuya, Yasuharu Suematsu, K. G. Ravikumar, and Shigehisa Arai. Light Emission from Quantum-Box Structure by Current Injection. *Japanese Journal of Applied Physics*, 26(Part 2, No. 4):L225–L227, 1987.

[2] L. Goldstein, F. Glas, J. Y. Marzin, M. N. Charasse, and G. Le Roux. Growth by molecular beam epitaxy and characterization of InAs/GaAs strained-layer superlattices. *Applied Physics Letters*, 47(10):1099–1101, 1985.

[3] N. Kirstaedter, N.N. Ledentsov, M. Grundmann, D. Bimberg, V.M. Ustinov, S.S. Ruvimov, M.V. Maximov, P.S. Kop'ev, Zh.I. Alferov, U. Richter, P. Werner, U. Gosele, and J. Heydenreich. Low threshold, large T_0 injection laser emission from (InGa)As quantum dots. *Electronics Letters*, 30(17):1416–1417, Aug 1994.

[4] L.F. Lester, A. Stintz, H. Li, T.C. Newell, E.A. Pease, B.A. Fuchs, and K.J. Malloy. Optical characteristics of 1.24-μm InAs quantum-dot laser diodes. *Photonics Technology Letters, IEEE*, 11(8):931–933, Aug 1999.

[5] G. Liu, A. Stintz, H. Li, K.J. Malloy, and L.F. Lester. Extremely low room-temperature threshold current density diode lasers using InAs dots in $In_{0.15}Ga_{0.85}As$ quantum well. *Electronics Letters*, 35(14):1163–1165, Jul 1999.

[6] I. N. Stranski and L. von Krastanov. *Abhandlungen der Mathematisch-Naturwissenschaftlichen Klasse, Akademie der Wissenschaften und der Literatur in Mainz*, 146:797, 1939.

[7] A. Stintz, G. T. Liu, A. L. Gray, R. Spillers, S. M. Delgado, and K. J. Malloy. Characterization of InAs quantum dots in strained $In_xGa_{1-x}As$ quantum wells. *Journal of Vacuum Science & Technology B*, 18(3):1496–1501, 2000.

[8] J. W. Matthews and A. E. Blakeslee. Defects in epitaxial multilayers. *Journal of Crystal Growth*, 27:118–125, December 1974.

[9] Jeffrey Y. Tsao. *Fundamentals of Molecular Beam Epitaxy*. Academic Press, Inc. San Diego, California, 1993.

[10] W. E. Hoke, T. D. Kennedy, and A. Torabi. Simultaneous determination of Poisson ratio, bulk lattice constant, and composition of ternary compounds: $In_{0.3}Ga_{0.7}As$, $In_{0.3}Al_{0.7}As$, $In_{0.7}Ga_{0.3}P$, and $In_{0.7}Al_{0.3}P$. *Applied Physics Letters*, 79(25):4160–4162, 2001.

[11] R. People and J. C. Bean. Calculation of critical layer thickness versus lattice mismatch for Ge_xSi_{1-x}/Si strained-layer heterostructures. *Applied Physics Letters*, 47(3):322–324, 1985.

[12] S. W. Corzine, R. S. Geels, J. W. Scott, R.-H. Yan, and L. A. Coldren. Design of Fabry-Perot surface-emitting lasers with a periodic gain structure. *IEEE Journal of Quantum Electronics*, 25:1513–1524, June 1989.

[13] Alexander A. Ukhanov. *Study of the carrier-induced optical properties in III-V quantum confined laser nano-structures*. PhD thesis, The University of New Mexico, May 2004.

[14] P. G. Eliseev, H. Li, A. Stintz, G. T. Liu, T. C. Newell, K. J. Malloy, and L. F. Lester. Transition dipole moment of InAs/InGaAs quantum dots from experiments on ultralow-threshold laser diodes. *Applied Physics Letters*, 77:262–264, July 2000.

[15] Siu Fung Yu. *Analysis and Design of Vertical Cavity Surface Emitting Lasers*. Wiley Series in Lasers and Applications, 2003.

[16] Scott W. Corzine Larry A. Coldren. *Diode Lasers and Photonic Integrated Circuits*. Wiley Series in Microwave and Optical Engineering, 1995.

[17] Carl Wilmsen, Henryk Temkin, and Larry A. Coldren. *Vertical-Cavity Surface-Emitting Lasers - Design, Fabrication, Characterization, and Applications*. Cambridge Studies in Mondern Optics, 1999.

[18] J.A. Lott, Jr. Schneider, R.P., K.J. Malloy, S.P. Kilcoyne, and K.D. Choquette. Partial top dielectric stack distributed Bragg reflectors for red vertical cavity surface emitting laser arrays. *Photonics Technology Letters, IEEE*, 6(12):1397–1399, Dec 1994.

[19] K. Uomi, S.J.B. Yoo, A. Scherer, R. Bhat, N.C. Andreadakis, C.E. Zah, M.A. Koza, and T.P. Lee. Low threshold, room temperature pulsed operation of 1.5 μm vertical-cavity surface-emitting lasers with an optimized multi-quantum well active layer. *Photonics Technology Letters, IEEE*, 6(3):317–319, Mar 1994.

[20] W. T. Tsang. Self-terminating thermal oxidation of AlAs epilayers grown on GaAs by molecular beam epitaxy. *Applied Physics Letters*, 33:426–429, September 1978.

[21] D. L. Huffaker and D. G. Deppe. Low threshold vertical-cavity surface-emitting lasers based on high contrast distributed Bragg reflectors. *Applied Physics Letters*, 70(14):1781–1783, 1997.

[22] S.A. Feld, J.P. Loehr, R.E. Sherriff, J. Wiemeri, and R. Kaspi. In situ optical monitoring of AlAs wet oxidation using a novel low-temperature low-pressure steam furnace design. *Photonics Technology Letters, IEEE*, 10(2):197–199, Feb 1998.

[23] J. M. Dallesasse, Jr. N. Holonyak, A. R. Sugg, T. A. Richard, and N. El-Zein. Hydrolyzation oxidation of $Al_xGa_{1-x}As$–AlAs–GaAs quantum well heterostructures and superlattices. *Applied Physics Letters*, 57(26):2844–2846, 1990.

[24] K.D. Choquette, K.M. Geib, C.I.H. Ashby, R.D. Twesten, O. Blum, H.Q. Hou, D.M. Follstaedt, B.E. Hammons, D. Mathes, and R. Hull. Advances in selective wet oxidation of AlGaAs alloys. *Selected Topics in Quantum Electronics, IEEE Journal of*, 3(3):916–926, Jun 1997.

[25] G. W. Pickrell, J. H. Epple, K. L. Chang, K. C. Hsieh, and K. Y. Cheng. Improvement of wet-oxidized $Al_xGa_{1-x}As$ (x $\sim$ 1) through the use of AlAs/GaAs digital alloys. *Applied Physics Letters*, 76(18):2544–2546, 2000.

Chapter 3

Quantum Dot Vertical-Cavity Surface-Emitting Laser

3.1 Introduction

The increasing demand for higher bandwidth in telecommunications, internet connections, and cable television has fueled the advance of fiber-optic transmission techniques. For short-distance (< 100 m) local area network applications, widely available 850 nm LEDs or VCSELs are used successfully, but their range is severely limited by the high absorption loss in the fiber at that wavelength. For metropolitan area networks (< 50 km) or longer distances, operating wavelengths of 1.3 or 1.5 μm are essential. Standard single-mode fibers (SMFs) [1, 2] have no dispersion at 1.3 μm, making that wavelength ideal for high-speed transmissions. The absorption loss is even lower at 1.5 μm, but pulse broadening due to the non-zero dispersion limits bandwidth at that wavelength. While this can be circumvented by using dispersion-shifted fiber [3], most of the optical fiber already installed still suffers from that limitation.

Typical light sources for fiber-optic transmission at 1.3 μm are InP-based distributed feedback (DFB) lasers. Their drawbacks include the higher cost of InP substrates, challenging fabrication of the DFB gratings, and as a consequence of the edge-emitting design, labor-intensive processing, cleaving and AR/HR coating of facets, packaging, and coupling the highly divergent output beam into a fiber. Due to the high operating current, active heatsinking using TE coolers is usually necessary for satisfactory device performance.

VCSELs on the other hand are smaller and have lower threshold and operating currents, allowing them to be used without TE coolers in many applications. They can be processed and tested on wafer scale and since they don't rely on cleaved facets, the devices can be automatically separated with a dicing saw. Their low divergence, circular output beam is ideal for coupling into optical fibers. As much as 90% coupling efficiency has been demonstrated for lens-like etched fiber ends [4], more than 80% for as-cleaved fibers [5].

The lack of suitable DBR mirrors on InP substrate significantly limits possible active region designs for 1.3 μm emission. While AlGaInAs/InP active regions have been successfully bonded to GaAs/AlGaAs DBRs to produce electrically pumped VCSELs [6], a monolithic approach would be much preferred for its less complex processing and better electrical properties. A GaAsSb QW active region has been proposed [7], and optically pumped operation [8], as well as electrically injected [9] VCSELs have been demonstrated. While continuous wave (CW) operation was achieved, output powers were low (< 0.1 mW) and the longest lasing wavelength reported was 1295 nm.

The main focus has been on the development of GaInNAs VCSELs, with first CW operation near 1.3 μm reported in 2000 [10], soon reaching output powers above 1 mW [11], and commercial devices have been announced [12]. However, some issues still remain, including polarization control, and high-temperature performance.

InAs QDs promise to overcome several of the problems encountered with other VCSEL designs: Since they are grown on GaAs substrate, active region and high quality GaAs/AlGaAs or GaAs/AlO_x mirrors can be MBE-grown monolithically. QD edge-emitting lasers have demonstrated very good device performance, including record-low threshold current densities [13]. The broad emission spectrum of QDs would be an advantage for tunable or mode-locked devices, their higher resistance to optical feedback should eliminate the need for an optical isolator.

Electrically injected short-wavelength (≈ 1 μm) QD VCSELs with good performance were reported in 1997 [14, 15], more recently even MOCVD grown devices at 1100 nm have been reported [16].

Pulsed operation of a 1.3 μm oxide DBR QD VCSEL was achieved in 2000 [17], by 2002 CW output powers in excess of 1 mW were reported by the same group [18]. Recently, semiconductor DBR devices have shown promising performance [19], but with limited output powers.

In this chapter, the development of QD VCSELs is demonstrated based on three different device designs: first, an optically pumped VCSEL structure is realized, followed by electrically injected devices with both oxide and semiconductor DBRs.

3.2 Optically Pumped VCSEL

As a first step in the development of QD VCSELs, an optically pumped structure was designed. This significantly reduces the number of processing steps required before testing the VCSEL and also the complexity of the design, when compared to an electrically injected device.

3.2.1 Design

As discussed in the previous chapter, oxide DBRs combine high reflectivity with reasonable MBE growth times, so this mirror design was chosen for the optically pumped VCSEL. The device was to be pumped through the top DBR with a Ti:Sapphire laser around 800 nm, which would be absorbed in the GaAs layers of the mirror. To prevent that, the material composition of the high index layers was changed to $Al_{0.15}Ga_{0.85}As$, which has a bandgap corresponding to a wavelength of around 760 nm, and therefore does not absorb the pump laser. The Al content is low enough, however, to ensure that the layer is not affected by the wet oxidation used to convert the AlAs layers to oxide. Six DBR pairs were grown for the top (output) reflector, eight for the bottom. The interfaces between $Al_{0.15}Ga_{0.85}As$ and AlAs were digitally graded over 18 nm.

The $3\lambda/2$ thick cavity contains two groups of three DWELL layers, placed at subsequent antinodes of the electrical field standing wave pattern. The index of refraction profile of the device structure and simulated electrical field strength [20] are shown in Fig. 3.1.

3.2.2 Processing

The lateral dimensions of an optically pumped VCSEL are defined by the spot of the pump laser; no processing is needed. Due to the use of oxide DBRs, however, some form of patterning is required to reduce the lateral extent of the AlAs layers to be oxidized. A pattern of 100 μm wide stripes with a pitch of 250 μm was transfered onto the sample using photolithography. The area between the stripes was then etched using the ICP etcher. The exact etch depth is not critical, as long as it exceeds the total thickness of the device, including top DBR, active region, and bottom DBR. After removing the etch mask, this can be verified using a stylus surface profilometer.

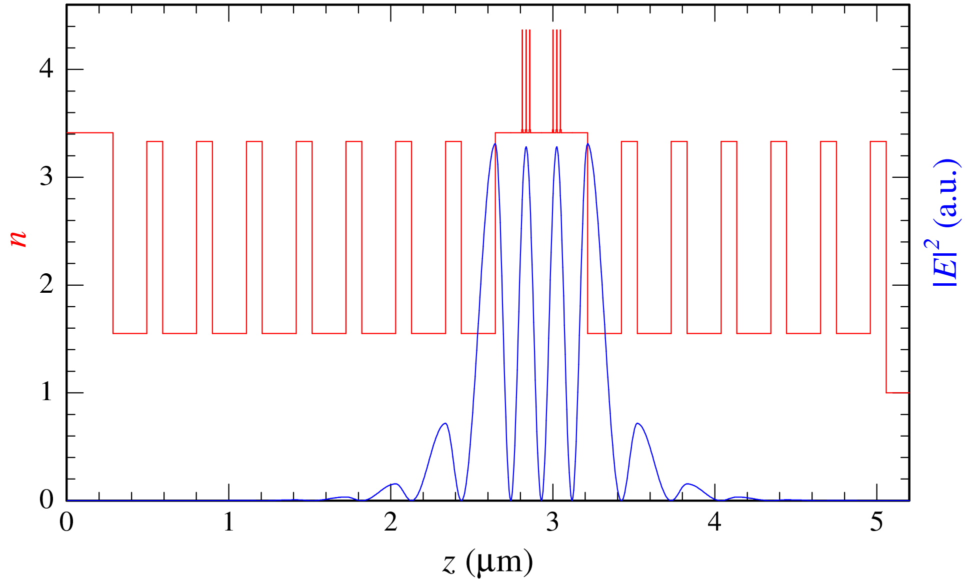

Figure 3.1: Refractive index n and calculated electric field $|E|^2$ for the optically pumped VCSEL sample. The digitally graded DBR interfaces have been omitted for clarity.

The etched sample is then oxidized in a wet oxidation system as described in section 2.3.3. The process time is chosen based on 50 μm lateral oxidation, to make sure the 100 μm wide stripes are oxidized uniformly. Finally, a reflectance spectrum is recorded using a FTIR spectrometer. A correction for the background signal from the exposed GaAs substrate is necessary as the spot size is much larger than the device dimensions. The resulting spectrum, compared to a simulation, is shown in Fig. 3.2.

3.2.3 Experimental Setup

A schematic diagram of the experimental setup is shown in Fig. 3.3. The sample is mounted on a temperature-controlled heatsink. For optical pumping, a tunable Ti:Sapphire laser was used. The pump wavelength was around 800 nm, but adjusted

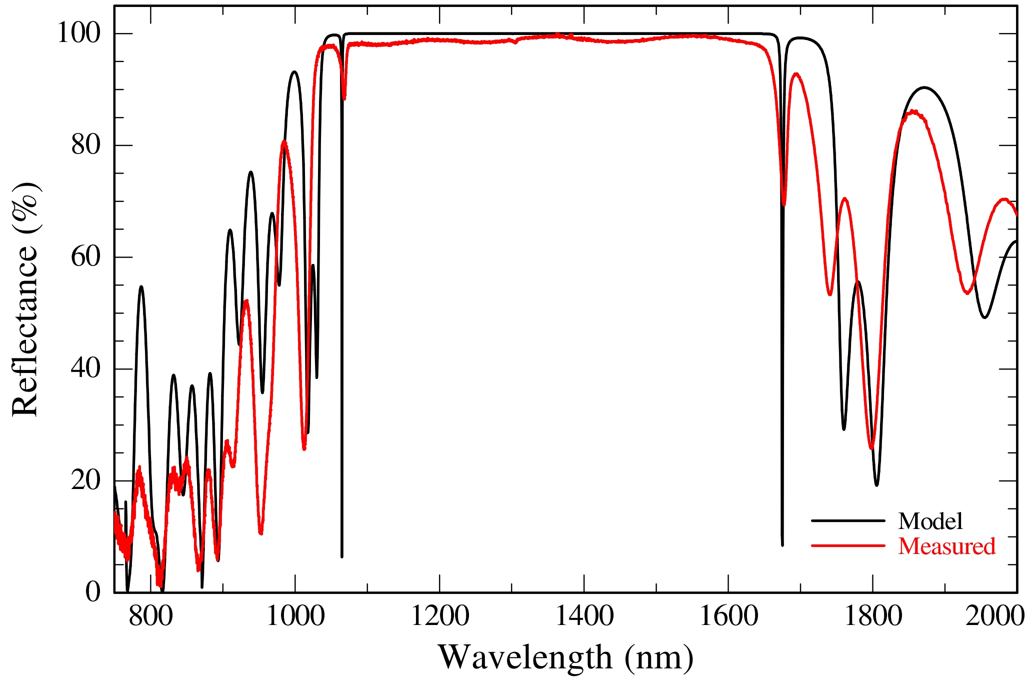

Figure 3.2: Modeled and measured reflectance spectra for optically pumped VCSEL sample after oxidation.

for each experiment to match a minimum in the sample reflectivity. The pump laser passes through a beam splitter (≈ 70% transmission at 800 nm) and is focused onto the sample with a microscope objective. The emitted light from the sample is collected with the same objective and the signal reflected from the beam splitter (≈ 70% reflection at 1300 nm) is measured by an optical power meter. Any scattered or reflected pump light is removed by a 900 nm long pass filter before reaching the detector. In addition, the VCSEL output can also be directed onto an optical fiber bundle to measure emission spectra using a grating monochromator and a GaInAs photo diode.

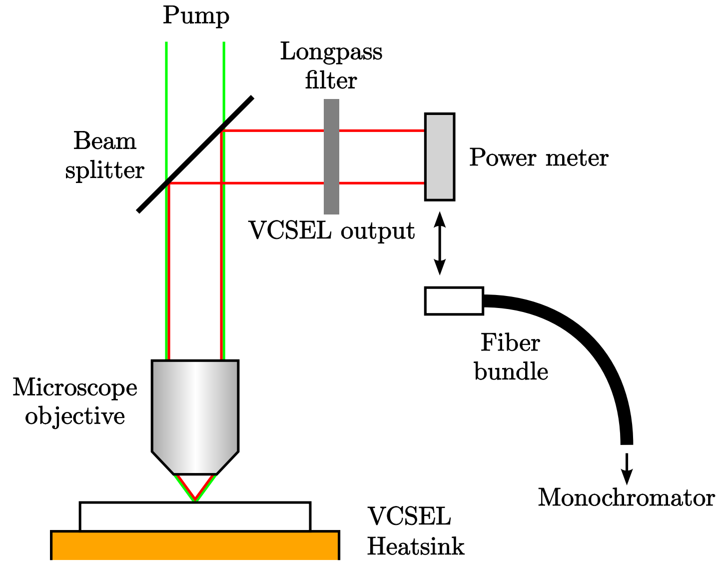

Figure 3.3: Schematic diagram of optically pumped VCSEL setup.

3.2.4 Experimental Results

A plot of the output power from the optically pumped VCSEL as function of incident pump power is shown in Fig. 3.4. The lasing threshold was reached at very low pump powers of around 10 mW at 10°C. The maximum output power achieved was only about 10 μW, even after correcting for the loss at the beam splitter. Combined with the low threshold, this suggests that only a very small area of the sample participates in the lasing action. Also, since the same microscope objective is used to focus the pump light and collect the sample emission, it is not possible to optimize each one independently. The objective used is certainly not perfectly achromatic from 800–1300 nm, which might result in significantly reduced collection efficiency.

Fig. 3.5 contains lasing spectra corresponding to three different pump powers from Fig. 3.4. While the resolution of the grating monochromator and the dynamic range of the GaInAs detector are somewhat limited, it seems quite clear that all the lasing emission occurs at a single wavelength. This is again consistent with the

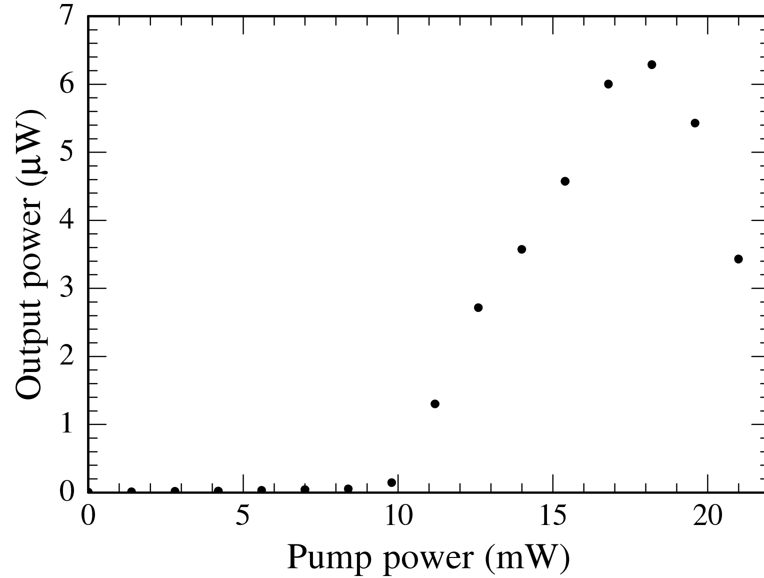

Figure 3.4: Optically pumped VCSEL output power as function of incident pump power, both corrected for the losses at the beam splitter, at a heatsink temperature of 10°C.

excitation of a small lateral active area in the VCSEL, only supporting one lasing mode.

Optical pumping experiments were repeated for different heatsink temperatures. The maximum output power achieved at each temperature is shown in Fig. 3.6. The VCSEL operated to slightly above room temperature, with a roughly linear decrease in output power with increasing temperature.

Lasing spectra were recorded at 0, 10, and 20°C and are compared in Fig. 3.7. The lasing emission shifts to longer wavelengths at a rate of approximately 0.1 nmK^{-1}.

Since the optically pumped VCSEL was only meant to be a proof of concept and testbed for QD active regions in VCLs, no further experiments were conducted and our efforts were instead focused on the development of electrically injected QD VCSEL diodes.

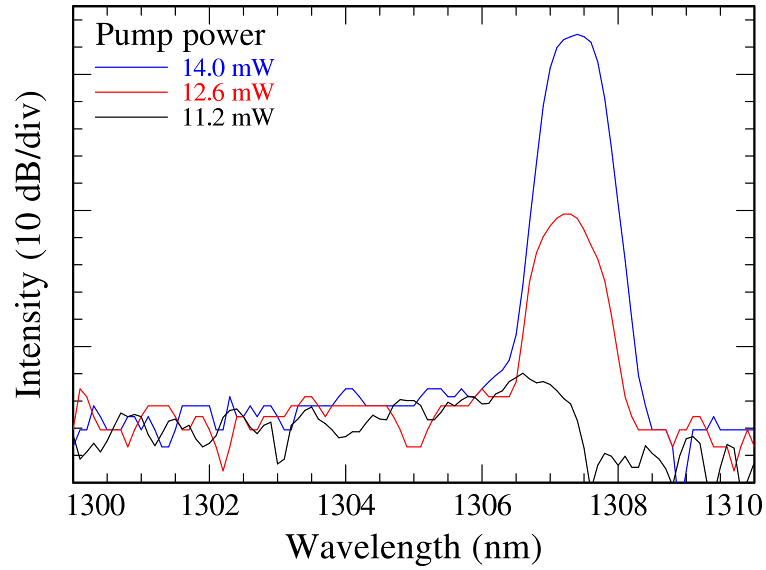

Figure 3.5: Optically pumped VCSEL lasing spectra for different pump powers at a heatsink temperature of 10°C.

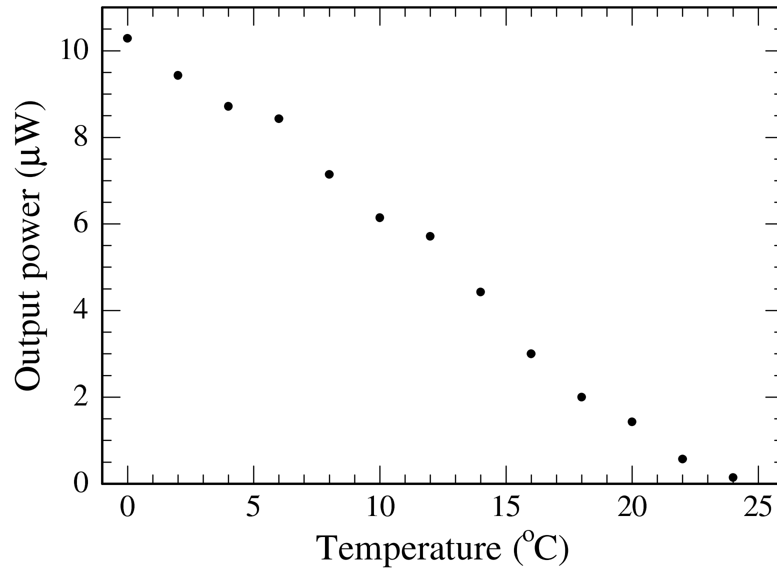

Figure 3.6: Maximum optically pumped VCSEL output power as function of the heatsink temperature.

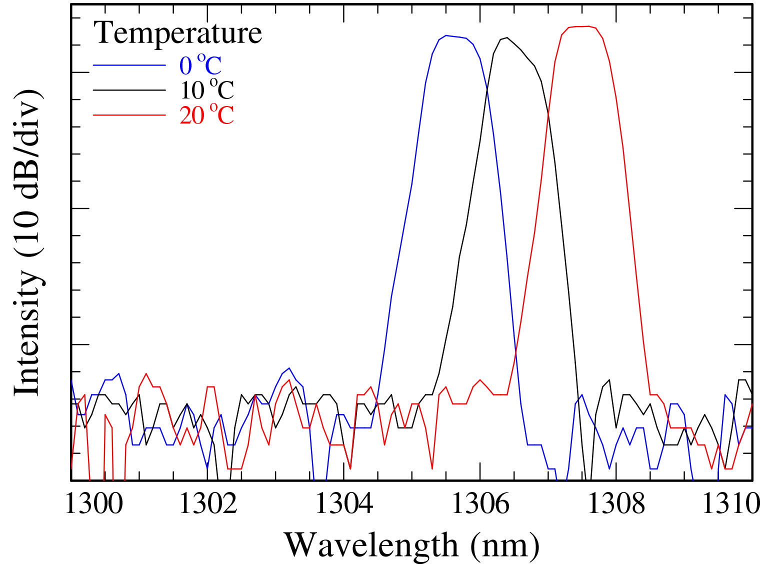

Figure 3.7: Optically pumped VCSEL lasing spectra for different heatsink temperatures.

3.3 Oxide DBR Electrically Injected VCSEL

The usefulness of GaAs/AlO_x mirrors formed by selective wet oxidation of AlAs is confirmed by the results from the optically pumped VCSEL. The design of QD VCSEL diodes with oxide DBRs is quite challenging for several reason, including the mechanical stress introduced during oxidation, and the electrically insulating properties of the oxide. However, an elegant solution was found and devices were processed.

3.3.1 Design

Since the GaAs/AlO_x DBRs are not electrically conductive, the current can not be injected through the mirror stacks. This can be solved by placing the p- and n-type contact layers on opposite sides of the active region, but inside of the DBRs. This

scheme is typically referred to as intra-cavity contacts [21].

To prevent the carriers from spreading throughout the device structure, one usually has to use proton implantation [22] to concentrate the current in the small active area at the center of the VCSEL. Instead, one can use an AlGaAs layer of suitable thickness and composition, placed close to the active layers in the device structure. An aperture can then be formed by laterally oxidizing that layer until an opening of the desired dimension remains at the center of the device [23].

A VCSEL design has been proposed [24], which combines all these elements. The refractive index profile and simulated standing wave pattern is shown in Fig. 3.8. The bottom DBR consists of seven pairs of $Al_{0.98}Ga_{0.02}As$/GaAs layers, grown as a digital alloy. For the five pairs of the top DBR, the material composition was changed to $Al_{0.96}Ga_{0.04}As$ to achieve comparable oxidation time despite the smaller lateral dimensions in the final device (see section 3.3.2).

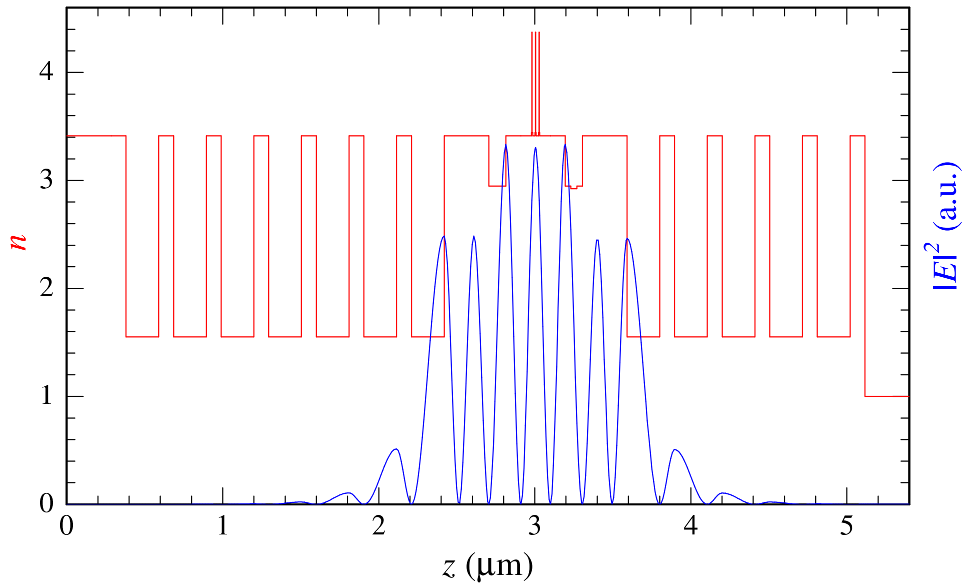

Figure 3.8: Refractive index n and calculated electric field $|E|^2$ for electrically injected oxide DBR VCSEL. The digital alloys and graded interfaces have been omitted for clarity.

The layer structure and index of refraction profile are shown in more detail in Fig. 3.9. Next to the DBRs are highly doped contact layers, followed by slightly lower doped spacer layers, until an optical thickness of $3\lambda/4$ is reached. At this point a $\lambda/4$ $Al_{0.92}Ga_{0.08}As$ layer is placed, effectively forming a semiconductor DBR pair together with the surrounding GaAs. This extra reflector confines more of the optical power at the center of the cavity, reducing the overlap of the lasing mode with the highly doped contact layers, lowering free carrier absorption. The interfaces between the GaAs and AlGaAs layers were all digitally graded to help reduce series resistance. For lateral current confinement, a 40 nm $Al_{0.97}Ga_{0.03}As$ layer is incorporated into the p-side $Al_{0.92}Ga_{0.08}As$ layer. The composition was chosen to result in an open aperture of a few micron during the oxidation time required for the DBR mirrors. At the center of the VCSEL is a λ-thick undoped GaAs cavity with three DWELL layers at the center, spaced by 15 nm.

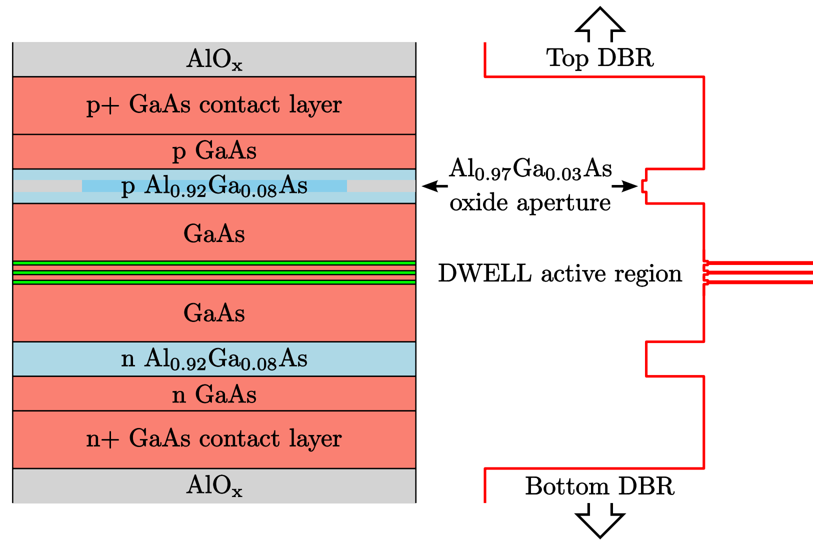

Figure 3.9: Layer structure and index of refraction profile of oxide DBR VCSEL cavity. The digital alloys and graded interfaces have been omitted for clarity.

3.3.2 Processing

The elaborate design of the electrically injected oxide DBR VCSEL requires several steps during device processing. Since light will in the end be emitted from the wafer surface, it is essential to protect it during every step. While it should be covered by a layer of photoresist (PR) most of the time, one can also choose to deposit a more permanent protective layer on top of the sample before proceeding to device manufacturing. Si_3N_4 of about 100 nm was deposited on the sample by plasma-enhanced chemical vapor deposition (PECVD) whenever we felt the extra assurance was warranted.

In a first photolithography step, a pattern of small squares is defined. In the following etch step, this will form mesas for the top DBRs of the VCSEL. To make sure the etch is just deep enough to reach the p contact layer (without removing any of it), the etch was performed in two steps: The bulk of the material is removed in an ICP etch, which is stopped in the last AlGaAs layer of the top DBR. Then the remaining AlGaAs is removed by a selective wet etch in a buffered, KOH-based developer (AZ 400K [25]). Finally, the remaining PR mask is removed with solvents. The resulting structure is schematically shown in Fig. 3.10 (a).

Next, the area for the p metallic contact is defined by photolithography. To assure good adhesion and low contact resistance of the metal, the exposed semiconductor surface is first cleaned of any remaining PR in an Oxygen plasma. This will ash any small remnants of resist in the exposed contact area, but not significantly affect the thick layer of PR used to mask the rest of the sample. Any oxide formed at the semiconductor surface is then removed by wet etching in diluted buffered HF and HCl, after which the samples are immediately loaded into the e-beam metal evaporator. Once a suitable vacuum ($\approx 2 \cdot 10^{-6}$ Torr) has been achieved, the metallic contact consisting of 50 nm Ti, 50 nm Pt, and 200 nm Au is evaporated onto the

sample. After removal from the evaporator, the sample is placed in Acetone to dissolve the PR, causing the metal from the protected areas to lift off the sample (Fig. 3.10 (b)).

Using photolithography and a second ICP etch step, a mesa is formed around the p contact as shown in Fig. 3.10 (c). This defines the surface for the n contact, but also the lateral dimensions for the formation of the oxide aperture. Oxidation is also used to insulate the contact pad, but since it is larger than the mesa around the current aperture, four extra holes are etched into the contact area to allow for complete oxidation of the buried $Al_{0.97}Ga_{0.03}As$ layer underneath the contact pad. Since the etch depth in this step is much smaller compared to the top DBR mesa, the necessary precision can be accomplished in a single ICP run.

The n contact is prepared analogous to the p contact, only the metal composition is changed to 26 nm Ge, 54 nm Au, 20 nm Ni, and 200 nm Au. The shape chosen places the n contact close to the active area, but also provides contact pads on either side of the p contact (Fig. 3.11 (a)).

The final lithography step defines 4 μm wide openings on both sides of the VCSEL mesa. Trenches are etched all the way through the bottom DBR to allow for the oxidation of its AlGaAs layers (Fig. 3.11 (b)). Due to the small width, the ICP etch rate is reduced. Fortunately, there is no harm in etching too deep, so a liberal compensation is added to the etch time.

During the wet oxidation procedure, several tasks are accomplished at once: Beginning with sample insertion into the furnace, the elevated temperature anneals the metal contacts. Once the water vapor flow is started, the top and bottom DBRs are both oxidized at the same time as the current aperture. The schematic diagram of the device after oxidation is shown in Fig. 3.11 (c); photomicrographs of test samples containing only a top DBR, current aperture, or bottom DBR are shown in Fig. 3.12.

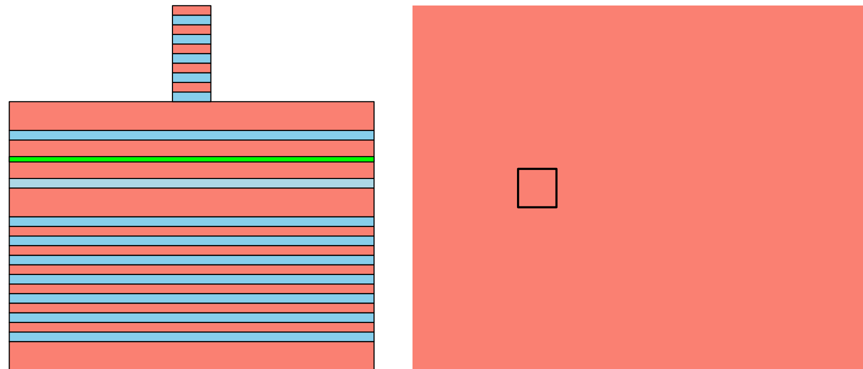

(a) Top DBR mesa etch.

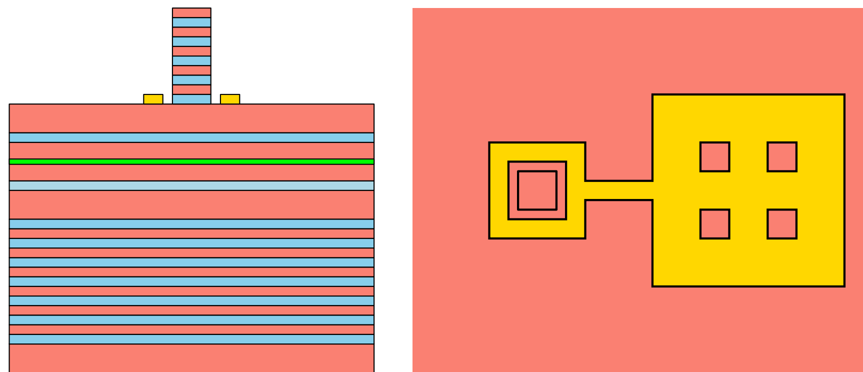

(b) P metal deposition.

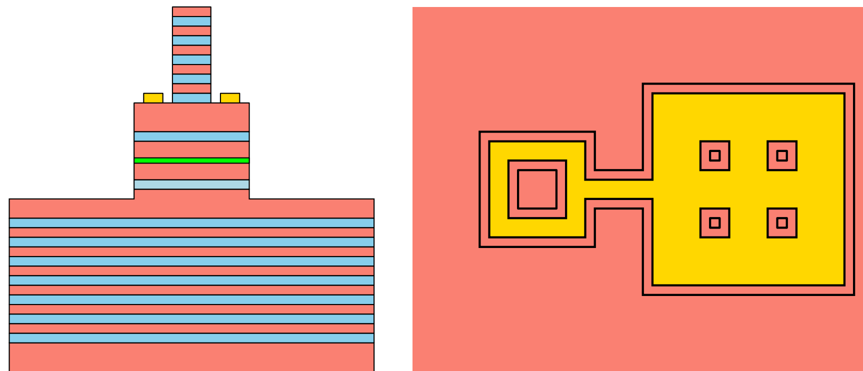

(c) Contact mesa etch.

Figure 3.10: Schematic diagrams of VCSEL processing steps.

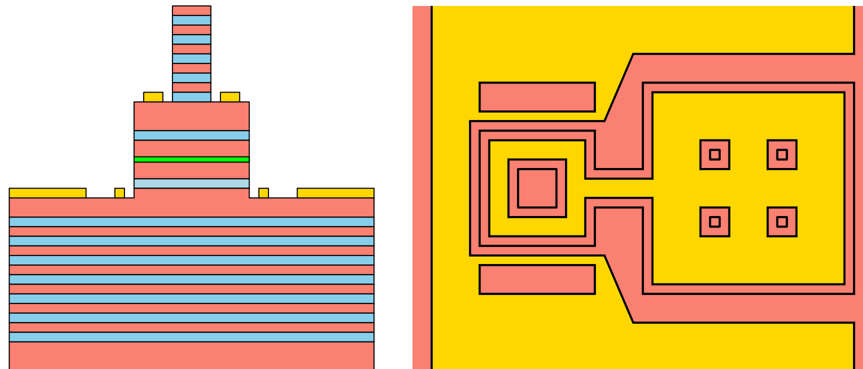

(a) N metal deposition.

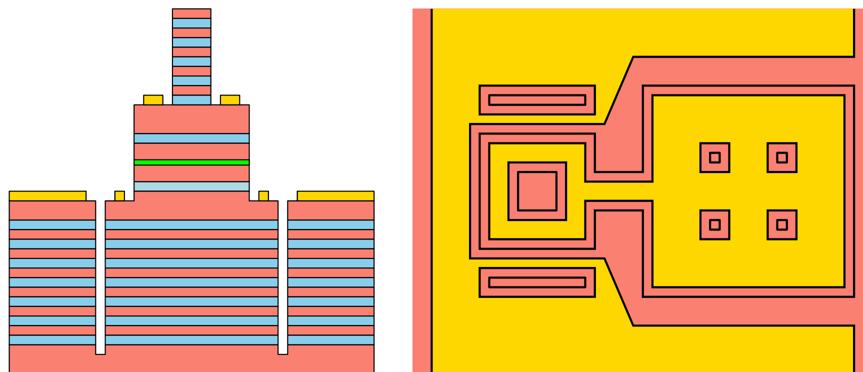

(b) Trench etch for bottom DBR.

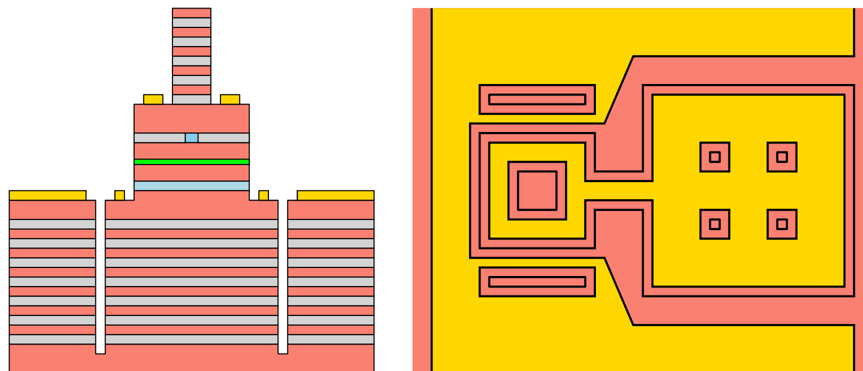

(c) Oxidation.

Figure 3.11: Schematic diagrams of VCSEL processing steps.

After the oxidation step, the small mesa of the top DBR is extremely fragile due to the strain resulting from the shrinkage of the AlGaAs. Special care needs to be taken in handling the sample from this point, to prevent any physical contact to the top DBR.

The timing of the oxidation is not very critical for the mirrors, as long as the AlGaAs is completely converted. However, the process time is crucial for the formation of the oxide aperture, which determines the size of the active area at the center of the VCSEL. Since our wet oxidation system does not allow for in-situ monitoring of the progress, several test samples are run first, all while following the operating procedure (appendix B) as precisely as possible. Once the required time is determined, the real VCSEL sample is oxidized.

To allow for a variety of aperture sizes in one oxidation run, the mask design incorporates devices with several different contact mesa sizes, from (56 μm)^2 square in 4 μm steps to (72 μm)^2. Assuming the smallest mesa has a 2 μm aperture after oxidation, the current apertures in the other devices should each be larger by about 4 μm, resulting in a maximum aperture of (18 μm)^2. A test structure to observe all the different aperture sizes after oxidation was also included on the mask, a photomicrograph of which is shown in Fig. 3.13.

Finally, if a protective Si_3N_4 was deposited by PECVD before processing, it is now removed in a CF_4 and O_2 plasma, and the VCSEL is ready for testing. A photo of a completely processed device is shown in Fig. 3.14.

3.3.3 Experimental Setup

One of the advantages of a VCSEL over edge-emitting lasers is the ease of testing. After processing, without the need to cleave or mount the devices, every single VCSEL on the chip can be characterized. To allow for temperature dependent measurements,

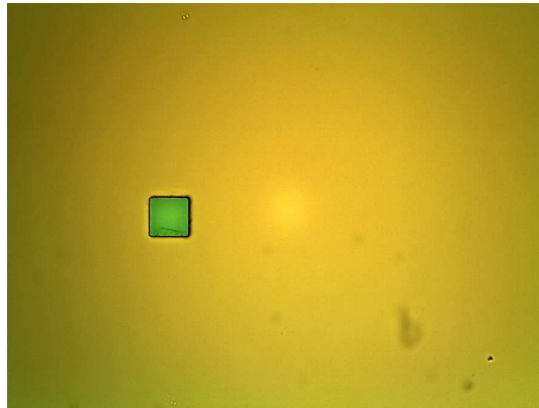

(a) Top DBR.

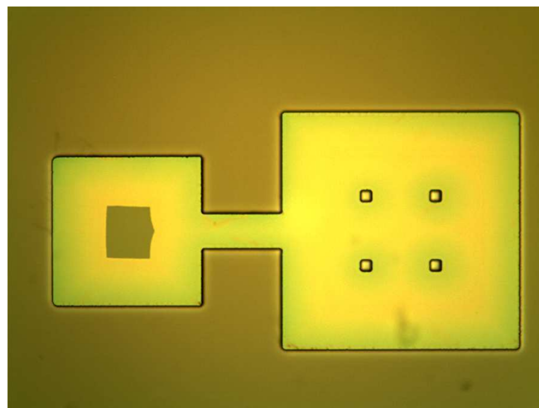

(b) Contact mesa with current aperture.

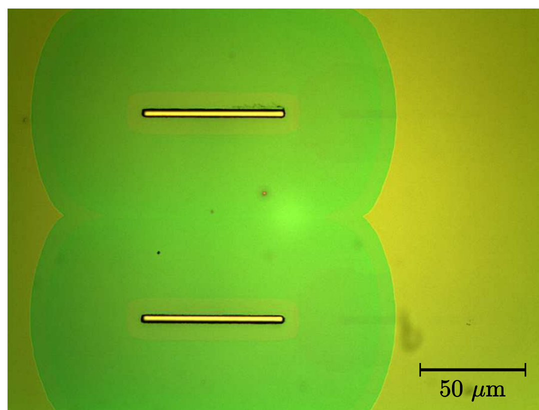

(c) Trenches for bottom DBR.

Figure 3.12: Photomicrographs of oxidation test samples.

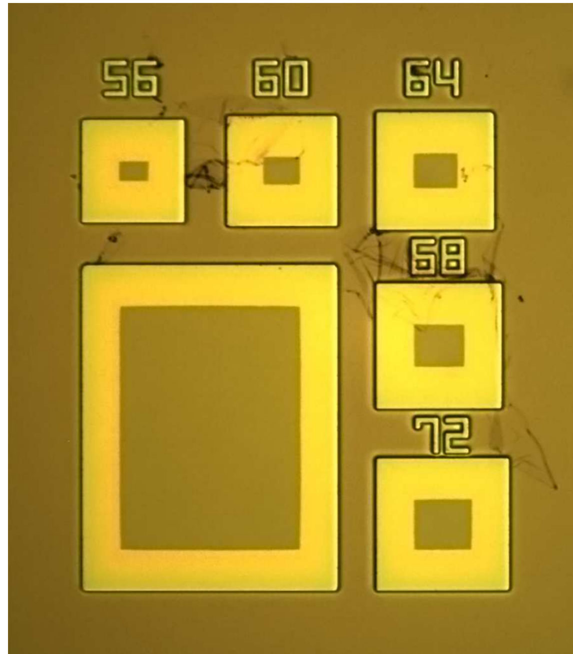

Figure 3.13: Photomicrograph of oxidized test structure, the numbers included on the sample indicate mesa size in micron.

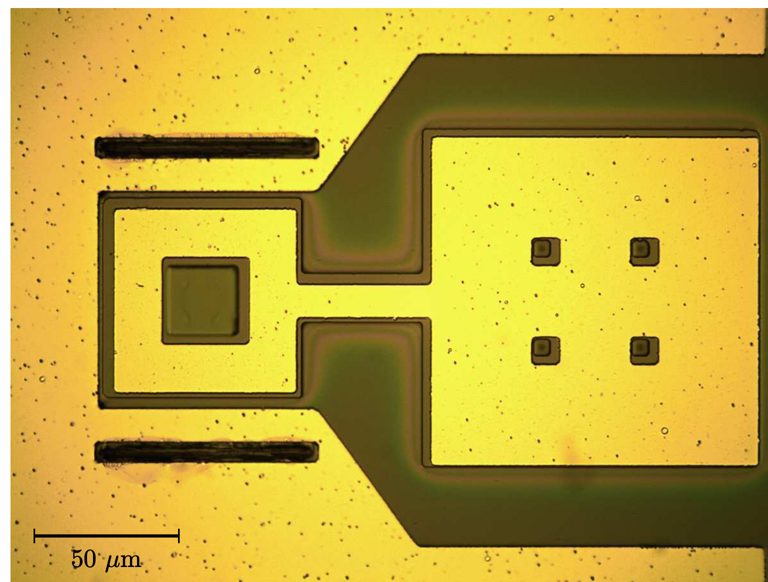

Figure 3.14: Photomicrograph of oxide DBR VCSEL diode after processing.

the sample is placed on a TE-cooled heatsink. Probe tips are placed on the p and n contact pads to inject current and measure the voltage drop across the device. The emitted light can be collected free-space by an optical power meter 5–10 mm above the sample. For spectral measurements, a multimode optical fiber can be placed on top of the VCSEL instead, to guide the light to an optical spectrum analyzer.

3.3.4 Experimental Results

Testing of the processed VCSEL diodes revealed several problems: While the electrical properties of the devices were promising, the amount of light emitted was minimal, almost too low to measure. In addition, the devices were very prone to fail: If too large of a current was applied, the light output would cease permanently, without affecting the electrical properties much, sometimes even lowering the voltage drop across the device. One possible explanation for this might be the Be doping close to the cavity: Be is known to diffuse in GaAs [26] and with the close proximity of the p doping to the DWELL layers, it may be possible for Be to partially short out the active region, allowing current to flow without recombination in the QDs.

Another problem was discovered by manufacturing a test structure without top DBR — essentially a light-emitting diode. Output power and voltage across the device as function of current are shown in Fig. 3.15. More interestingly, the electroluminescence spectrum in Fig. 3.16 shows a peak emission wavelength of 1325 nm, despite the test sample's location close to the edge of the wafer. This points toward a significant misalignment of the QD gain peak with the cavity mode around 1300 nm, which might explain the poor optical performance and the failure to achieve lasing operation. One possible explanation might again be the Be doping diffusion, which my have been incorporated in some of the QDs, shifting their emission wavelength.

In addition, the use of only three DWELL layers in the active region might have

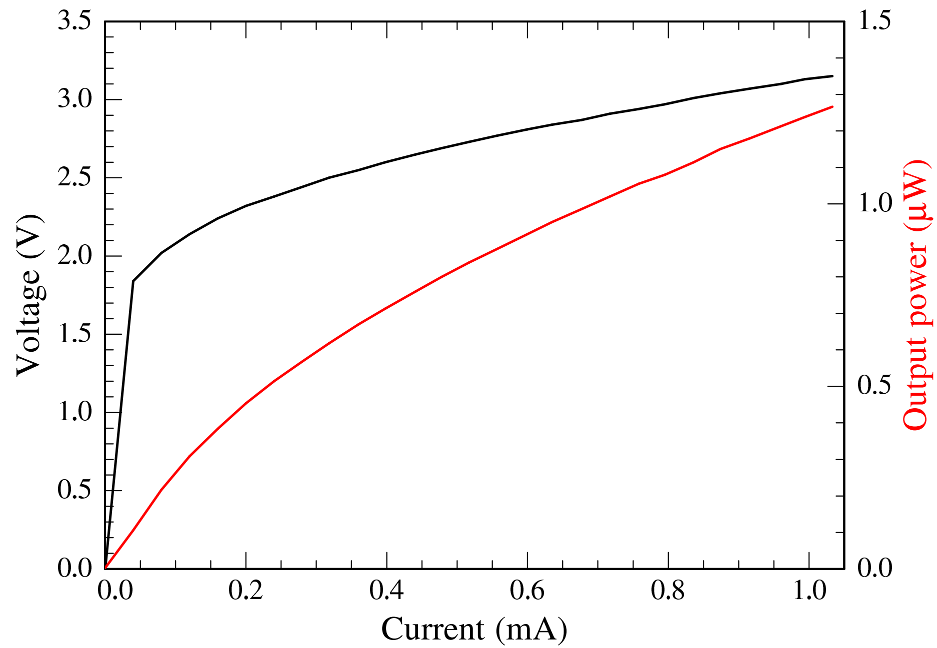

Figure 3.15: Output power and voltage as function of current for oxide DBR VCSEL test structure (no top DBR).

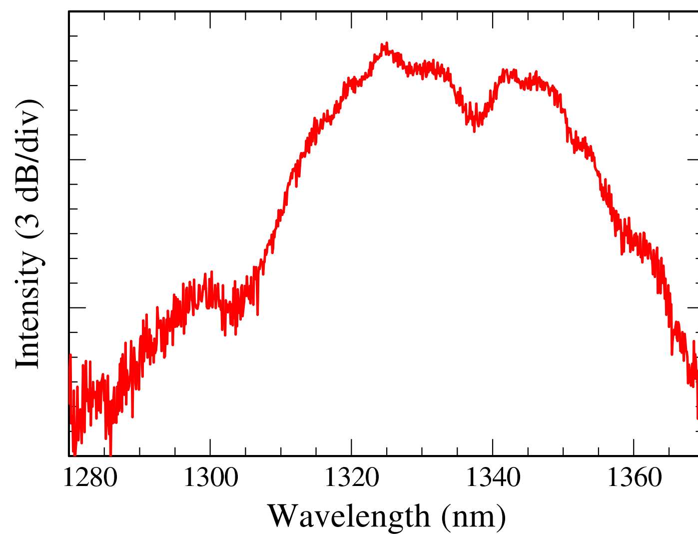

Figure 3.16: Electroluminescence spectrum from oxide DBR VCSEL test structure (no top DBR).

been somewhat optimistic, especially considering the increased absorption due to the high dopant concentration in the intra-cavity contact layers close to the gain medium. While the number of QD layers could easily be increased, the problem of Be doping diffusion is more serious. Carbon can be used as p-type dopant in GaAs, and has demonstrated good device performance in VCSELs [11]. Despite being able to acquire a Carbon source for our MBE, financial constraints have prevented its installation to this day, forcing a departure from the oxide DBR and intra-cavity contact VCSEL design.

3.4 Semiconductor DBR Electrically Injected VCSEL

A more standard approach to VCSEL design is to use AlGaAs/GaAs semiconductor DBRs. While this requires a larger number of mirror pairs, resulting in much longer MBE growth time, semiconductor DBRs can be doped and used to deliver current to the active region. This allows to design devices with a significantly smaller number of processing steps required, leading to a more rapid turnaround for testing different active regions.

3.4.1 Design

Ideally, the mirrors should be AlAs/GaAs, for the highest difference in index of refraction between the layers. But since the device still relies on an oxide current aperture, this requires any AlAs layers in the VCSEL to be protected during wet oxidation, which would involve extra processing steps. Instead, the low index material was changed to $Al_{0.9}Ga_{0.1}As$, which does not oxidize much during the time required to form the current aperture. With this material composition, 27 and 36 pairs were

utilized in the top and bottom DBR, respectively, to provide sufficient reflectivity values.

Since the current will be injected through the DBRs, they need to be doped. As in the case of the oxide DBR VCSEL design, one has to worry about minimizing free carrier absorption. The top DBR is the p contact of the device. The topmost mirror pair was Be-doped to a concentration of $p = 1.5 \cdot 10^{19}$ cm^{-3} to allow for a good ohmic contact. The dopant level was reduced to $p = 5 \cdot 10^{18}$ cm^{-3} in the next two layers, and to $p = 2 \cdot 10^{18}$ cm^{-3} for most of the DBR. Three mirror pairs above the cavity, where the amplitude of the standing wave is already much larger, the doping level was further reduced to $p = 5 \cdot 10^{17}$ cm^{-3}, while the GaAs cavity was undoped.

The bottom DBR is n-doped with Si at $n = 5 \cdot 10^{17}$ cm^{-3} for the first three DBR pairs after the cavity. For the rest of the bottom mirror, the dopant level was $n = 2 \cdot 10^{18}$ cm^{-3}. The n metal contact will be applied to the backside of the n-doped GaAs substrate.

Due to the performance problems encountered with the oxide DBR VCSEL, several changes were incorporated in the active region design: The emission wavelength of the QDs was reduced to 1250 nm, which provides higher gain due to greater QD density. In addition, the amount of In per DWELL is also reduced, resulting in lower strain, higher material quality and the ability to stack a larger number of DWELL layers in the structure. For this structure, a total of twelve DWELL layers were placed inside the cavity. The four groups of three QD layers were spaced by $\lambda/2$, to place them at adjacent antinodes of the electrical field standing wave pattern. The index profile and calculated field strength are shown in Fig. 3.17, a magnified view of the cavity area in Fig. 3.18. Note the oxide aperture layer incorporated into the first low-index layer on top of the GaAs cavity.

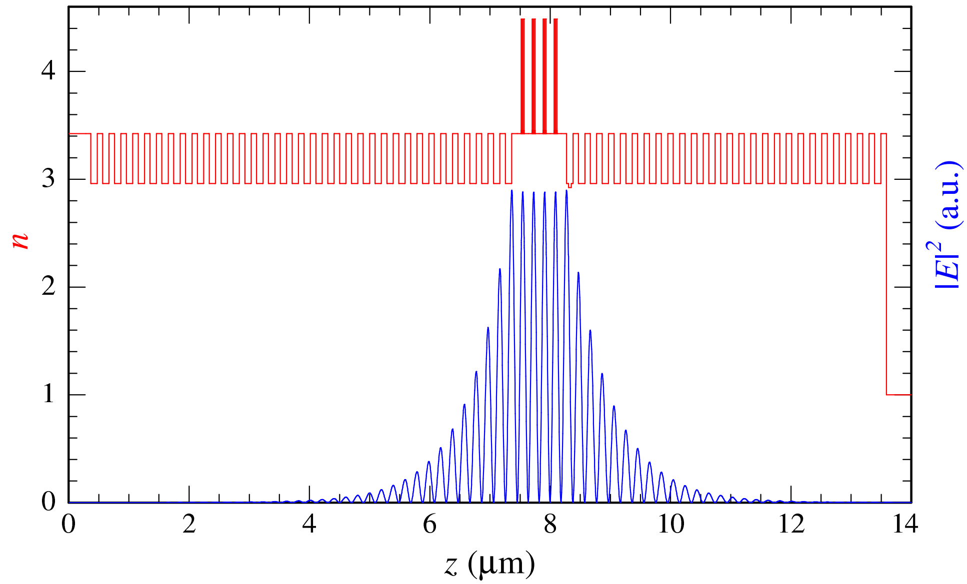

Figure 3.17: Refractive index n and electric field $|E|^2$ of the semiconductor DBR VCSEL sample.

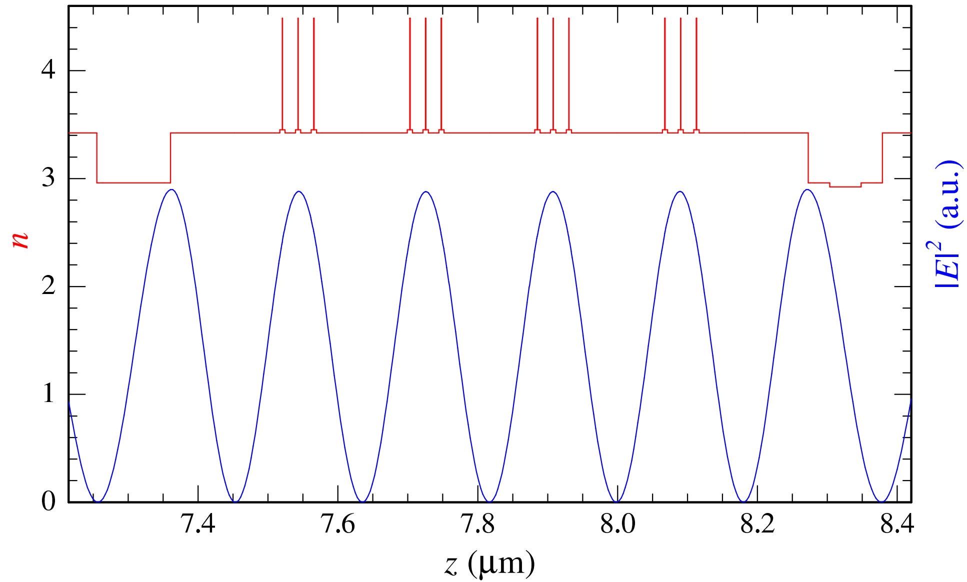

Figure 3.18: Refractive index n and electric field $|E|^2$ of the semiconductor DBR VCSEL sample, magnified view of cavity, showing placement of the DWELL layers.

3.4.2 Processing

Processing of the semiconductor DBR VCSEL is greatly simplified compared to the oxide DBR structure. The p metal contact is formed by patterning the sample using photolithography, depositing 50 nm Ti, 50 nm Pt, and 200 nm Au on top of the full layer structure, and lift-off from the layers protected by PR. The n metal, consisting of 26 nm Ge, 54 nm Au, 20 nm Ni, and 200 nm Au, is deposited onto the backside of the substrate, no patterning is needed.

Only a single etch step is required to define the lateral dimensions of the device and expose the buried oxide aperture layer. Unfortunately, when trying to use the corresponding layer of the oxide DBR mask set (Fig. 3.10 (c)) to define the mesa structure for the semiconductor DBR VCSEL, a problem was encountered: The four little holes designed to oxidize the current aperture layer underneath the contact pad were too small for the required etch depth of over 5 μm.

A new mask set was designed, which does not rely on holes. Instead, the contact pad size was been reduced to allow for complete oxididation in the time required to form the current aperture. The oxidation followed the same procedure as for the previous sample. However, since now the current aperture is underneath the entire 5 μm thick top DBR, it is now difficult to observe the extend of the oxidation with an optical microscope. Test patterns (as in the case of the oxide DBR VCSEL) would now require an additional lithography and etch step and were therefore not incorporated into the mask. Instead, the size of the oxide aperture was measured with an IR microscope: The light from an incandescent light bulb was passed through a 900 nm long pass filter. The remaining spectrum in the IR is below the bandgap energy of the GaAs and AlGaAs layers in the DBR and can penetrate the sample without much absorption. The resulting image is observed using a Si CCD camera, with the extend of the oxidation clearly visible, as seen in Fig. 3.19.

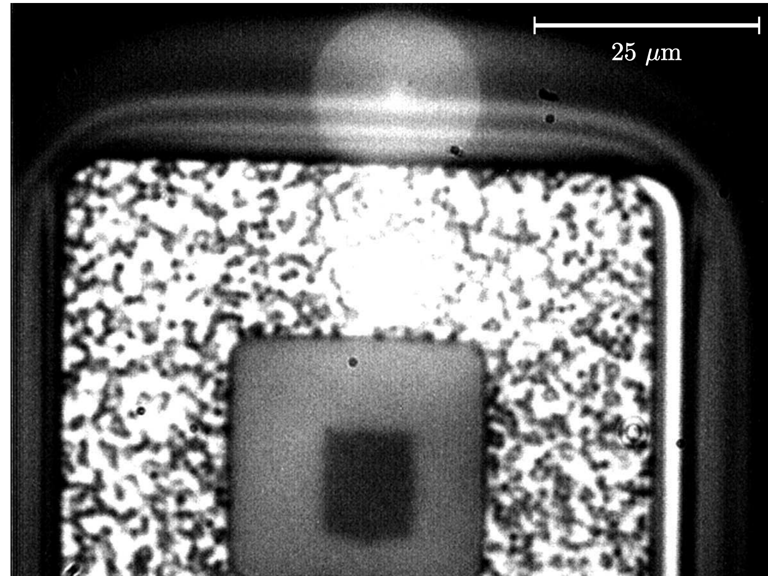

Figure 3.19: IR ($\lambda > 900$ nm) photomicrograph of semiconductor DBR VCSEL oxide aperture.

Fig. 3.20 shows an optical micrograph of two processed devices. While the small contact pad area of the new mask design requires more accuracy when contacting the device with a probe tip, or by wire bonding, the continuous metal contact (without the holes) actually proved to be a more reliable way to inject current into the device. A scanning electron microscope (SEM) image of a wire-bonded VCSEL array is shown in Fig. 3.21.

3.4.3 Experimental Setup

The experimental setup is almost identical to the case of the oxide DBR devices, the only exception being the n contact of the VCSEL diodes, which is formed by the whole backside of the substrate. Electrical contact is made by placing the sample on a gold-plated heatsink which is connected to the diode driver output.

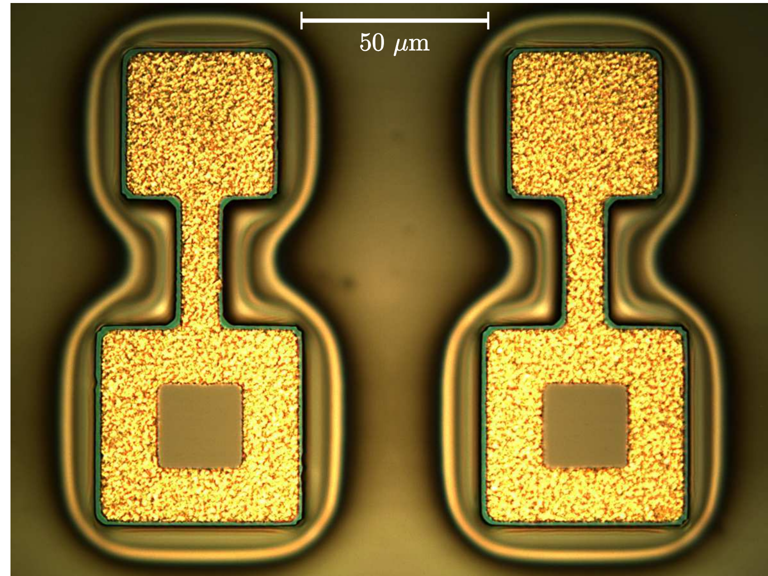

Figure 3.20: Photomicrograph of two semiconductor DBR VCSEL diodes after processing.

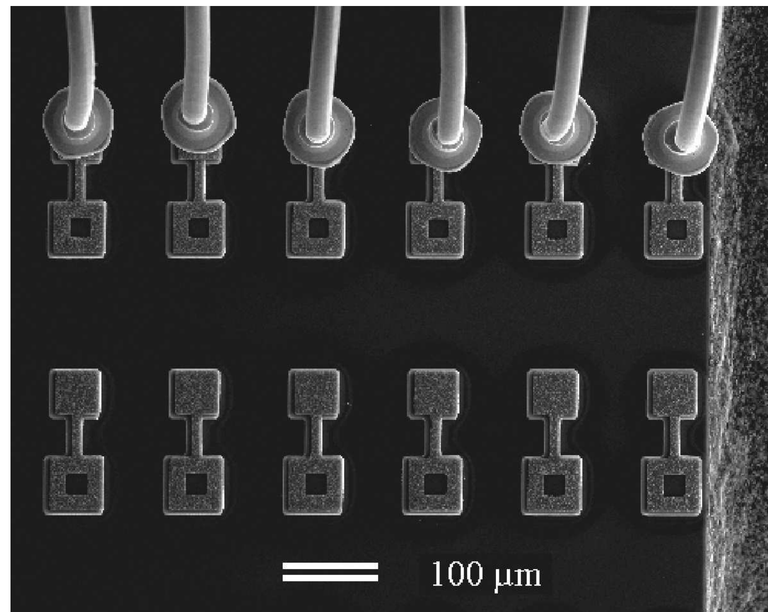

Figure 3.21: SEM image of wire-conded semiconductor DBR VCSEL array.

3.4.4 Experimental Results

Wafer Characterization

Semiconductor DBRs do not require processing, so large area FTIR reflectivity spectra can be utilized to assess the optical properties of the MBE-grown wafers. Reflectance measurements for the first semiconductor DBR VCSEL sample, grown on a three inch GaAs substrate, as function on the position on the wafer are shown in Fig. 3.22.

Due to the large (approximately 4 mm square) area of the FTIR reflectance setup, effectively averaging this area, the cavity resonance is not as sharp or deep as expected. However, its wavelength can be determined from the data. Since on the first wafer (A) this wavelength was close to 1285 nm at the center of the wafer, much longer than the peak of the QD emission at 1250 nm, a second wafer (B) was grown with reduced growth rates for GaAs and AlGaAs. The wavelength of the cavity mode as a function of the position on the wafer, as extracted from FTIR reflectance spectra, for both wafers is shown in Fig. 3.23.

Electrical and Optical Characterization

During electrical characterization of the processed VCSEL samples, it was found that the emission from 1250 nm QD devices was visible on a Si CCD camera (see appendix C). A photomicrograph of a lasing semiconductor DBR VCSEL is shown in Fig. 3.24. This proved to be very useful for measuring the size of the oxide aperture: By turning off the microscope illuminator and operating the VCSEL below threshold, as to not saturate the CCD camera, an image of the current aperture inside the VCSEL diode could easily be captured. An example is shown in Fig. 3.25.

Optical output power and voltage across the device were measured in CW op-

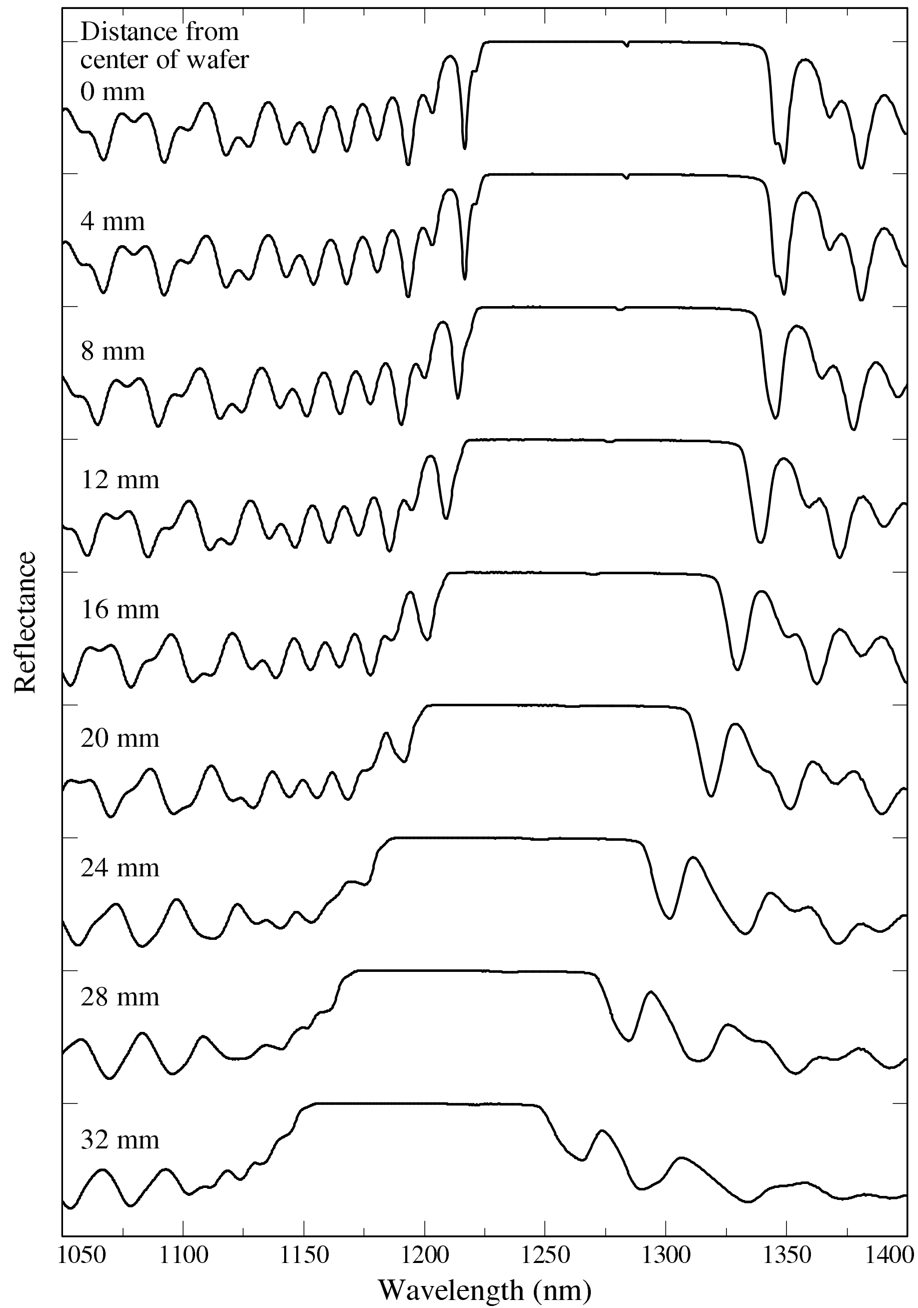

Figure 3.22: FTIR reflectance spectra as function of the position on the semiconductor DBR VCSEL wafer.

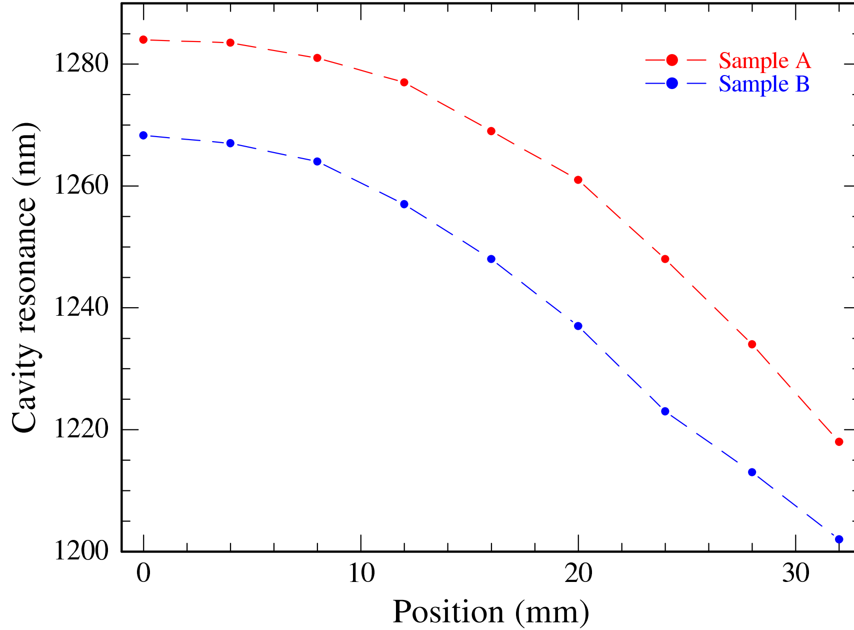

Figure 3.23: Wavelength of cavity mode as function of position on the wafer, measured radially from the center of the wafer.

eration for several areas of the samples. Unless otherwise noted, experiments were performed at a heatsink temperature of 20°C.

For wafer A, devices near the center of the substrate did not reach lasing threshold, because of the misalignment between DBR and gain wavelength. Devices approximately 25 mm from the center operated at a wavelength of 1230-1240 nm. Output power and voltage measurements for a device with a 4 μm^2 oxide aperture area are shown in Fig. 3.26, spectra for two different drive currents close to and above threshold are shown in Fig. 3.27.

VCSEL diodes with such small apertures exhibit low threshold currents, since only a small area of the active region is supplied with carriers. However, they suffer the most from optical scattering losses, resulting in low efficiency and limited output powers. At the same time, the electrical properties suffer as well, evident in the high voltage drop across the device.

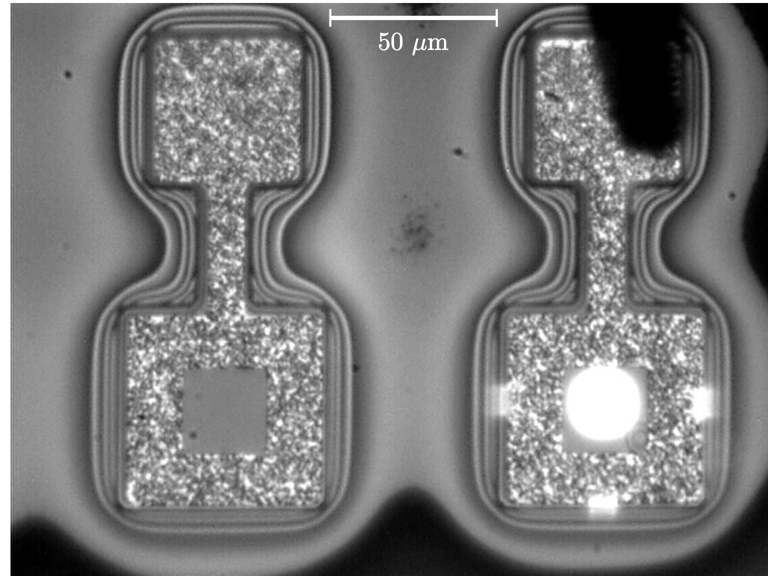

Figure 3.24: Photomicrograph of two VCSEL devices, with the right one lasing. The dark, out of focus object in the top right corner is the probe tip used to inject the current.

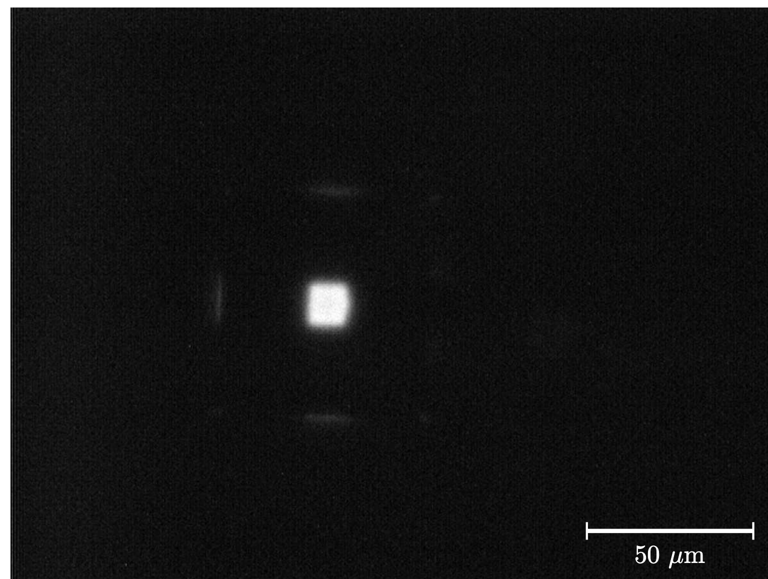

Figure 3.25: Photomicrograph of VCSEL device operating below threshold. The size of the oxide aperture is clearly visible.

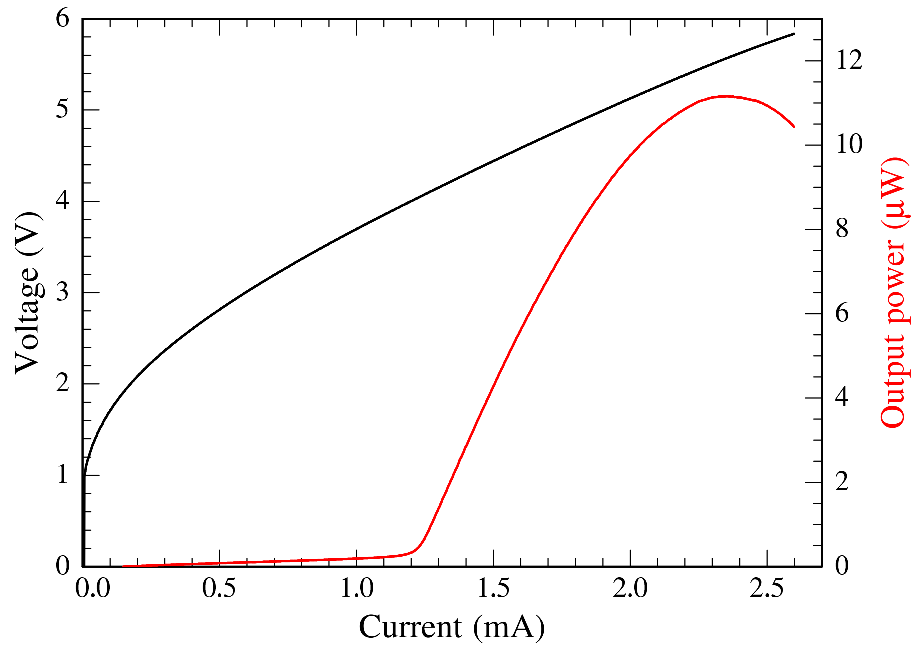

Figure 3.26: Output power and voltage as function of current for 4 μm^2 aperture device from wafer A.

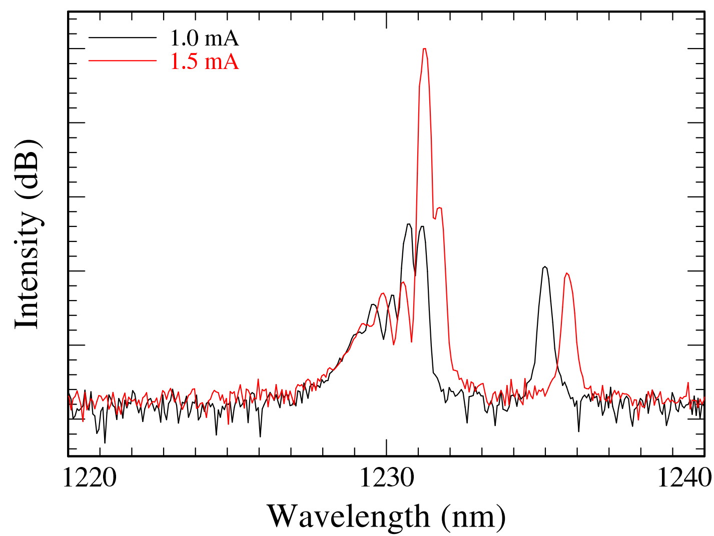

Figure 3.27: Lasing spectra for 4 μm^2 aperture device from wafer A.

For comparison, Fig. 3.28 contains output power and voltage measurements for a much larger device from the same wafer, with an oxide aperture area of 240 μm^2. Emission spectra for two different currents are shown in Fig. 3.29.

In addition, devices about 32 mm from the center of the wafer (at the very edge) were also lasing, now at a wavelength of 1200 nm. The output power of the larger aperture VCSEL diodes reached close to 1 mW CW at 20°C and above 1 mW for heatsink temperatures of 10°C or below. Measurement results for a device similar in size to the one in Fig. 3.28 are shown in Fig. 3.30, the lasing spectrum in Fig. 3.31.

On wafer B, despite the slightly better alignment between gain peak and cavity mode, devices near the center did not reach lasing threshold. Devices close to the edge of the samples exhibited best performance. Achievable output powers were comparable to wafer A, the device threshold currents, however, were significantly lower for wafer B, with the smaller devices reaching threshold currents as low as 250 μA. Measurements from one device can be seen in Fig. 3.32, the emission spectrum at a wavelength close to 1210 nm in Fig. 3.33.

Threshold current densities are calculated for the different devices by dividing the threshold current values by the size of the oxide aperture as determined from the microscope images. The values for different VCSEL diodes from both samples are shown in Fig. 3.34. Both curves exhibit the same trend of decreasing threshold with increasing devices size, where scattering losses are minimized and electrical properties improve. Wafer B clearly exhibits better performance with threshold current densities below 500 Acm^{-2} for the largest devices.

While values of $j_{th} = 170$ Acm^{-2} were reported for short wavelength (≈ 1 μm) QD VCSELs [14], we believe our results to be the lowest threshold current density for long wavelength (> 1.2 μm) QD VCSEL diodes.

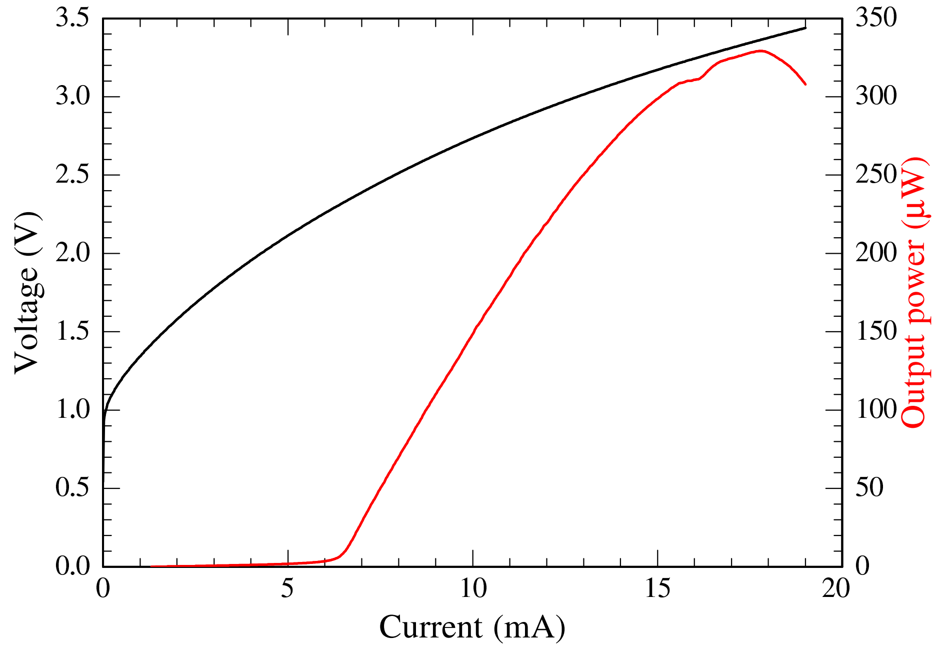

Figure 3.28: Output power and voltage as function of current for 240 μm^2 aperture device 25 mm from the center of wafer A.

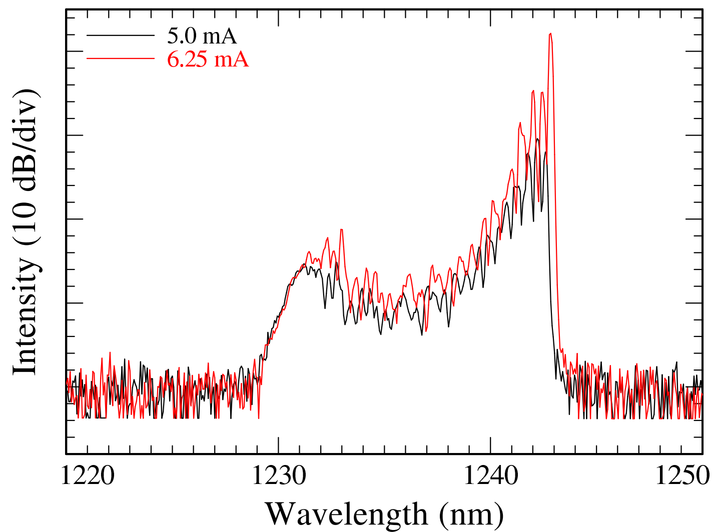

Figure 3.29: Lasing spectra for 240 μm^2 aperture device 25 mm from the center of wafer A.

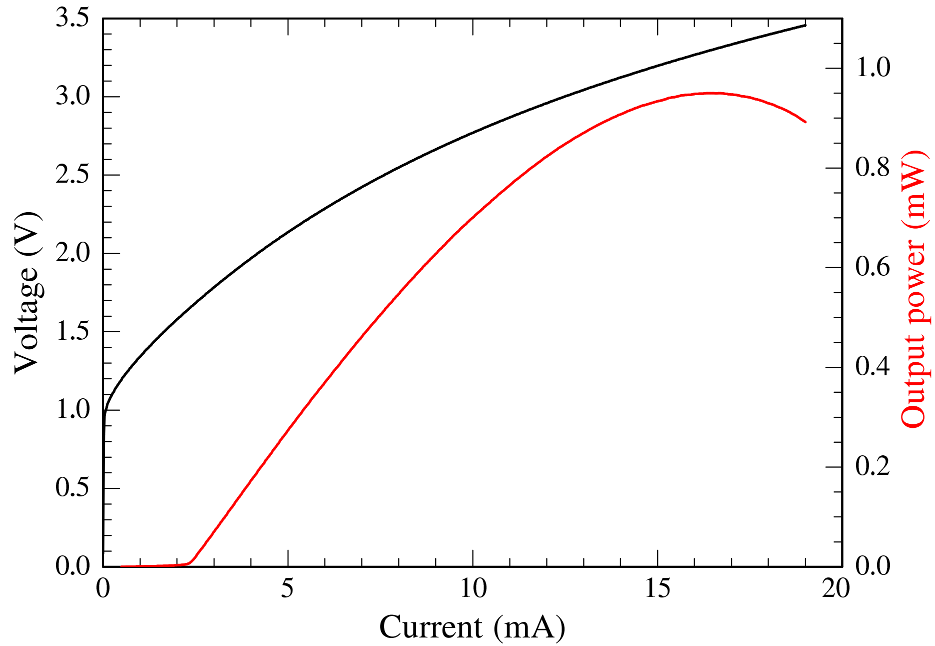

Figure 3.30: Output power and voltage as function of current for 225 μm^2 aperture device 32 mm from the center of wafer A.

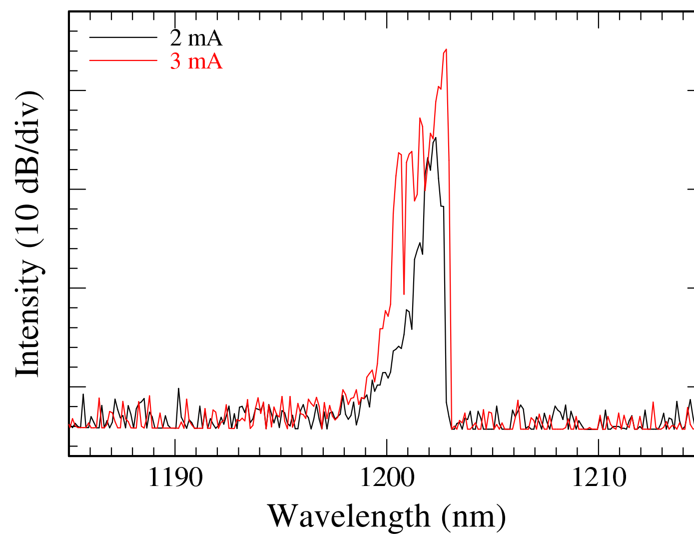

Figure 3.31: Lasing spectra for 225 μm^2 aperture device 32 mm from the center of wafer A.

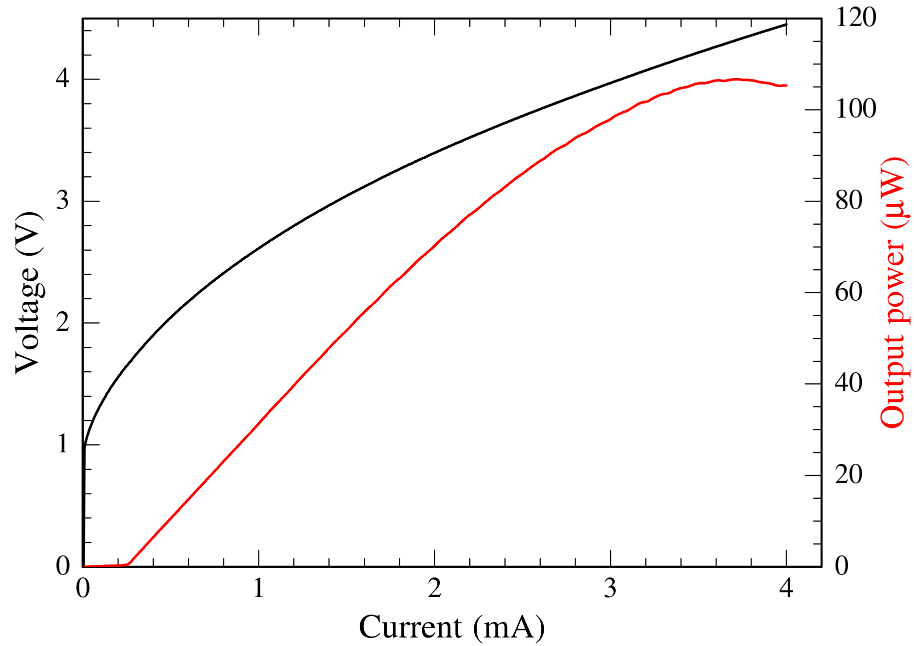

Figure 3.32: Output power and voltage as function of current for 18 μm^2 aperture device from wafer B.

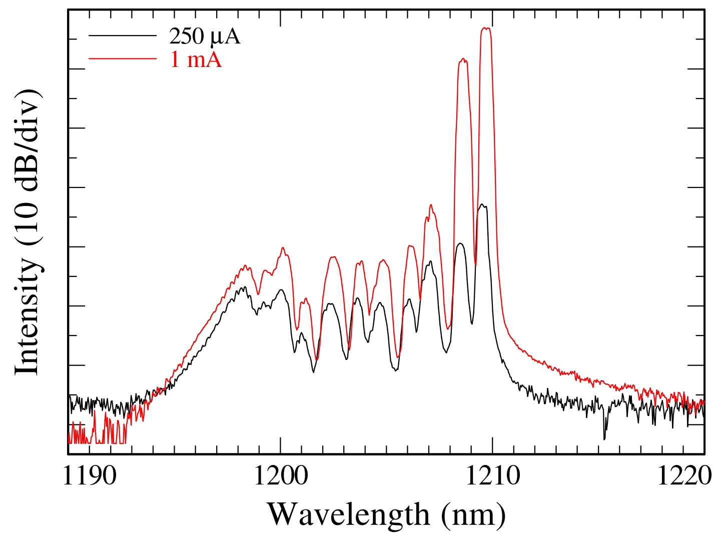

Figure 3.33: Lasing spectra for 18 μm^2 aperture device from wafer B.

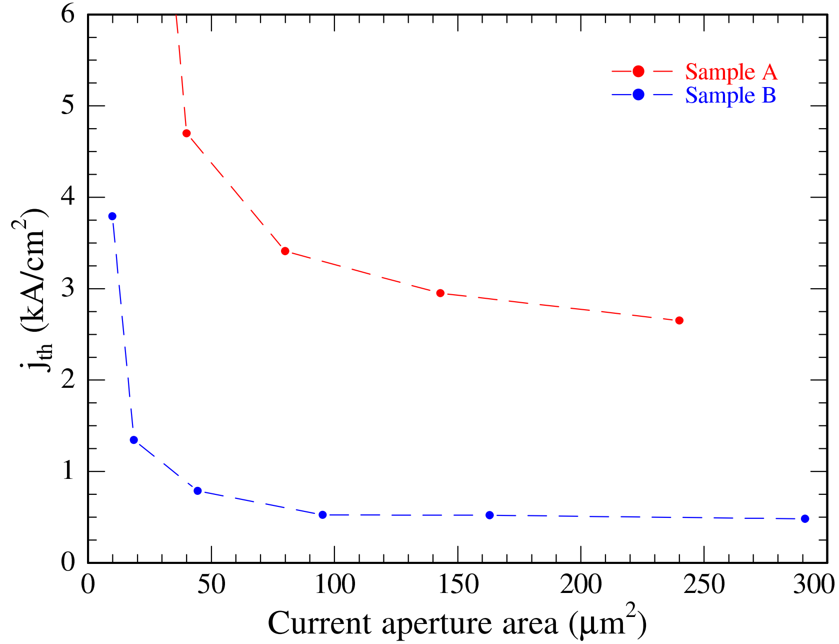

Figure 3.34: Threshold current density j_{th} as function of current aperture area for a number of devices from both wafers.

Polarization

The polarization of the VCSEL diodes was investigated by placing a film polarizer between the laser and the optical power meter. The angle of the polarizer was then adjusted to achieve the smallest output power from the device and the value compared to the power with the polarizer rotated 90° from there. All measured devices were found to be strongly polarized along the [110] crystal direction of the GaAs substrate, with output powers about a factor of 20 higher than in the perpendicular direction. This did not change significantly with the drive current. The direction of polarization agrees with previous findings on QD samples [27]. An example for the device polarization is shown in Fig. 3.35.

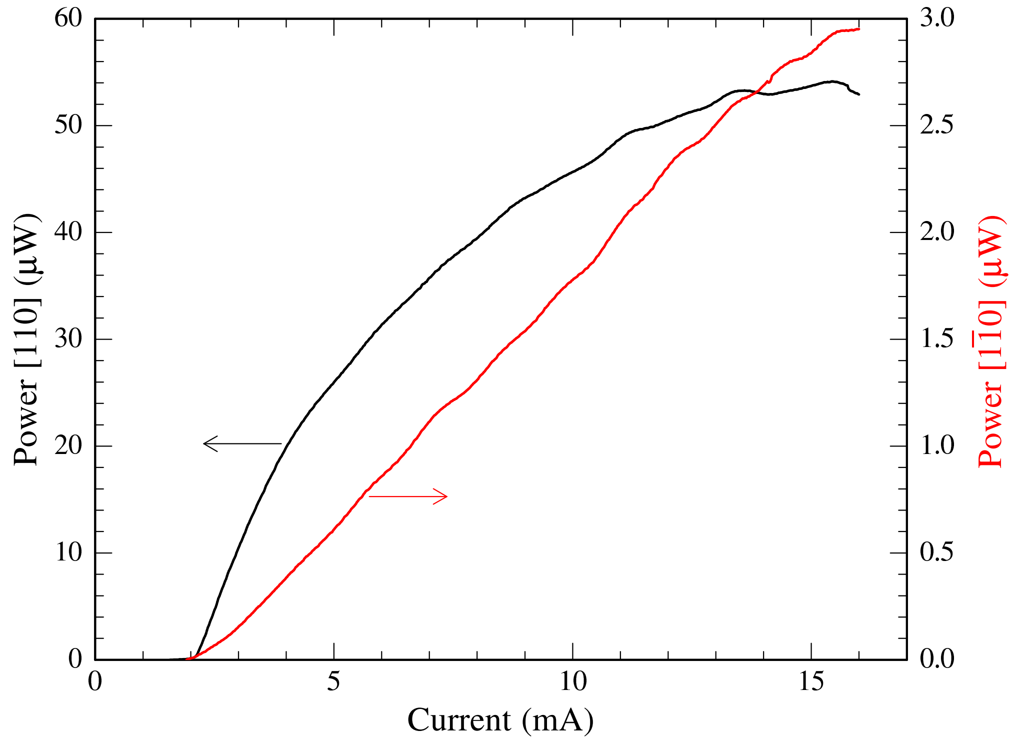

Figure 3.35: VCSEL output power vs. current for [110] and [$1\bar{1}0$] polarization direction, showing a roughly 20:1 ratio.

Temperature Dependent Properties

Temperature dependent device performance was investigated by placing the VCSEL diodes on a temperature controlled heatsink. CW lasing was observed at elevated temperatures up to 75°C, as seen in Fig. 3.36.

3.5 Conclusions

An optically pumped QD VCSEL with top and bottom GaAs/AlO_x DBRs was designed, MBE-grown, and processed. CW lasing operation at room temperature was achieved at a wavelength close to 1310 nm. Output powers were limited, probably

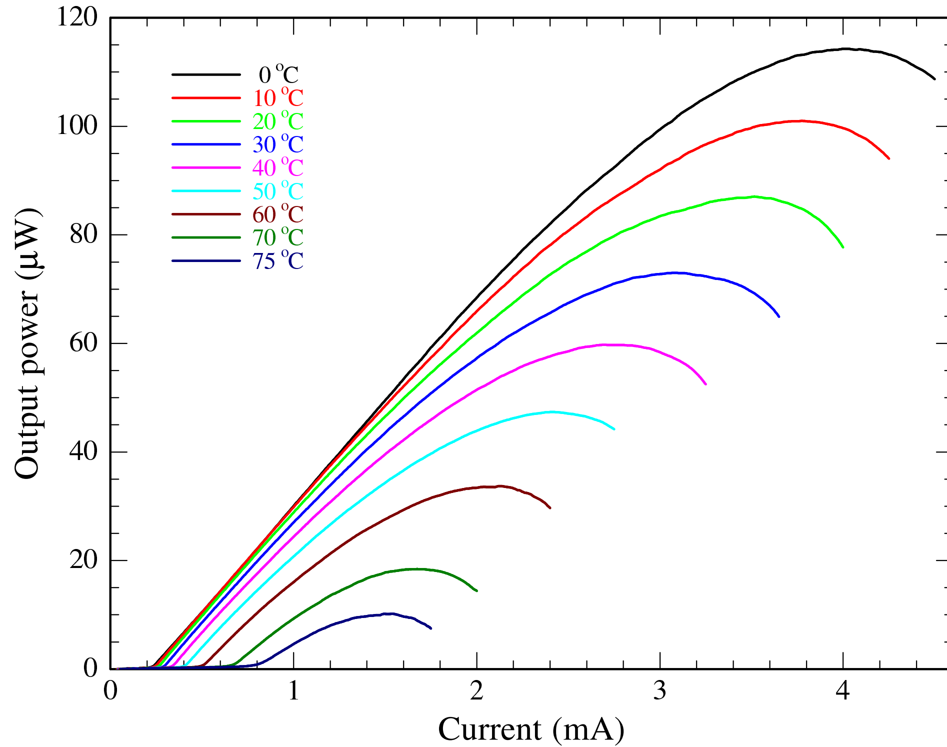

Figure 3.36: VCSEL output power vs. current for heatsink temperatures from 0°C to 75°C.

due to the small aperture size.

For electrically injected devices with oxide mirrors, an elaborate device design with double intra-cavity contacts and an oxide aperture for current confinement was investigated. VCSEL diodes were successfully processed and showed good electrical properties. Lasing threshold was not reached, likely due to a lack of gain from the three DWELL layers.

An all-semiconductor DBR VCSEL was designed to speed up turnaround for electrical device processing. For higher gain, the active region was changed to QDs of a shorter wavelength, providing higher QD density and gain. In addition, the number of DWELL layers in the active region was increased from three to twelve.

Devices were processed and characterized. Room temperature CW operation was achieved in a wavelength range from 1200–1240 nm. Output powers in excess of 1 mW were observed for heatsink temperatures below 10 °C.

Threshold current densities for devices around 1210 nm were below 500 Acm^{-2}, which we believe to be the lowest reported values for QD VCSELs with an emission wavelength longer than 1.2 μm.

References

[1] Corning Inc. Corning smf-28 ull optical fiber product information, August 2008. `http://www.corning.com/WorkArea/showcontent.aspx?id=14357`.

[2] Corning Inc. Corning smf-28e xb optical fiber product information, October 2008. `http://www.corning.com/WorkArea/showcontent.aspx?id=16913`.

[3] L.G. Cohen, Chinlon Lin, and W.G. French. Tailoring zero chromatic dispersion into the 1.5 - 1.6 μm low-loss spectral region of single-mode fibres. *Electronics Letters*, 15(12):334–335, 7 1979.

[4] K. Tai, G. Hasnain, J.D. Wynn, R.J. Fischer, Y.H. Wang, B. Weir, J. Gamelin, and A.Y. Cho. 90% coupling of top surface emitting GaAs/AlGaAs quantum well laser output into 8 μm diameter core silica fibre. *Electronics Letters*, 26(19):1628–1629, Sept. 1990.

[5] C. Jung, R. Jager, M. Grabherr, P. Schnitzer, R. Michalzik, B. Weigl, S. Muller, and K.J. Ebeling. 4.8 mW singlemode oxide confined top-surface emitting vertical-cavity laser diodes. *Electronics Letters*, 33(21):1790–1791, Oct 1997.

[6] V. Jayaraman, M. Mehta, A.W. Jackson, S. Wu, Y. Okuno, J. Piprek, and J.E. Bowers. High-power 1320-nm wafer-bonded VCSELs with tunnel junctions. *Photonics Technology Letters, IEEE*, 15(11):1495–1497, Nov. 2003.

[7] T. Anan, K. Nishi, S. Sugou, M. Yamada, K. Tokutome, and A. Gomyo. GaAsSb: A novel material for 1.3 μm VCSELs. *Electronics Letters*, 34(22):2127–2129, Oct 1998.

[8] F. Quochi, D.C. Kilper, J.E. Cunningham, M. Dinu, and J. Shah. Continuous-wave operation of a 1.3-μm GaAsSb-GaAs quantum-well vertical-cavity surface-emitting laser at room temperature. *Photonics Technology Letters, IEEE*, 13(9):921–923, Sep 2001.

[9] T. Anan, M. Yamada, K. Nishi, K. Kurihara, K. Tokutome, A. Kamei, and S. Sugou. Continuous-wave operation of 1.30 μm GaAsSb/GaAs VCSELs. *Electronics Letters*, 37(9):566–567, Apr 2001.

[10] K.D. Choquette, J.F. Klem, A.J. Fischer, O. Blum, A.A. Allerman, I.J. Fritz, S.R. Kurtz, W.G. Breiland, R. Sieg, K.M. Geib, J.W. Scott, and R.L. Naone. Room temperature continuous wave InGaAsN quantum well vertical-cavity lasers emitting at 1.3 μm. *Electronics Letters*, 36(16):1388–1390, Aug 2000.

[11] H. Riechert, A. Ramakrishnan, and G. Steinle. Development of InGaAsN-based 1.3 μm VCSELs. *Semiconductor Science Technology*, 17:892–897, August 2002.

[12] J. Jewell, L. Graham, M. Crom, K. Maranowski, J. Smith, T. Fanning, and M. Schnoes. Commercial GaInNAs VCSELs grown by MBE. *physica status solidi (c)*, 5(9):2951–2956, 2005.

[13] G. Liu, A. Stintz, H. Li, K.J. Malloy, and L.F. Lester. Extremely low room-temperature threshold current density diode lasers using InAs dots in $In_{0.15}Ga_{0.85}As$ quantum well. *Electronics Letters*, 35(14):1163–1165, Jul 1999.

[14] J.A. Lott, N.N. Ledentsov, V.M. Ustinov, A.Yu. Egorov, A.E. Zhukov, P.S. Kop'ev, Zh.I. Alferov, and D. Bimberg. Vertical cavity lasers based on vertically coupled quantum dots. *Electronics Letters*, 33(13):1150–1151, Jun 1997.

[15] D. L. Huffaker, O. Baklenov, L. A. Graham, B. G. Streetman, and D. G. Deppe. Quantum dot vertical-cavity surface-emitting laser with a dielectric aperture. *Applied Physics Letters*, 70(18):2356–2358, 1997.

[16] I.N. Kaiander, F. Hopfer, T. Kettler, U.W. Pohl, and D. Bimberg. Alternative precursor growth of quantum dot-based VCSELs and edge emitters for near infrared wavelengths. *Journal of Crystal Growth*, 272(1-4):154 – 160, 2004. The Twelfth International Conference on Metalorganic Vapor Phase Epitaxy.

[17] J.A. Lott, N.N. Ledentsov, V.M. Ustinov, N.A. Maleev, A.E. Zhukov, A.R. Kovsh, M.V. Maximov, B.V. Volovik, Zh.I. Alferov, and D. Bimberg. InAs-InGaAs quantum dot VCSELs on GaAs substrates emitting at 1.3 μm. *Electronics Letters*, 36(16):1384–1385, 2000.

[18] N.N. Ledentsov. Long-wavelength quantum-dot lasers on GaAs substrates: from media to device concepts. *Selected Topics in Quantum Electronics, IEEE Journal of*, 8(5):1015–1024, Sep/Oct 2002.

[19] Y.H. Chang, P.C. Peng, W.K. Tsai, G. Lin, FangI Lai, R.S. Hsiao, H.P. Yang, H.C. Yu, K.F. Lin, J.Y. Chi, S.C. Wang, and H.C. Kuo. Single-mode monolithic

quantum-dot VCSEL in 1.3 μm with sidemode suppression ratio over 30 dB. *Photonics Technology Letters, IEEE*, 18(7):847–849, 1, 2006.

[20] Frank H. Peters and W.L. Gore and Associates. Vertical Version 1.1 Beta, 1996.

[21] J.W. Scott, B.J. Thibeault, D.B. Young, L.A. Coldren, and F.H. Peters. High efficiency submilliamp vertical cavity lasers with intracavity contacts. *Photonics Technology Letters, IEEE*, 6(6):678–680, Jun 1994.

[22] P. Ressel, H. Strusny, S. Gramlich, U. Zeimer, J. Sebastian, and K. Vogel. Optimised proton implantation step for vertical-cavity surface-emitting lasers. *Electronics Letters*, 29(10):918–919, May 1993.

[23] D. L. Huffaker, D. G. Deppe, K. Kumar, and T. J. Rogers. Native-oxide defined ring contact for low threshold vertical-cavity lasers. *Applied Physics Letters*, 65(1):97–99, 1994.

[24] Xiaodong Huang, Andreas Stintz, Kevin Malloy, Guangtian Liu, Luke Lester, and Julian Cheng. Quantum dot vertical cavity surface emitting laser. US Patent Number 6782021, August 2004.

[25] AZ Electronic Materials. AZ Developer, 400K, and 421K Inorganic Developers, January 2005. `http://www.az-em.com/PDFs/inorganic_developer/az_inorganic_developer.pdf`.

[26] D. L. Miller and P. M. Asbeck. Be redistribution during growth of GaAs and AlGaAs by molecular beam epitaxy. *Journal of Applied Physics*, 57(6):1816–1822, 1985.

[27] Thomas J. Rotter. *Growth and properties of self assembled InAs quantum dash laser active regions*. PhD thesis, The University of New Mexico, July 2007.

Chapter 4

Quantum Dot Vertical-External-Cavity Surface-Emitting Laser

4.1 Introduction

High power lasers emitting in the visible wavelength range are of interest for a number of applications including sources for optical pumping, biomedical uses, and laser projection displays. High output powers are not easily achieved in VCSELs, mostly due to the small lateral dimensions of the device active region, which for single transverse mode operation is typically less than 10 μm. By using an external cavity, the device diameter in a VECSEL can be extend to several hundred microns, while still retaining high beam quality and single-mode operation. This has been successfully implemented for electrically injected devices [1], however problems with current spreading and resistive heating severely hinder device performance. Optically pumped VECSELs on the other hand have been very promising since the first

demonstration [2], resulting in Watt-level output powers with good beam quality.

Most visible wavelengths are not readily accessible in VECSELs, at least not in the native AlAs/GaAs material system which is preferred for the high refractive index contrast in the Bragg reflector and its mature technology. But since the laser cavity of a VECSEL extends into free space, one has the option of adding a nonlinear crystal intra-cavity to allow for efficient frequency-doubling of the laser emission, also called second harmonic generation (SHG). This is routinely used for green [3] and blue [4] VECSELs.

For red emission, there are a number of different approaches: In the GaInP/ AlGaInP/GaAs material system, fundamental emission around 675 nm has been achieved [5]. However, these VECSELs require a short wavelength pump source, typically an Argon ion or frequency-doubled diode pumped solid-state (DPSS) laser, instead of the more affordable and widespread[1] 808 nm diode lasers. It is also not easy to extend this design to shorter wavelength emission due to a lack of suitable direct bandgap barrier materials providing sufficient carrier confinement in the QWs. Alternatively, red light can be generated by frequency-doubling of a 1200–1300 nm VECSEL. Using GaInAs, this range is just out of reach, but by adding a small amount of nitrogen, GaInNAs QW VECSELs have been demonstrated in 2004 [7]. More recently, higher output powers allowed for efficient intra-cavity frequency-doubling resulting in 2.7 W of second harmonic (SH) red emission at a wavelength of 612 nm [8].

InAs QDs are also well suited for this range. In 2008, QD VECSELS operating on an excited state transition at 1040 nm have been reported [9], followed by sub-monolayer QDs with a ground state wavelength of 1034 nm [10]. Later that year, ground state emission at 1210 nm with a CW output power of 300 mW was achieved

[1]The main use of 808 nm high power diode lasers is as pump sources for Nd:YAG DPSS lasers. The wavelength is tailored to a strong absorption line in the material [6].

[11]. To our knowledge, intra-cavity frequency-doubling of a QD VECSEL has not been demonstrated prior to this dissertation.

4.2 VECSEL Design

A typical VECSEL is comprised of a semiconductor gain mirror and an external concave dielectric mirror as shown in Fig. 4.1. The gain mirror consists of the active region on top of a DBR. The designs used in our QD devices are discussed in 4.2.1. The constraints for the external cavity and pump setup, and requirements for the external mirror are examined in 4.2.2.

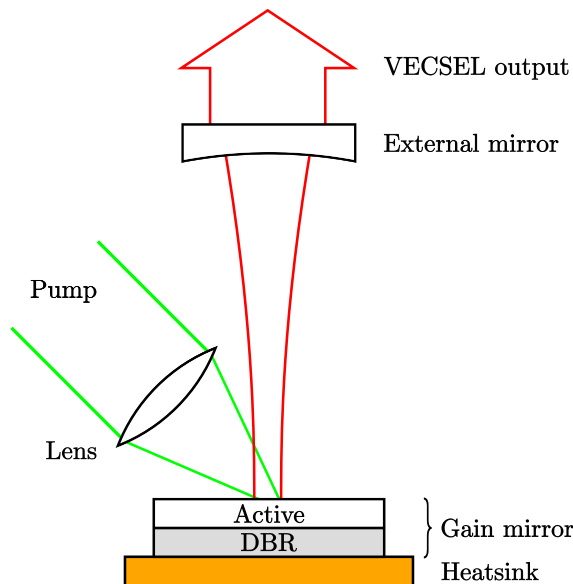

Figure 4.1: Schematic diagram of a VECSEL.

4.2.1 Gain Mirror

The design of a VECSEL gain mirror is essentially identical to that of a VCSEL without the top DBR. The lateral dimension of the device active area is defined by the size of the pump laser spot on the sample and no oxide aperture is needed. Therefore, pure AlAs can be used for the low-index layers of the DBR. In our design, the bottom Bragg reflector consists of 30 pairs of $\lambda/4$ optical thickness alternating layers of GaAs and AlAs.

The optically excited carriers inside the GaAs cavity need to be confined in the vertical direction, to prevent surface recombination at the GaAs-air interface. This is acomplished by an AlGaAs or AlAs layer, which can be integrated in a MBE-grown AR coating [12]. Due to concerns of insufficient gain from the QD active region, an extra DBR pair was grown instead. To prevent the pump laser from being absorbed in the extra layers, $Al_{0.3}Ga_{0.7}As$ was used as the high-index layer and only covered with 5 nm of GaAs to protect it from oxidation. This additional reflector leads to a lower lasing threshold, since $|E|^2$ at the QD layers is higher compared to the AR-coated structure [13]. However, the resulting higher-finesse subcavity might cause problems, due to the narrower resonance: A broad emission spectrum is not only desirable for possible mode-locking of the VECSEL, it also is advantageous for temperature stability. With increasing temperature at high pump powers the gain maximum shifts much faster than the sub-cavity resonance, resulting in lower efficiency.

To improve performance for these applications, the extra DBR pair on top can be removed using selective wet etching, leaving a GaAs-air interface. Furthermore, a dielectric AR coating as in [2] could be employed.

Gain is supplied via 12 DWELL layers, arranged in different ways for the two samples: One utilizes a design analogous to the VCSEL, with four groups of three

closely spaced DWELL layers at each antinode of the standing wave pattern inside the semiconductor. The electrical field, simulated using [14], and index of refraction profile of this structure is shown in Fig. 4.2. The other has a single DWELL layer at each antinode, repeated 12 times. The second design, shown in Fig. 4.3, is usually referred to as a resonant periodic gain (RPG) structure [15]. In both cases, the distance between the groups or single QD layers corresponds to an optical path length of $\lambda/2$, resulting in a total length L of the GaAs subcavity between the the bottom and top DBR of $4\lambda/2$ and $12\lambda/2$, respectively.

As has been calculated in chapter 2, the different active region designs result in different confinement factors and threshold gain values, with a slight advantage for the RPG structure. It also has the lower average In composition throughout the cavity, yielding lower strain and therefore possibly better material quality.

The subcavity length is important for the absorption of the pump light. For a simple approximation, we can calculate the pump intensity I_P at a depth z inside a GaAs layer as

$$I_P(z) = I_{P,0}\ e^{-\alpha z} \tag{4.1}$$

where $I_{P,0}$ is the intensity at the surface and α is the absorption coefficient of GaAs. At our pump wavelength of 808 nm the value is $\alpha = 1.3 \cdot 10^4$ cm^{-1} [16, 17].

For the 4x3 DWELL structure, the GaAs subcavity has a thickness of 0.9 μm, resulting in roughly 70% of the pump light being absorpted in a single pass through the subcavity. The remaining light is mostly absorbed in the bottom DBR, with only a small portion being reflected back into the cavity. In the case of the RPG design, the thickness GaAs thickness is almost 2.4 μm, resulting in about 96% of light being absorbed. This should be advantageous, however it also results in larger nonuniformity of the pump power throughout the subcavity.

It has been suggested [10], that the active layers in a VECSEL can be distributed

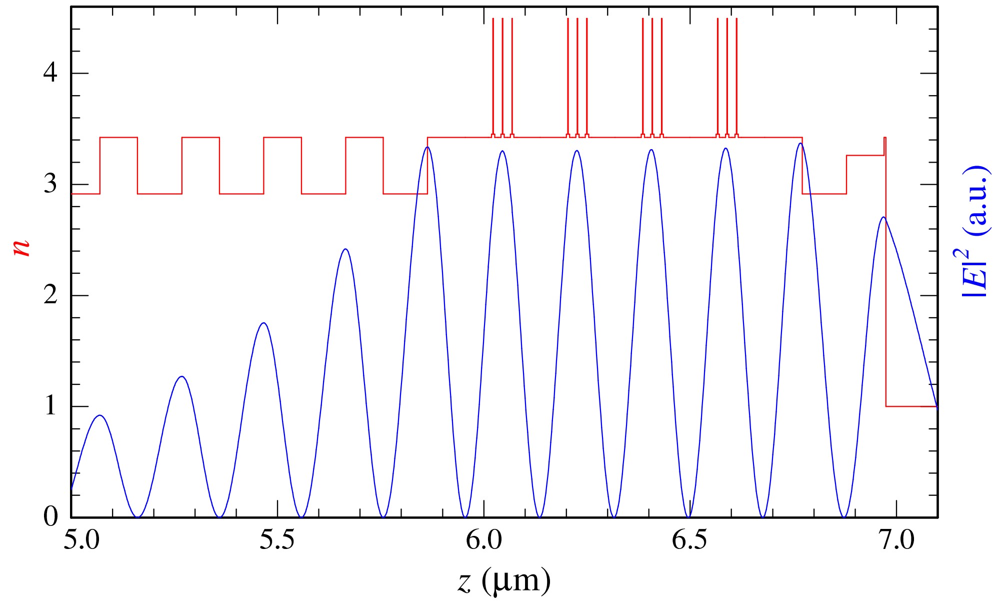

Figure 4.2: Refractive index n and electric field $|E|^2$ of the 4x3 DWELL sample. Note that only four of the 30 bottom DBR pairs are shown.

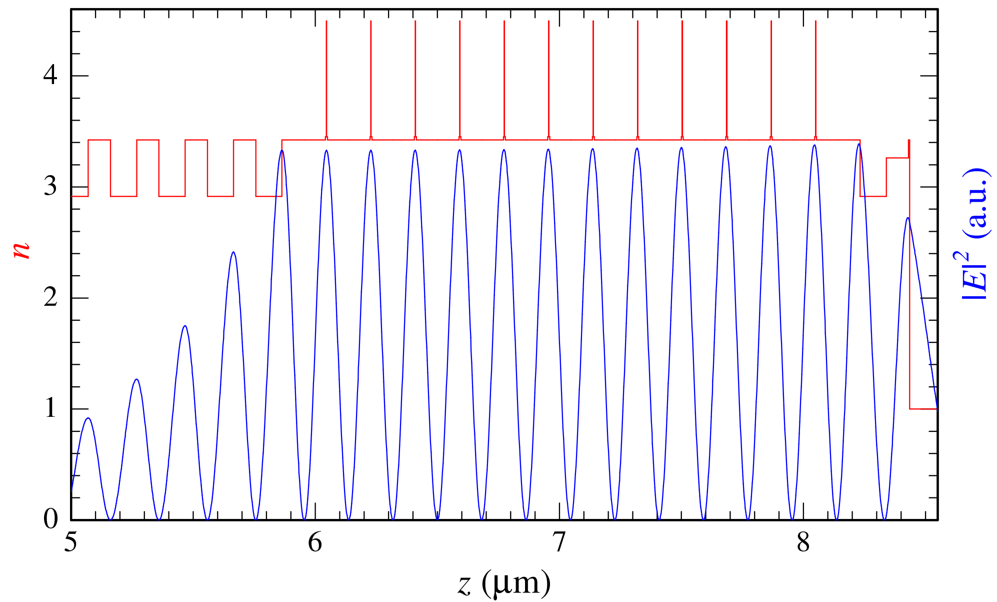

Figure 4.3: Refractive index n and electric field $|E|^2$ of the 12 DWELL RPG sample. Note that only four of the 30 bottom DBR pairs are shown.

in a nonlinear fashion to account for the varying pump intensity. In our device geometry, combined with a maximum of three DWELL layers per standing wave antinode, would allow for only one 3-stack, followed by single QD layers. To keep the total number of DWELL layers unchanged, the remaining single layers would still be spread out too far to allow for uniform carrier distribution, so we decided against this design.

4.2.2 External Cavity

The first aspect to consider when designing the external cavity is its stability. According to [18], we can find the transmission matrix **T** by multiplying the matrices for the propagation over the distance d (see Fig. 4.4) from the gain mirror to the external mirror, the reflection at the external mirror with radius R, and the propagation

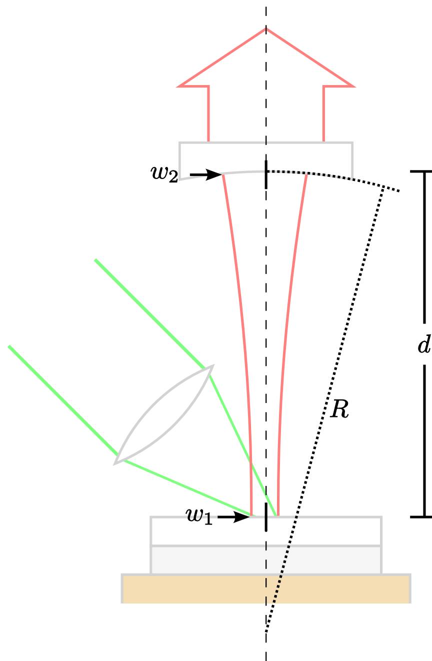

Figure 4.4: Dimensions of the VECSEL cavity.

back to the gain mirror:

$$\mathbf{T} = \begin{bmatrix} 1 & d \\ 0 & 1 \end{bmatrix} \begin{bmatrix} 1 & 0 \\ -\frac{2}{R} & 1 \end{bmatrix} \begin{bmatrix} 1 & d \\ 0 & 1 \end{bmatrix} = \begin{bmatrix} 1-\frac{2d}{R} & 2d-\frac{2d^2}{R} \\ -\frac{2}{R} & 1-\frac{2d}{R} \end{bmatrix} \equiv \begin{bmatrix} A & B \\ C & D \end{bmatrix} \tag{4.2}$$

The cavity is stable, if

$$0 \leq \frac{A+D+2}{4} \leq 1 \tag{4.3}$$

Assuming positive d and R this yields

$$d \leq R \tag{4.4}$$

meaning the cavity length has to be less than or equal to the radius of cuvature of the external mirror.

Next, the beam waist w_1 of the Gaussian mode on the gain mirror can be calculated. This is of importance, because the waist of the focused pump beam needs to be matched to it for best performance. For this calculation, a simplified matrix

$$\mathbf{T} = \begin{bmatrix} 1 & d \\ 0 & 1 \end{bmatrix} \equiv \begin{bmatrix} A & B \\ C & D \end{bmatrix} \tag{4.5}$$

can be used, only taking into account the propagation between the mirrors.

A Gaussian beam can be characterized by the complex beam parameter q, where

$$\frac{1}{q} = \frac{1}{R} - i\frac{\lambda_0}{\pi n w} \tag{4.6}$$

Since in our case the cavity is in free space, $\lambda = \lambda_0$ and $n = 1$ will be used. The ABCD law relates the beam parameters at two planes 1 and 2:

$$\frac{1}{q_2} = \frac{C + D(1/q_1)}{A + B(1/q_1)} \tag{4.7}$$

Using $R_1 = \infty$ for the flat gain mirror, $R_2 = R$ for the external mirror, and Eq. 4.5 we can solve for the beam waist on the gain mirror:

$$w_1 = \sqrt[4]{\frac{Rd\lambda^2 - d^2\lambda^2}{\pi^2}} \tag{4.8}$$

Experiments were carried out using either a Ti:sapphire laser or a fiber-coupled high power diode laser as pump source. In the first case, the power is limited to less than 1.5 W. Therefore, only a small spot size can be pumped in order to reach lasing threshold. For those experiments, a mirror with $R = 25$ mm was used. The beam waist as a function of cavity length as calculated by Eq. 4.8 is shown in Fig. 4.5. Typical cavity lengths are $0.8R \lesssim d < R$, as in shorter cavities the pump beam would have to be at too large an angle from the sample surface normal as to not be obstructed by the external mirror. Under these conditions, the beam waist is around 30–60 μm. The Ti:sapphire pump beam can easily be focused to similar dimensions with a simple lens.

In the case of the fiber-coupled diode laser, a very tight focus is hard to achieve, because of the larger fiber core diameter of 400 μm. Due to space restraints, this can only be imaged slightly smaller than 1:1, resulting in a beam waist close to 200 μm. This requires the use of an external mirror with larger radius of curvature, in our case $R = 250$ mm. The calculated beam waist is shown in Fig. 4.6, with typical values of 100–200 μm for this case.

The mirror selected for the Ti:Sapphire pump experiments ($R = 25$ mm) has a reflectance of 99.5%. Due to the extremely short cavity length (< 25 mm), a half-inch diameter mirror was chosen to allow easier access for the pump beam. The reflectance spectra is shown in Fig. 4.7. For the $R = 250$ mm external mirrors, obstruction of the pump beam path is not an issue, so one inch diameter optics were chosen to allow for easier alignment. Reflectance values of 99.5% and 99.0% (see Fig. 4.7) allow for a variation of the mirror loss of the cavity. For high output power, the lower reflectivity is prefered, while the lower loss/higher reflectivity mirror reduces threshold and increases intra-cavity power, which is advantages for frequency-doubling experiments.

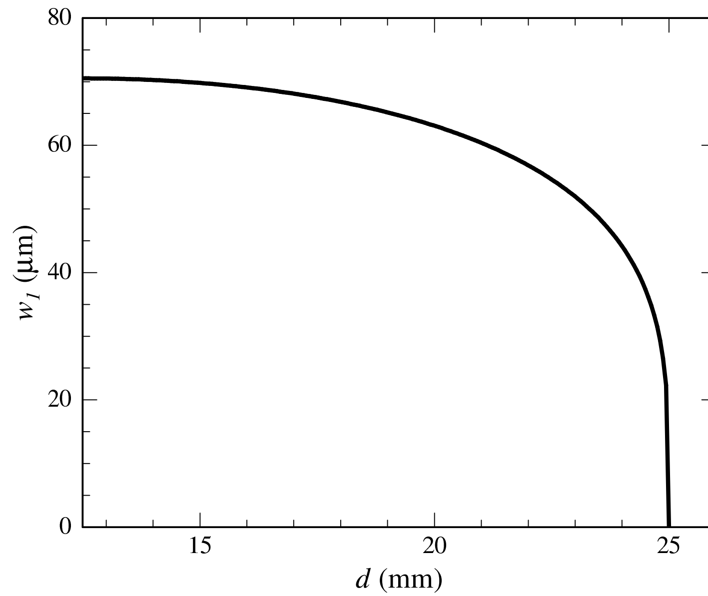

Figure 4.5: Calculated beam waist w_1 as function of cavity length d for a $R = 25$ mm external mirror and a wavelength of $\lambda = 1250$ mm.

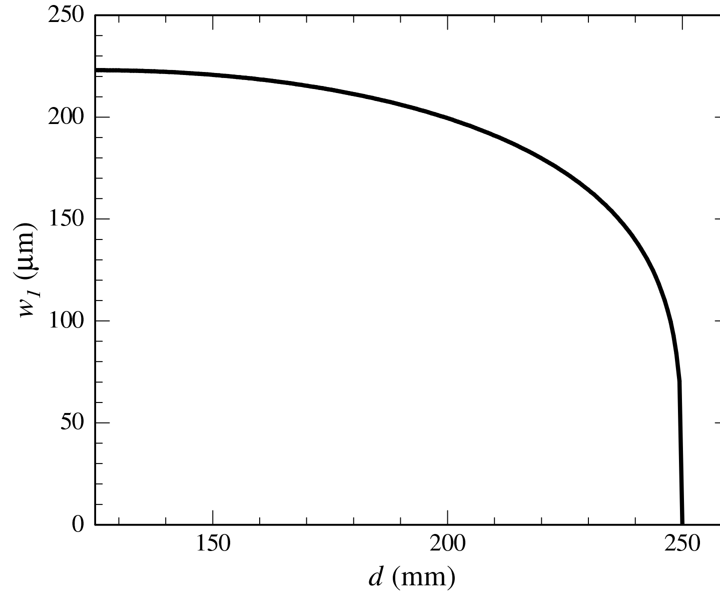

Figure 4.6: Calculated beam waist w_1 as function of cavity length d for a $R = 250$ mm external mirror and a wavelength of $\lambda = 1250$ mm.

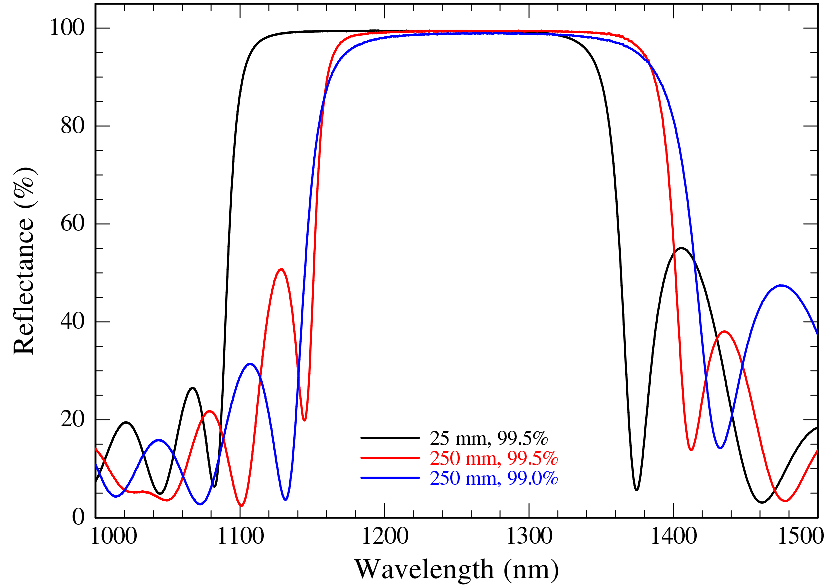

Figure 4.7: Reflectance spectra for the external mirrors/output couplers used in VECSEL experiments.

4.3 Experimental Results

4.3.1 Optical Wafer Characterization

Before setting up the external cavity and pump laser, a few preliminary tests can be performed, to verify the properties of the VECSEL wafers. Reflectance spectra, collected using a near-normal incidence reflectivity setup and white-light source in the FTIR spectrometer allow for a fast comparison with the calculated spectra [14]. Fig. 4.8 shows both spectra for the 4x3 DWELL VECSEL sample, with the simulation being designed for a wavelength of 1260 nm.

The sample can also be characterized using room temperature PL with low power Helium-Neon laser excitation. However, the observed spectrum is the result of the QD emission being filtered by the reflectance and cavity resonance. This is quite obvious when overlaying the PL data onto the reflectance spectra as in Fig. 4.8.

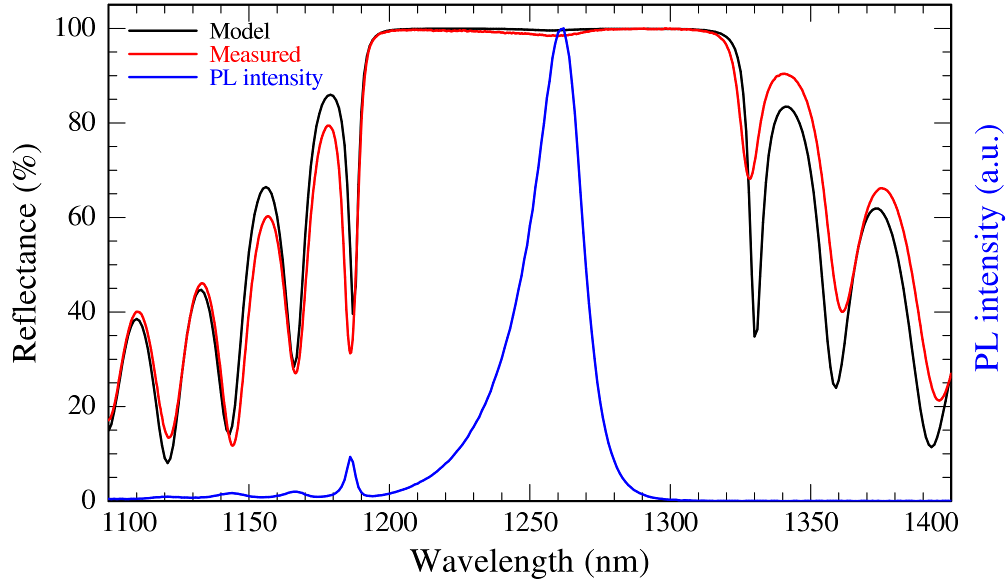

Figure 4.8: Comparison between calculated and measured reflectance spectra as well as PL spectrum measured at room temperature and low excitation power for 4x3 DWELL VECSEL.

Therefore, the peak in the PL signal might not actually correspond to the maximum of the QD spontaneous emission spectrum, but rather the subcavity resonance. It is possible to reduce this effect by etching off the extra DBR pair on top, applying a simple AR coating to the sample, or measuring the emission from the side. But some of the influence of the cavity remains, hindering a straightforward interpretation of results. For this reason, no extensive characterization of the PL emission of the VECSEL samples has been carried out. Fortunately, we know from past experience [19] characterizing QD samples grown on the same MBE reactor without DBRs or cavities that the emission wavelength is very uniform across the wafer, so this is not of major concern.

The layer thickness and hence the DBR wavelength and subcavity resonance on the other hand changes significantly across the wafer. It is very useful to have this variation in a sample, as a variety of different gain peak to cavity mode alignments

can be tested in the same device. For an even larger range of wavelength, the two VECSEL samples investigated were MBE-grown on three inch diameter substrates. The resulting wafers are radially symmetric with the thickest layers (longest wavelength) at the center, tapering off towards the outside. FTIR-measured reflectance spectra for various positions on the sample are shown in Fig. 4.9. The indicated position as function of the distance from the center of the wafer refers to the middle of the approximately 4 mm wide measurement area.

4.3.2 Output Power Characteristics

Initial experiments were conducted using a Ti:Sapphire laser as the pump source. Output powers of up to 1.4 W were achieved with the emission wavelength tuned to 800 nm in CW operation (limited by the poor mode quality of the aging Ar-ion pump laser).

The Ti:Sapphire pump beam was directed onto the QD sample under an angle of approximately 25° to the semiconductor surface normal and was focused by a lens with a focal length of 10 cm. The VECSEL gain mirror was mounted to a TE-cooled copper plate using silicone-based heat sink compound. The cavity was completed with the $R = 25$ mm radius of curvature external mirror at a distance of 24 mm.

The position and angle of the output coupler was aligned by maximizing the emission power, which was also utilized to adjust the focus of the pump beam to match the spot size to the beam waist of the cavity mode. Pump power was adjusted using a variable ND filter and measured using a thermopile detector. The VECSEL output was directed onto a photodiode for low power measurements, or a thermopile detector for higher powers.

Output power vs. pump power was measured for heatsink temperatures of 0°C and 20°C and was plotted in Fig. 4.10 for the 4x3 DWELL VECSEL and Fig. 4.11

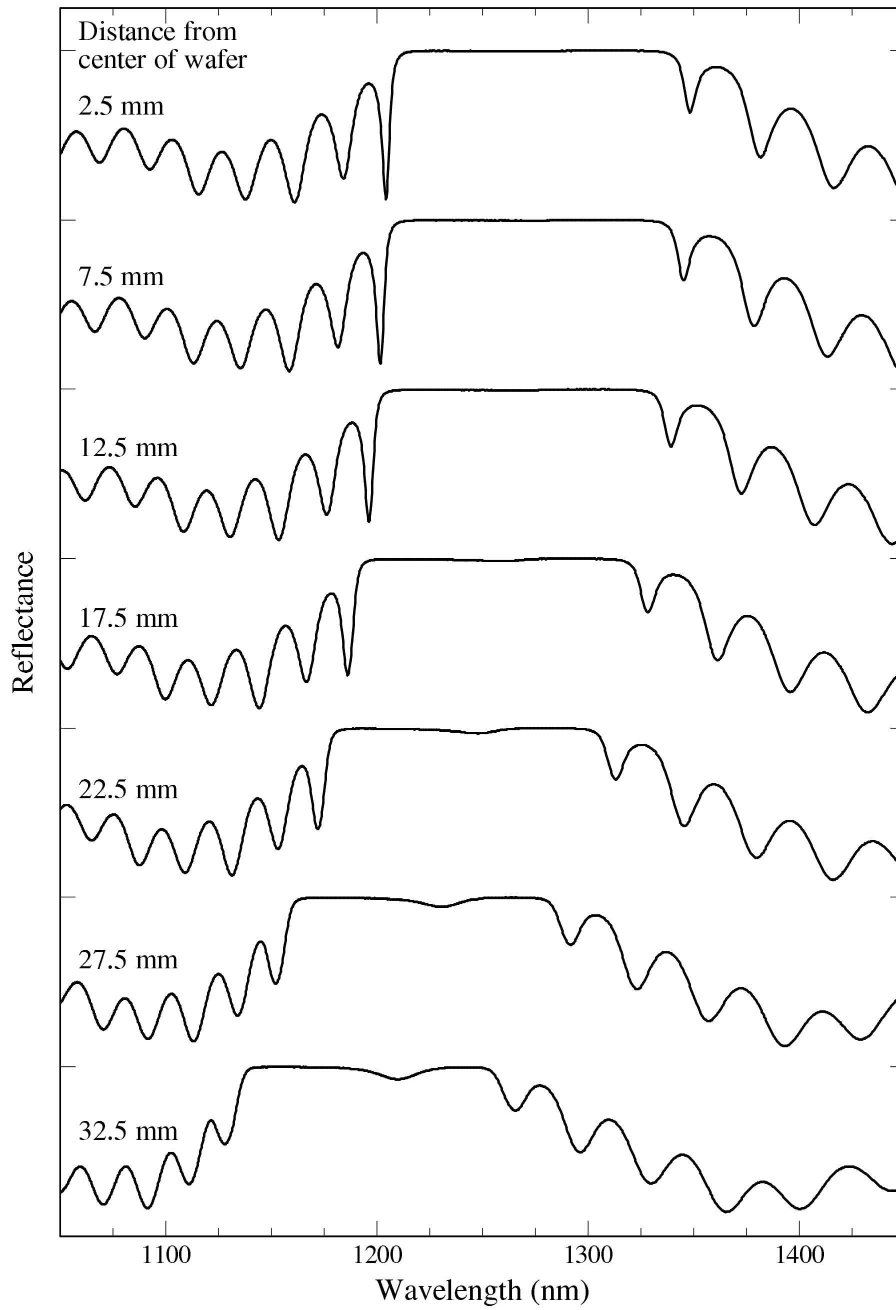

Figure 4.9: FTIR reflectance spectra as function of the position on the 4x3 DWELL VECSEL wafer.

for the RPG structure, respectively. The straight lines overlaid onto the data points are linear fits to indicate the area used to determine the differential optical-to-optical efficiency (slope efficiency); not shown in the plots are linear fits at low output power levels used to extrpolate the threshold pump powers.

The output power in these experiments was mainly limited by the available power from the Ti:Sapphire pump laser, only at 20°C signs of thermal roll-over were visible. For higher power experiments, a 808 nm fiber coupled diode laser with a maximum CW power of 45 W was used. The output coupler was replaced with a 250 mm radius of curvature optic, with nominally identical reflectance of 99.5%. The ouput from the 400 μm core diameter fiber was collimated by a 50 mm focal length lens and then focused onto the gain mirror by a 35 mm focal length lens. This should result in a roughly 150 μm spot size, ideal for the beam waist of the 250 mm external mirror at a distance of 240 mm. The shorter distance from the focussing lens to the sample also required an increase in the pump angle to about 40°, which did not result in any obvious negative effects on the VECSEL's operation.

With this new setup, output power vs. pump power curves were again measured for both gain structures and are shown in Figs. 4.12 and 4.13. Differential efficiencies and threshold powers were evaluated in the same way as before.

Since both VECSELs easily reached lasing threshold and operated over a wide range of pump powers above threshold, the 99.5% reflecting output coupler was replaced with the lower reflectance (99.0%)/higher transmission one of identical radius of curvature. The VECSEL cavity alignment was once again optimized for maximum output power, and pump vs. output power curves at 20°C and 0°C were recorded and analyzed for both gain mirror samples. The resulting plots are shown in Figs. 4.14 and 4.15.

The data extracted from the different plots is collected in Tab. 4.1. Due to the

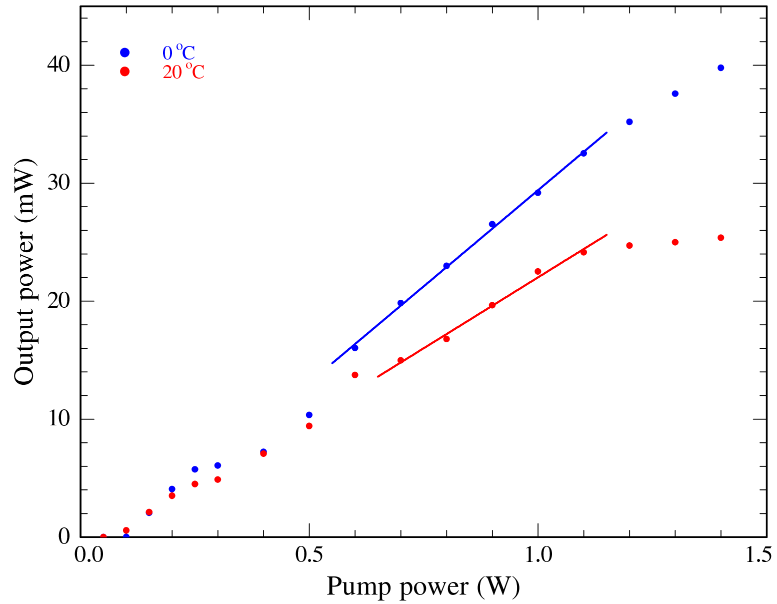

Figure 4.10: VECSEL output power vs. pump power for Ti:Sapphire pumped operation for the 4x3 DWELL sample.

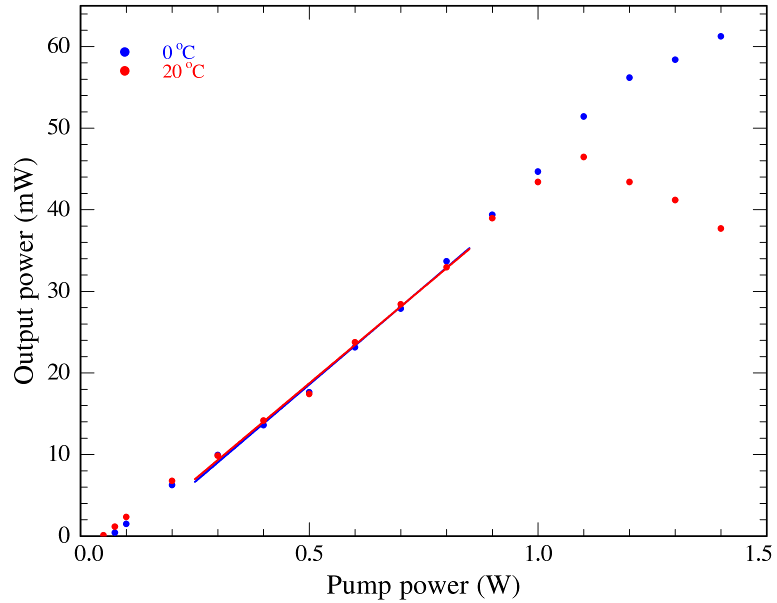

Figure 4.11: VECSEL output power vs. pump power for Ti:Sapphire pumped operation for the RPG sample.

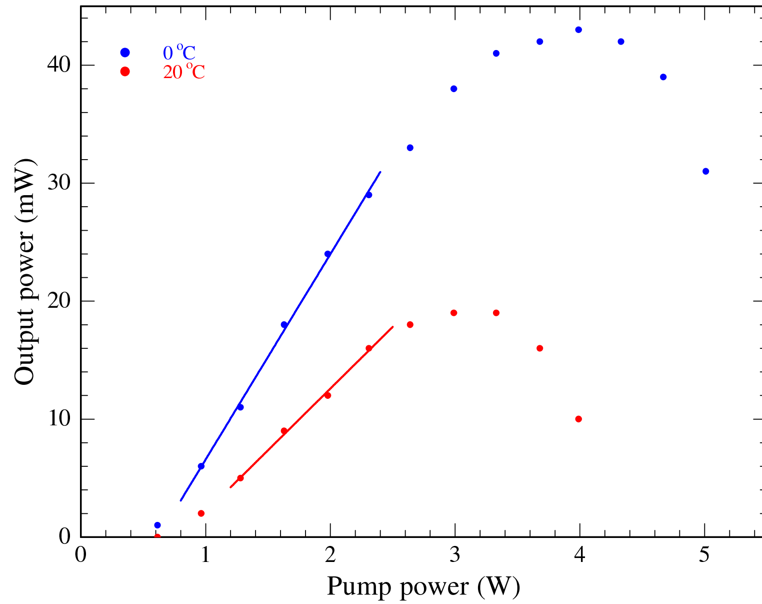

Figure 4.12: VECSEL output power vs. pump power for diode-pumped operation for the 4x3 DWELL sample and 99.5% external mirror.

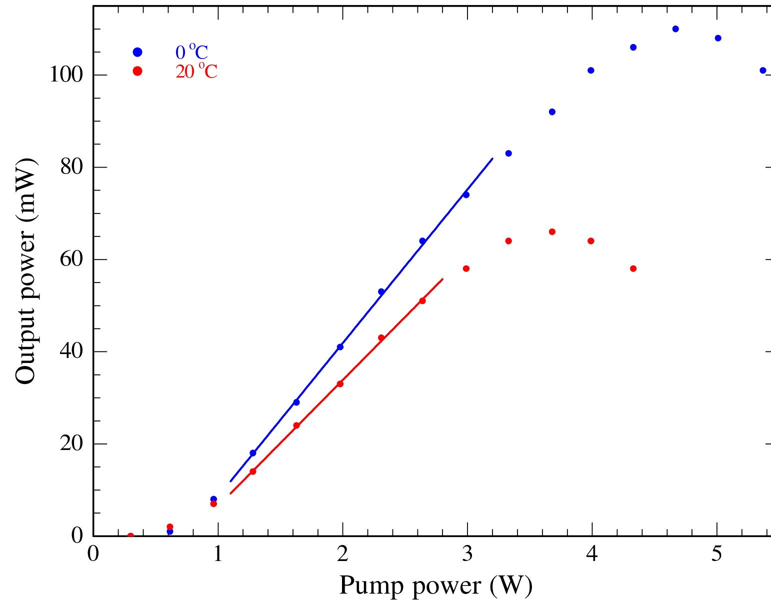

Figure 4.13: VECSEL output power vs. pump power for diode-pumped operation for the RPG sample and 99.5% external mirror.

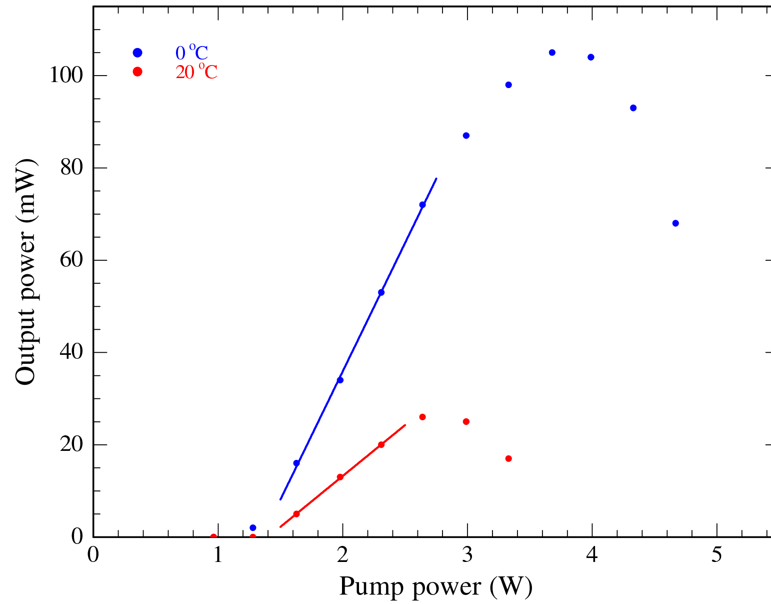

Figure 4.14: VECSEL output power vs. pump power for diode-pumped operation for the 4x3 DWELL sample and 99.0% external mirror.

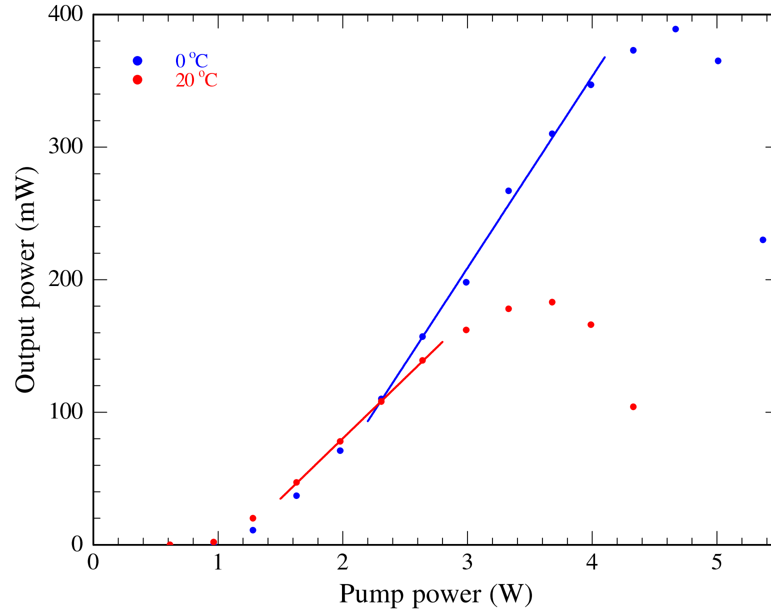

Figure 4.15: VECSEL output power vs. pump power for diode-pumped operation for the RPG sample and 99.0% external mirror.

Gain mirror	4x3 DWELL			12 DWELL RPG		
Pump laser	Ti:Sapphire	808 nm diode		Ti:Sapphire	808 nm diode	
Beam waist (μm)	50	150		50	150	
Reflectance (%)	99.5	99.5	99.0	99.5	99.5	99.0
Threshold power	0.10	0.55	1.23	0.07	0.57	1.13
(W)	0.08	0.62	1.28	0.05	0.48	1.02
Threshold power	1.27	0.77	1.74	0.85	0.80	1.60
density (kWcm^{-2})	1.02	0.87	1.81	0.62	0.67	1.44
Slope efficiency	3.3	1.7	5.6	4.7	3.3	14.4
(%)	2.4	1.1	2.2	4.5	2.7	9.1
Maximum output	40[a]	43	105	61[a]	110	389
power (mW)	25[a]	19	26	46	66	183

[a]Limited by available pump power from the Ti:Sapphire laser.

Table 4.1: Summary of VECSEL lasing parameters extracted from Figs. 4.10–4.15. Values for a heat sink temperature of 0°C are shown in blue, for 20°C in red.

different pump spot sizes, the threshold power varies significantly for the different experiments. To facilitate the comparison of results, the threshold power density

$$P_{th} = \frac{\text{Threshold power}}{\text{Mode area}} \tag{4.9}$$

is introduced[2], analogous to the threshold current density in electrically injected devices.

Values for P_{th} using a 99.5% external mirror are on the order of 0.8 kWcm^{-2} for both gain structures, when using the 808 nm diode pump. A similar number is found for the RPG structure using the Ti:Sapphire laser. Only the 4x3 DWELL sample exhibits slightly larger values. The lowest reported threshold power density for a QD VECSEL is 2 kWcm^{-2} using a 99.8% mirror [11]. Our threshold is less

[2]Power divided by area is usually referred to as "intensity"; in VECSEL literature, however, the term "threshold power density" is used almost exclusively.

than half, despite the higher mirror loss in the cavity. Even for the case of the 99.0% reflective output coupler the threshold power density only rises to 1.8 kWcm^{-2}. The comparison to the lowest published threshold of a GaInNAs VECSEL of 5 kWcm^{-2} using a 99.0% external mirror [20] is also very favorable for our QD lasers.

To allow for a comparison of the threshold power densities with the results from our QD VCSELs (chapter 3), we can calculate the current corresponding to the rate at which carriers are excited in the sample by the pump laser. The total Energy provided by a laser beam of optical power P is

$$P = \frac{dN}{dt} h \frac{c}{\lambda} \tag{4.10}$$

where dN/dt is the flux of photons of wavelength λ, h is Planck's constant, and c is the speed of light. Ignoring any reflected or transmitted pump light and assuming every incident photon creates an electron-hole pair in the sample, this corresponds to a current

$$I = \frac{dN}{dt} e \tag{4.11}$$

where e is the electron charge. Using equation 4.10 we get

$$I = \frac{Pe\lambda}{hc} \tag{4.12}$$

Pump power densities of 0.8 kWcm^{-2} therefore correspond to a current density of 0.5 kAcm^{-2} under those idealized assumptions, comparable to the values in our large VCSEL devices. With higher mirror loss the value increases to about 1 kAcm^{-2}.

While threshold data are quite consistent between the samples, the values for differential efficiency and maximum output power differ significantly. Comparing the Ti:Sapphire pumped experiments, the RPG sample shows considerably higher output powers and slope efficiencies. When switching to the diode pump laser, the 4x3 DWELL structure falls even more behind, with differential efficiencies about half

the previous value, resulting in the same output power as in the previous experiment, despite larger area and high pump power. The RPG structure exhibits decreased efficiency as well, but the maximum output power is still roughly doubled.

As expected, the switch to the 99.0% external mirror increases differential efficiencies and output powers for both samples (at the expense of threshold power density), with the 4x3 DWELL VECSEL now emitting over 100 mW at 0°C, and the RPG structure close to 400 mW. The slope efficiencies are 5.6% and 14.4%, respectively. The large increase in performance when changing the output coupler suggests that the use of a lower reflectance mirror, e.g. 98%, might show further improvement.

It should also be noted that an increase of the heatsink temperature to 20°C has a much more detrimental effect on the 4x3 DWELL sample. While the difference between the two samples in the Ti:Sapphire experiments might be explained by the lower pump absorption in the thinner cavity of the 4x3 DWELL device, its significantly lower performance in the diode-pumped configuration might suggest another possible explanation: The higher incident pump powers associated with the 808 nm pump laser produce more heat in the gain mirror. Heat is removed through the substrate and bottom DBR, with the latter having the lowest thermal conductivity. It is therefore plausible, that the GaAs cavity of VECSEL structure acts as a heat spreader, laterally removing the heat from the pump spot. Since the 4x3 DWELL sample has a significantly thinner cavity (0.9 μm compared to 2.4 μm for the RPG structure), its performance might be impaired by the more localized heating.

Both samples would certainly profit from the use of more advanced heat sinking techniques, like substrate removal or the use of a transparent intra-cavity heat spreader like SiC or diamond.

4.3.3 Spectral Properties

In the experimental setup, the detector measuring the VECSEL output power can be removed and the emission can be focused into a multimode optical fiber to collect a lasing spectrum using a fiber-coupled optical spectrum analyzer. Spectra for the RPG structure at 0°C using the 99.0% external mirror are shown in Fig. 4.16 for different incident pump power levels above threshold. Two properties are obvious from this plot: The spectra broaden for higher pump powers, and they shift towards longer wavelength.

Even with the VECSEL operating in a single transverse mode, the 240 mm long cavity supports a very large number of closely spaced longitudinal modes. The QD gain peak is very broad as well, due to the size distribution of the dots. The bottom DBR and external mirror have reflectivity maxima over 100 nm and close to 200 nm wide, respectively. The only wavelength selective part of the setup is the subcavity formed by the semiconductor-air interface (or extra DBR pair) on top of the gain mirror. However, this resonance is still very wide when compared to a VCSEL, so that even the broad emission at higher pump powers is easily supported.

The evolution of the spectra with pump power, starting with a very narrow emission just above threshold, and then broadening as the pump power increases might be explained as follows: At threshold, only the lowest loss mode will have enough gain to support lasing. As the power increases, all QDs of the correct size/wavelength provide gain in that mode, until the carrier transport to and capture in the dots [21] limits a further increase in output power. But since not only QDs in that particular mode are supplied carriers faster at higher pump levels, more wavelengths reach threshold and participate in the lasing action.

The resulting broad emission could be advantageous in various applications, especially for the construction of mode-locked lasers for short pulse generation. Even

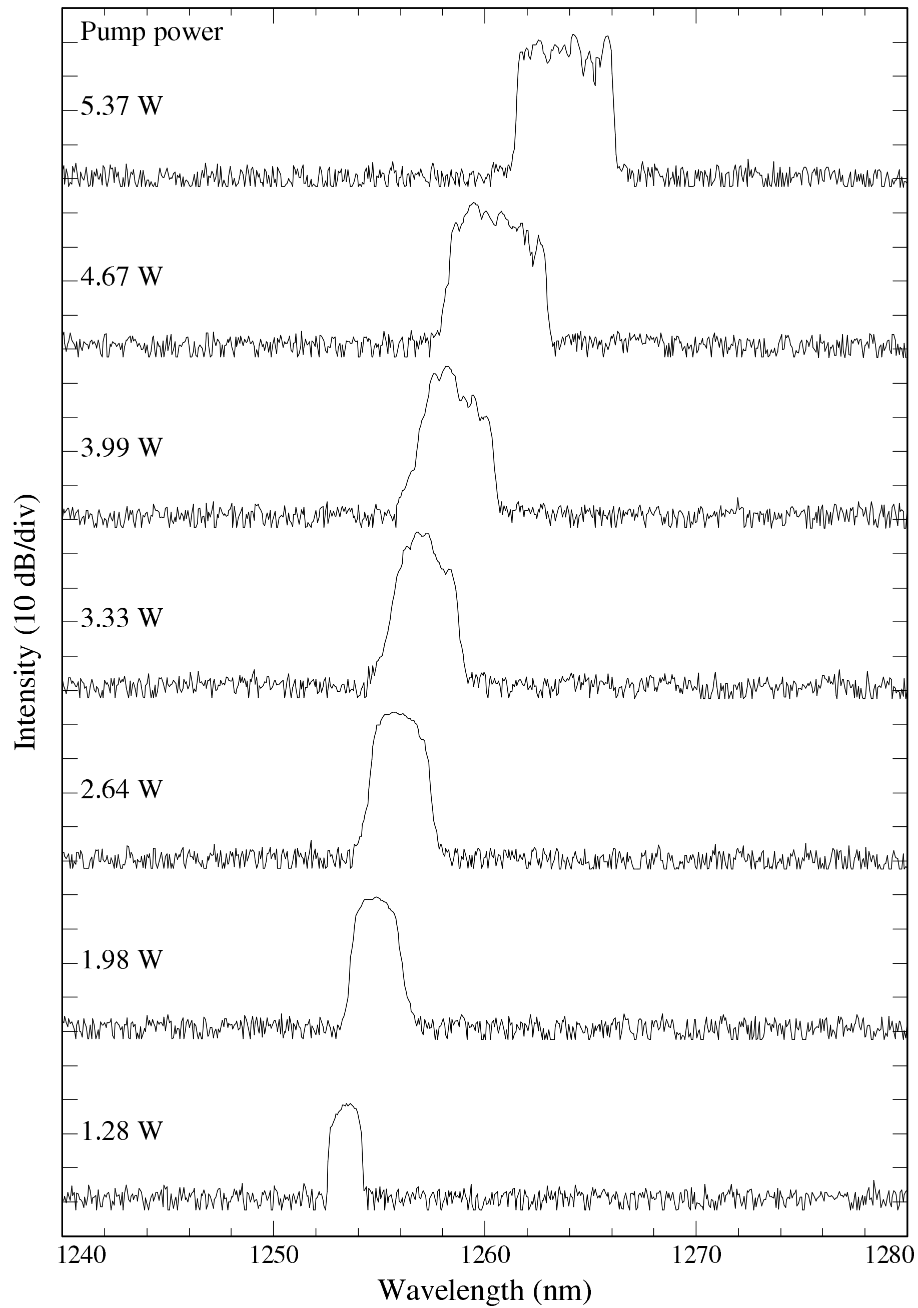

Figure 4.16: Lasing spectra for the RPG structure at 0°C, using the 99.0% external mirror, for different pump power levels.

where the application does not require a broad spectrum, but rather a high output power, the QD VECSEL design provides for very simple power scaling with excellent beam quality. In the case of edge-emitting broad area lasers, power scaling often involves much more intricate techniques, such as spectral beam combining [22].

If on the other hand the application requires a narrow-band and/or tunable emission, it is possible to add a wavelength selective element inside the VECSEL cavity, such as a Fabry-Prot etalon or birefringent filter.

The redshift of the lasing spectrum with higher pump power observed in the VECSEL experiments likely results from increased device heating by the pump beam. Temperature affects not only the bandgap of the gain material, but also the refractive index of the material. For GaAs, which makes up most of the VECSEL structure, the index changes at a rate of approximately $0.07\ \mathrm{nmK}^{-1}$. In addition, thermal expansion might also shift the wavelength of the subcavity resonance in the gain mirror. The linear thermal expansion coefficient for GaAs around room temperature is $6.4 \cdot 10^{-6}\ \mathrm{K}^{-1}$ [23], resulting in a shift of the cavity resonance of an additional $0.01\ \mathrm{nmK}^{-1}$. The shift in the QD emission due to bandgap narrowing was measured in chapter 2 and found to be around $0.4\ \mathrm{nmK}^{-1}$.

The 10 nm redshift observed in our device would correspond to a temperature change of 25°C, when explained by this effect. Thermal expansion and refractive index change on the other hand would require a much larger temperature change which is unrealistic, since it would not only shift the gain peak well away from the resonance, but also reduce the amount of gain available too much to allow lasing. Once again, due to the very broad resonance of the subcavity, it seems quite plausible that the gain peak merely shifts within the constraints of the cavity mode.

4.3.4 Lasing Mode

As expected, the output beam of the QD VECSEL showed a perfectly circular, low divergence beam profile, consistent with a single-mode Gaussian beam. This has been verified by measuring the intensity of the output as a function of position in two dimensions with a CCD array. The resulting mode image, as well as horizontal and vertical line plots through the center of the image are shown in Fig. 4.17. The solid lines are Gaussian fits to the data points.

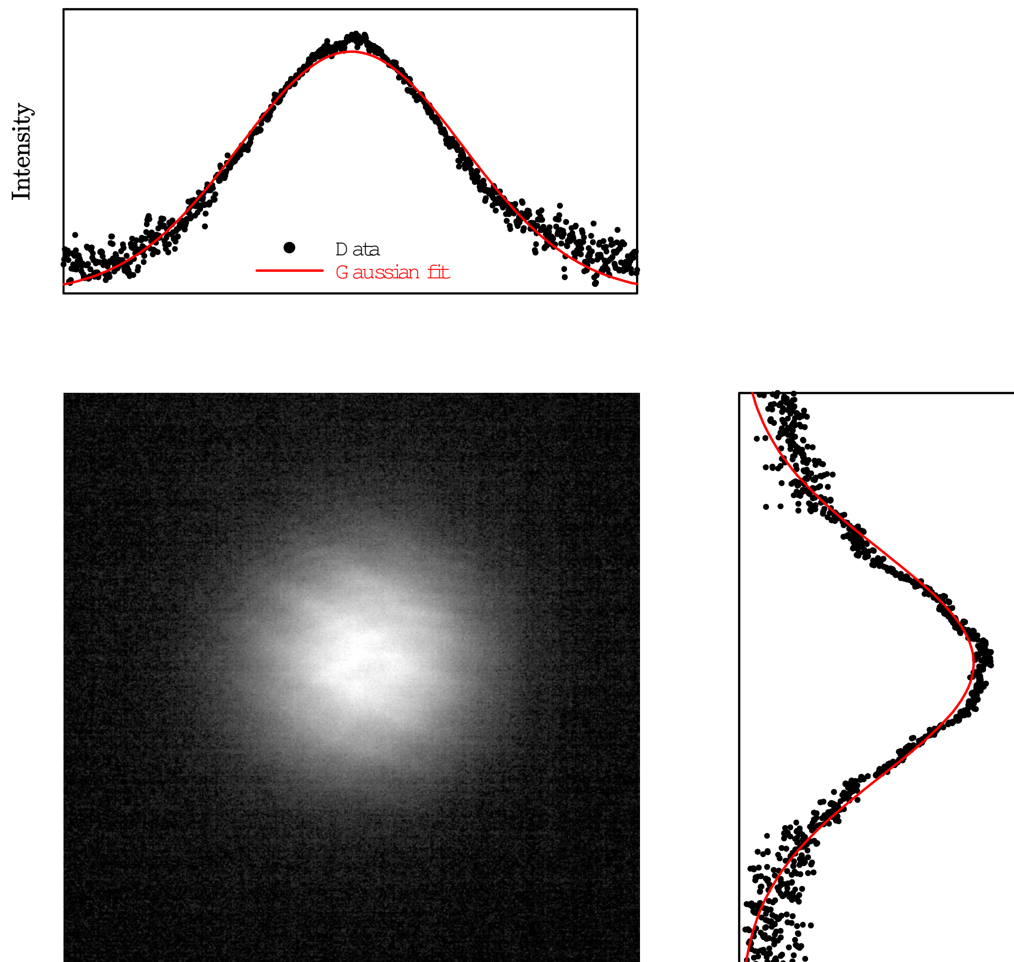

Figure 4.17: Photographs of the fundamental VECSEL lasing mode. The plots are cross-sections through the intensity maximum with Gaussian fits.

In the 808 nm diode-pumped experiments, the larger pump angle from the surface normal sometimes resulted in a single higher-order mode to be preferred over the circular lowest-order mode, which in those cases delivered slightly lower output power.

Typically, the lasing mode was a function of the pump beam and output coupler alignment with respect to the gain mirror, and not affected by any change in pump power.

If the alignment was adjusted away from the optimum position, several different higher-order Hermite-Gaussian lasing modes, or combinations thereof, could be realized in the external cavity. A few random example images of higher-order VECSEL modes obtained in this manner are shown in Fig. 4.18.

4.3.5 Polarization

The VECSEL output was analyzed using a film polarizer in front of the power meter. Output power versus pump power curves were recorded with the polarizer adjusted to block as much of the output as possible, and perpendicular to that. Both curves are plotted in Fig. 4.19, note the different y-axis scaling. The high output powers correspond to a polarization along the [110] crystal direction of the GaAs substrate, and are about a factor of 100 higher than the powers for perpendicular polarization. These observations are in agreement with the results from our VCSELs (see chapter 3), as well as with the preferential polarization previously observed in InAs QDs outside of laser structures [24].

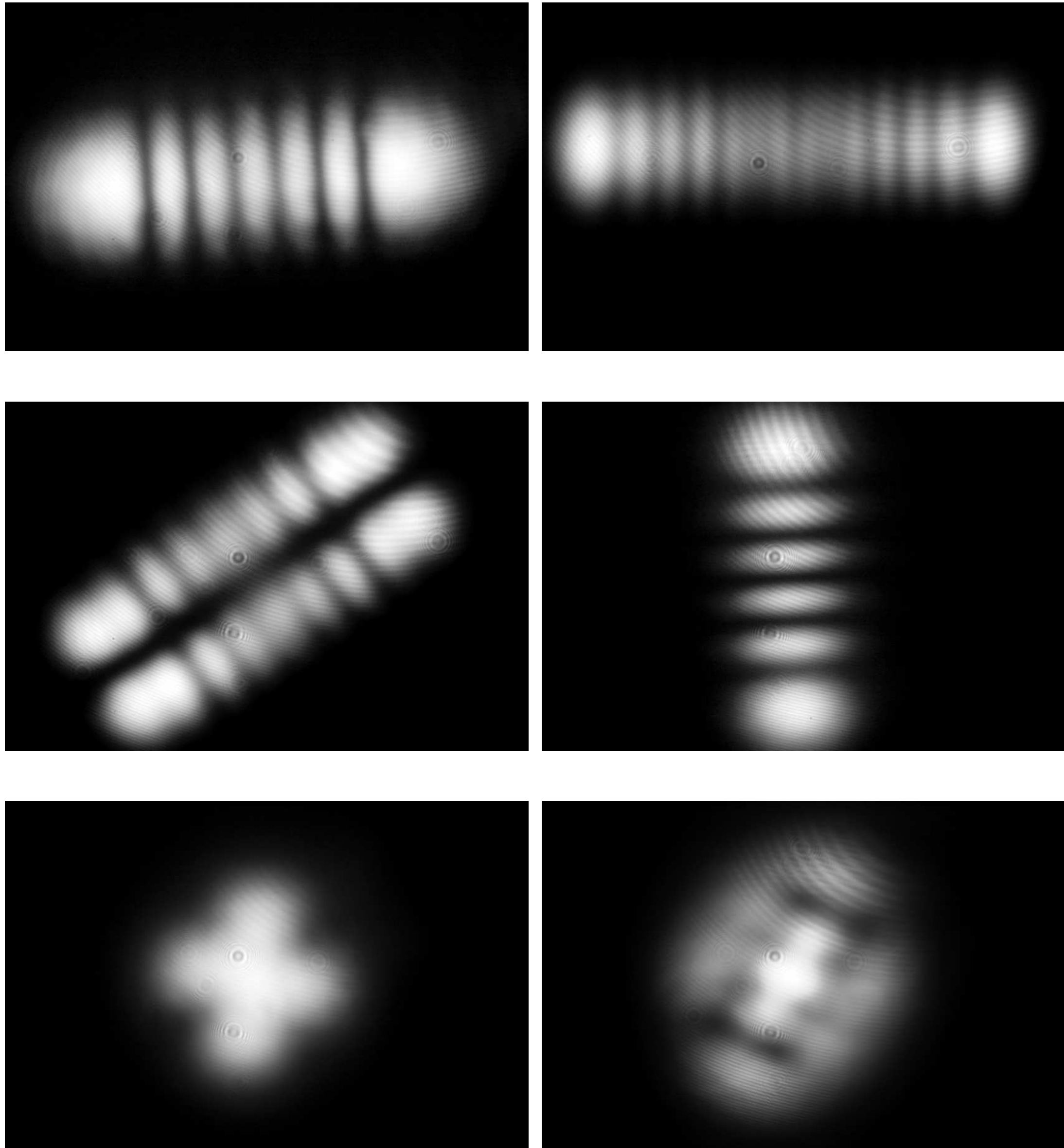

Figure 4.18: Photographs of higher order VECSEL lasing modes created by slightly adjusting pump spot or external mirror location.

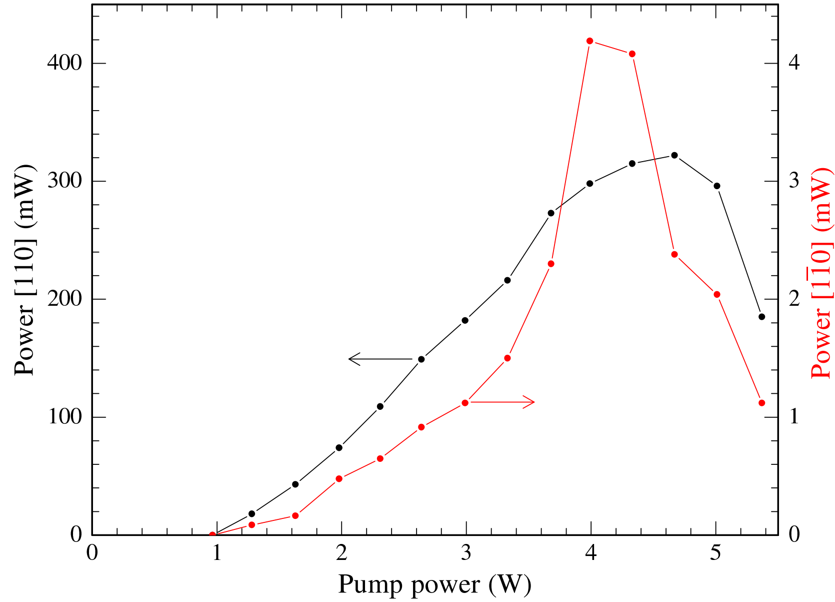

Figure 4.19: VECSEL output power vs. pump power for [110] and [1$\bar{1}$0] polarization direction, showing a roughly 100:1 ratio.

4.3.6 Temperature Dependent Properties

While the presence of the pump laser alone locally changes the sample temperature, the dependence of VECSEL performance on heatsink temperature are of great interest for practical applications. Since the gain mirror is mounted to a copper block attached to a TE cooler, the heatsink temperature can easily be controlled. Experiments were conducted in 10°C steps from 0°C upwards. Output power vs. pump power curves at the different temperatures for the 4x3 DWELL VECSEL are shown in Fig. 4.20, for the RPG structure in 4.21.

The most obvious observation is once again the higher temperature sensitivity of the 4x3 DWELL sample's performance, which did not reach lasing threshold for heat sink temperatures higher than 30°C, whereas the RPG VECSEL was still able to operate at 50°C. For a more detailed analysis of the results, linear fits (not included in plots to preserve clarity) were performed for each curve to determine differential

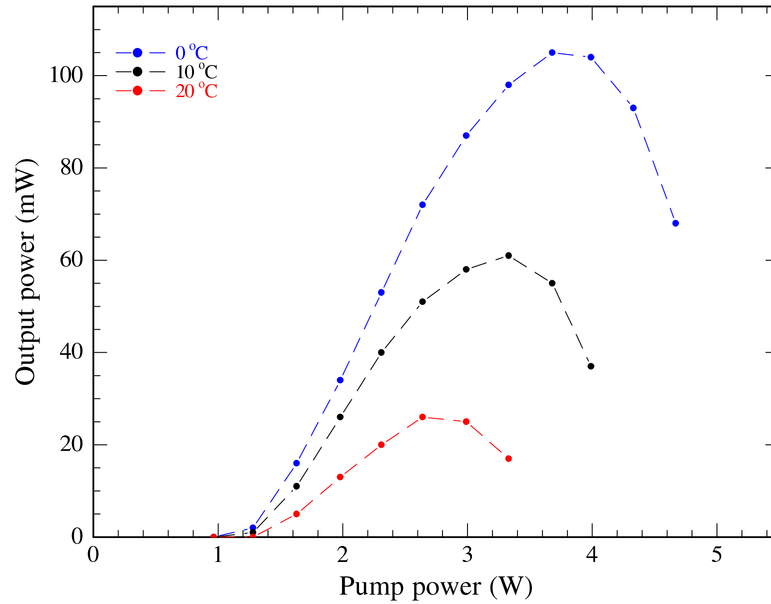

Figure 4.20: VECSEL output power vs. pump power for the 4x3 DWELL sample and 99.0% external mirror at different temperatures.

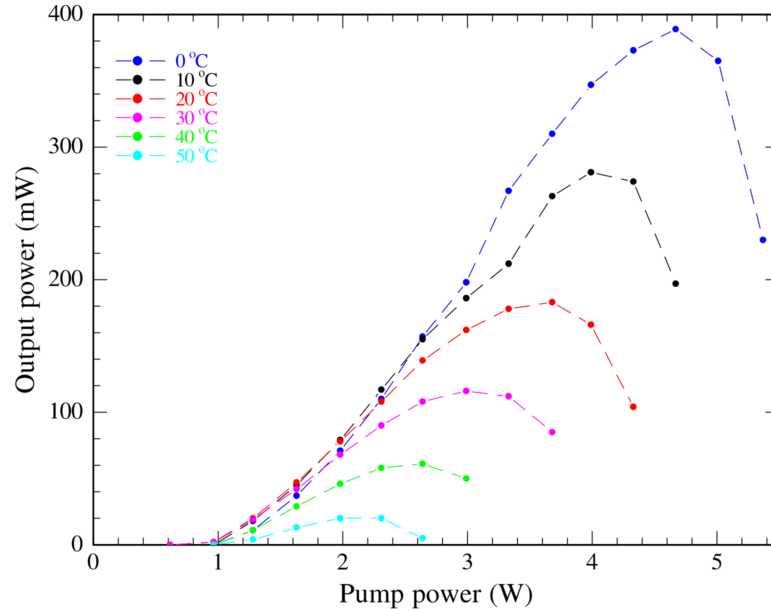

Figure 4.21: VECSEL output power vs. pump power for the RPG sample and 99.0% external mirror at different temperatures.

efficiency and threshold pump power.

Fig. 4.22 shows the threshold pump power density as a function of temperature for the two samples. As has been noted earlier, the threshold is slightly higher for the 4x3 DWELL sample compared to the RPG structure. Although there is only a relatively small change with temperature, the different trend for the two structures is curious. For the 4x3 DWELL VECSEL the threshold increases slightly with temperature, as would be expected if gain decreases with higher temperatures [25].

The 12 DWELL RPG structure on the other hand exhibits a steady decline in threshold power density with increasing temperature. The most likely cause for this is the alignment between gain peak and subcavity mode: At low temperature, the peak wavelength is shorter than the cavity resonance. Once the sample heats up, either from increased pump power or by changing the heatsink temperature, the two shift into alignment. This is consistent with the sample location, which was chosen for high output power at high pump power, i.e. high temperature of the QDs. Similar conditions should exist on the 4x3 DWELL wafer as well, but could not be found. Likely the decreased thermal conductivity — and therefore higher gain

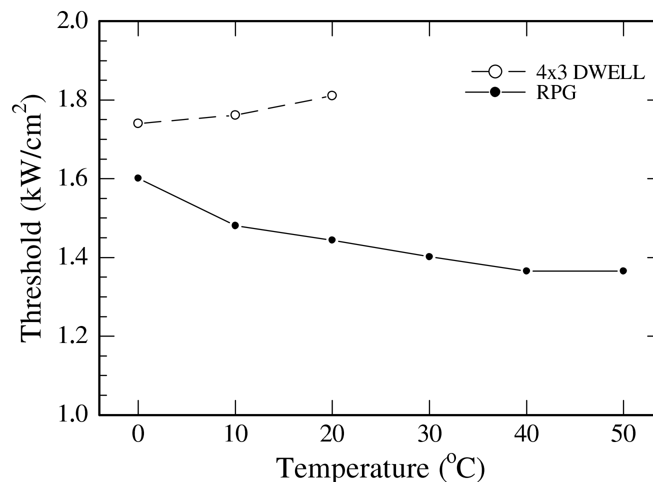

Figure 4.22: VECSEL threshold power density at different temperatures.

medium temperature — in the thinner 4x3 DWELL cavity offsets any advantage due to better alignment.

The differential efficiency is plotted in Fig. 4.23. Both structures show a significant decline with increasing temperature. As observed before, the RPG VECSEL exhibits higher slope efficiency than the 4x3 DWELL sample at a given temperature. The maximum achievable output power (Fig. 4.24) follows the same trend. This is consistent with carrier escape from the DWELL layers due to their higher thermal energy.

Also associated with the change in sample temperature is a redshift of the lasing wavelength. For the RPG structure, spectra were collected just above threshold at a constant pump power of 1.68 W for each temperature, and are shown in Fig. 4.25. Over the 50°C range the laser emission shifted about 7 nm toward longer wavelength. This shift of 0.14 nmK^{-1} is once again in the middle between what would be expected from refractive index change and from the temperature shift of the bandgap energy. Compared to the results from section 4.3.3, however, it seems the index change has larger influence in this experiment.

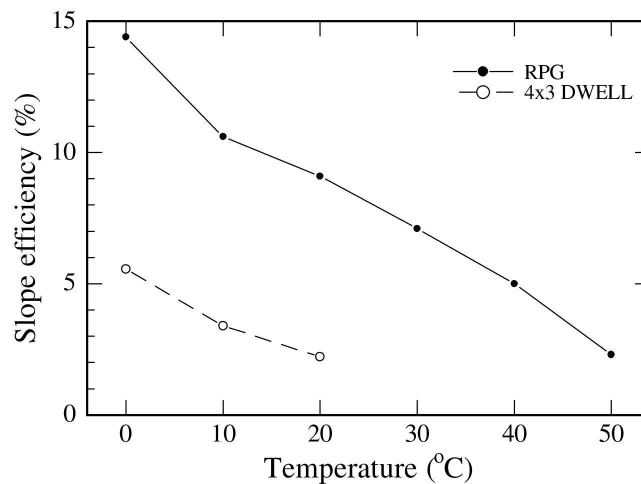

Figure 4.23: VECSEL differential efficiency at different temperatures.

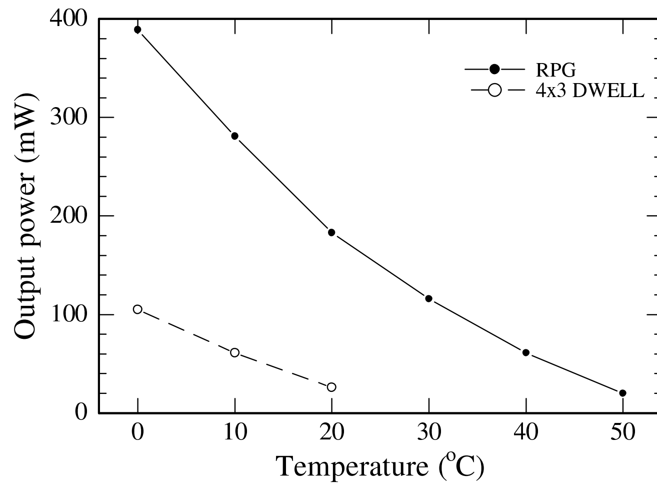

Figure 4.24: Maximum VECSEL output power at different temperatures.

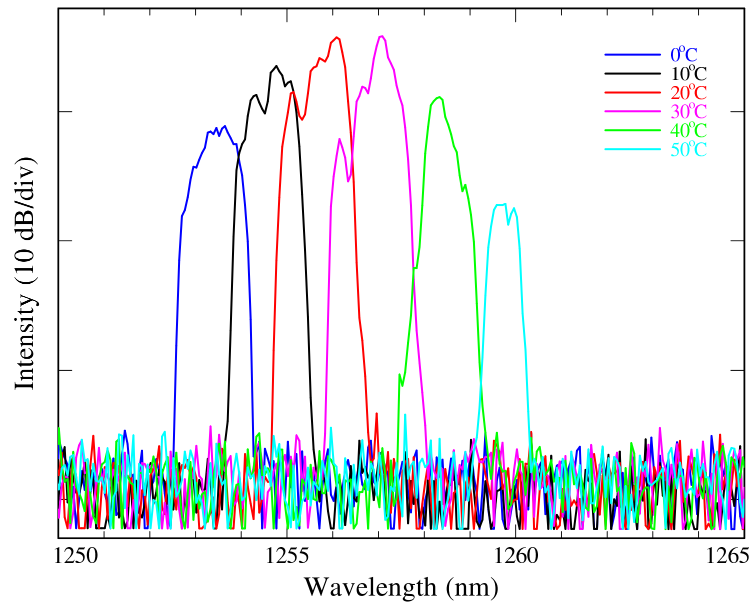

Figure 4.25: Lasing spectra from RPG VECSEL at 1.28 W pump power for different heatsink temperatures.

4.3.7 Tuning by Position on the Wafer

The non-uniformity of the layer thickness and therefore subcavity resonance wavelength across the wafer due to the MBE growth, combined with the large gain bandwidth of the QD active region can be used to tune the VECSEL emission wavelength by moving the pump spot to different areas of the sample.

Lasing spectra were recorded with a spacing of 10 nm and are reproduced in Fig. 4.26 for the 4x3 DWELL VECSEL and Fig. 4.27 for the RPG sample. Both experiments used the 99.0% reflectance external mirror and a heatsink temperature of 0°C.

Output power vs. pump power curves were recorded at each position and are shown in Figs. 4.28 and 4.29. The spectra correspond to the highest output power data point in each curve of the same wavelength (same color in the plots). For the 4x3 DWELL structure, lasing threshold could not be reached at a wavelength of 1220 nm, the RPG VECSEL showed very limited output power as well. Both samples only performed marginally at 1280 nm. A plot of the lasing wavelength as function of the position on the wafer is shown in Fig. 4.30. The x-axis represents the whole wafer from the center at 0 to the edge of the epitaxy area at 35 mm.

The maximum achievable output power for the different positions is shown in Fig. 4.31. As observed before, the RPG sample outperforms the 4x3 DWELL structure by more than a factor of three at any given wavelength. Both samples perform best between 20 mm and 25 mm from the center of the wafer, again explained by the alignment between subcavity resonance and QD gain. The similar behavior of the two VECSELs is indicative of the precisely controlled and highly repeatable MBE growth.

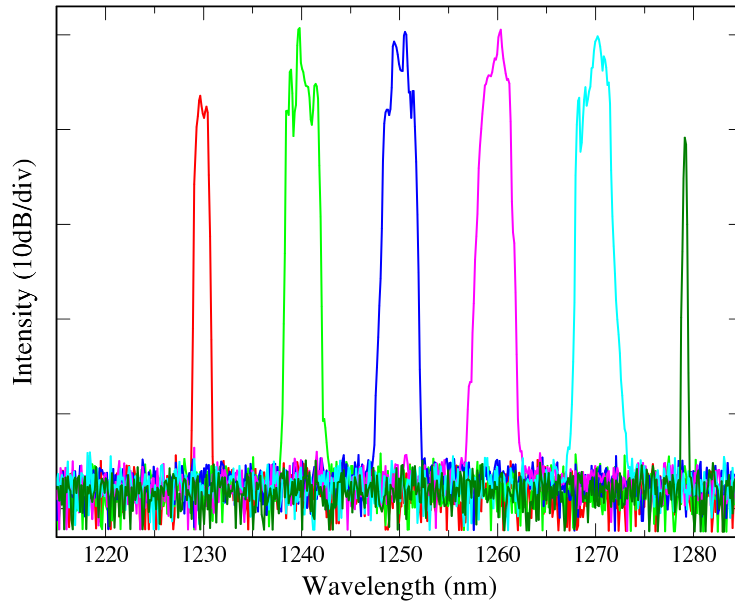

Figure 4.26: VECSEL spectra for different positions across the wafer of the 4x3 DWELL sample.

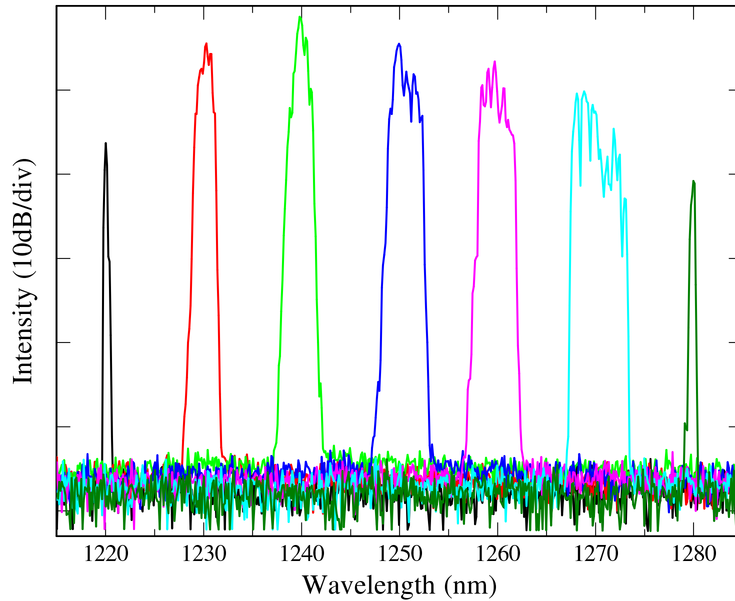

Figure 4.27: VECSEL spectra for different positions across the wafer of the RPG sample.

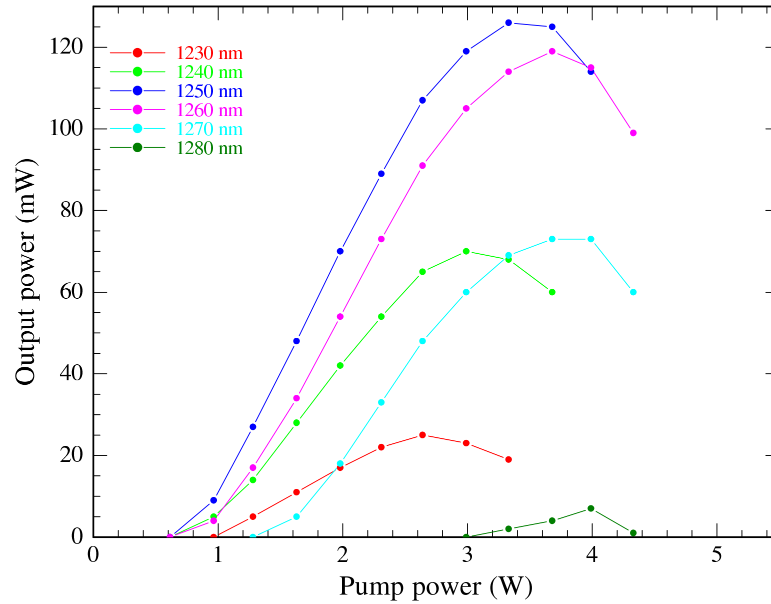

Figure 4.28: VECSEL output power vs. pump power for different positions across the wafer of the 4x3 DWELL sample.

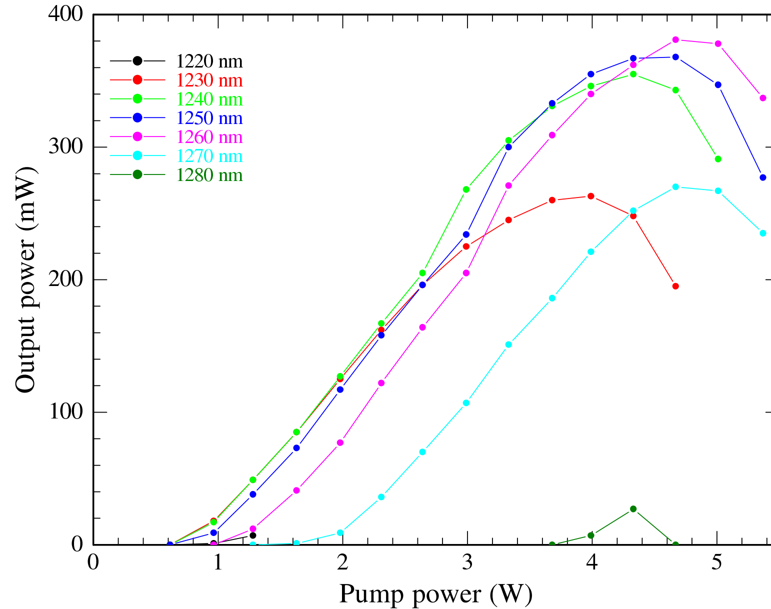

Figure 4.29: VECSEL output power vs. pump power for different positions across the wafer of the RPG sample.

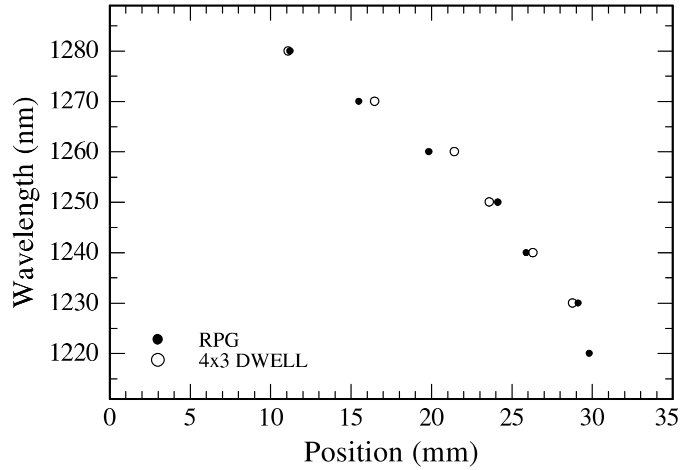

Figure 4.30: VECSEL lasing wavelength as a function of position on the wafer.

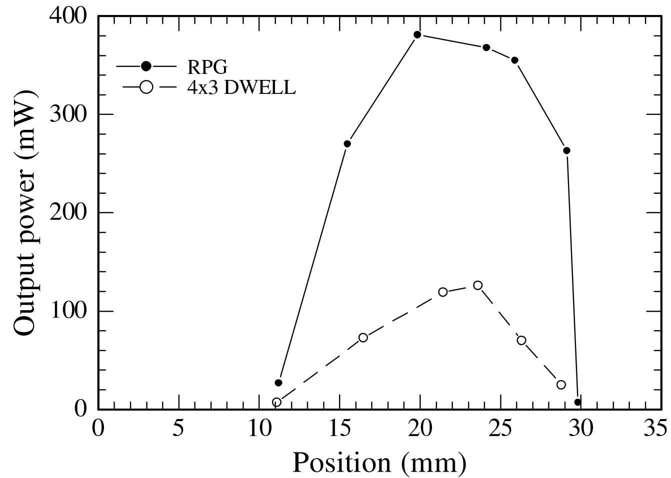

Figure 4.31: Maximum VECSEL output power as a function of position on the wafer.

4.3.8 Intra-Cavity Frequency Doubling

To reach the goal of red emission, a non-linear optical crystal is needed for frequency doubling [26] of the IR output from the QD VECSEL. For our experiments, a β-Barium Borate (BBO) crystal was used. For a fundamental wavelength of 1260 nm and the BBO crystal at room temperature, an angle of $\theta = 20.8°$ [27, 28] is required

for phase-matching. An existing crystal, cut at $\theta = 20.4°$ was utilized instead, at a small angle to the VECSEL cavity, adjusted to maximize SHG. Both surfaces of the BBO were AR coated at 1260 nm and also at 630 nm. For the short wavelength, an HR coating on one facet would be preferable, since any red emission toward the gain mirror will be lost.

The SHG is proportional to the square of the intensity in the fundamental beam, so in order to archive efficient doubling, a small spot size is needed. Without changes to the existing VECSEL cavity (Fig. 4.1), the smallest beam waist is at the gain mirror. However, to prevent obstruction of the pump laser, the non-linear crystal was located approximately 15 mm from the VECSEL sample. To increase the optical power inside the cavity, the 99.5% external mirror was used; ideally a mirror even more reflective at the fundamental wavelength should be used. The position of the output coupler had to be adjusted to account for changes to the cavity due to the BBO.

The cavity was first aligned without the nonlinear crystal in place. The BBO was then introduced and the alignment of the crystal and output coupler was optimized to reach lasing threshold again and then to maximize fundamental output power. After this, the thermal power meter used to measure IR output power was replaced with an integrating sphere with Silicon photo diode. Two short-pass filters were used to block the fundamental emission from reaching the detector when measuring the second harmonic (SH) output power. The two filters resulted in a loss of 20% optical power at 630 nm, which was corrected for in our results. The BBO crystal was now rotated slowly to optimize the phase-matching angle, thereby maximixzing the SH power. Small modifications to the output coupler alignment were needed to correct for the changed optical path due to the rotation of the nonlinear crystal.

Maximizing the red emission resulted in the VECSEL no longer lasing in the lowest order mode. Instead, a higher mode was preferred, with mainly one outer-

most lobe of the mode pattern contributing to the SHG, as schematically shown in Fig. 4.32. This might be explained by the higher intensity of this feature when compared to the lower order mode and the lack of focusing of the light inside the BBO.

Fundamental and SH power (from one facet of the BBO crystal) as function of pump power are shown in Fig. 4.33. The IR output power dropped over 25% when compared to the experiment without the BBO (Fig. 4.13). This is more than expected due to SHG, the rest can be explained by absorption and reflection losses at the non-linear crystal.

The maximum red emission collected from one facet was about 11 mW. The sharper peak of the SH power when compared to the IR power results from the quadratic power dependence of the SHG, as well as the pump-power induced heating, causing a shift of the fundamental wavelength with power, which hinders perfect phase-matching at all pump power levels.

A spectrum of the red emission from the frequency-doubled VECSEL is shown in Fig. 4.34. The slope of the baseline is an artifact from the spectrum analyzer.

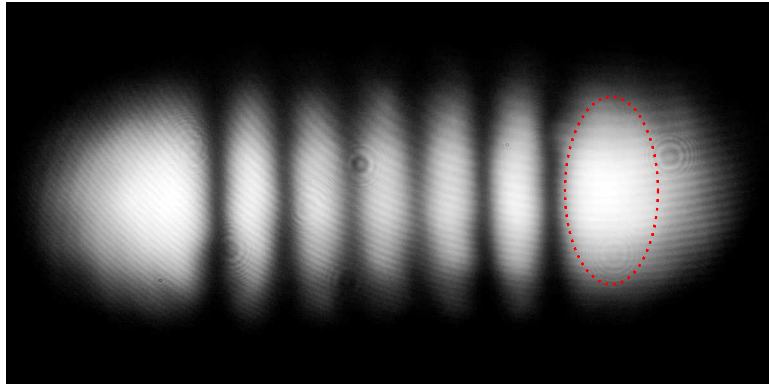

Figure 4.32: Schematic drawing of SHG area overlaid on a photograph of IR lasing mode in the VECSEL cavity without BBO crystal present.

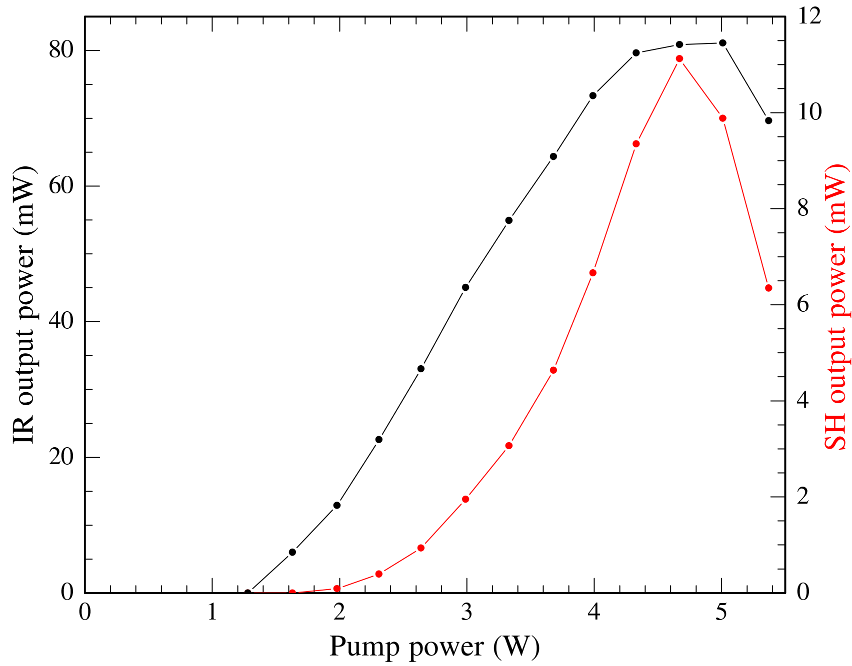

Figure 4.33: VECSEL IR and SH output power vs. pump power for the RPG structure.

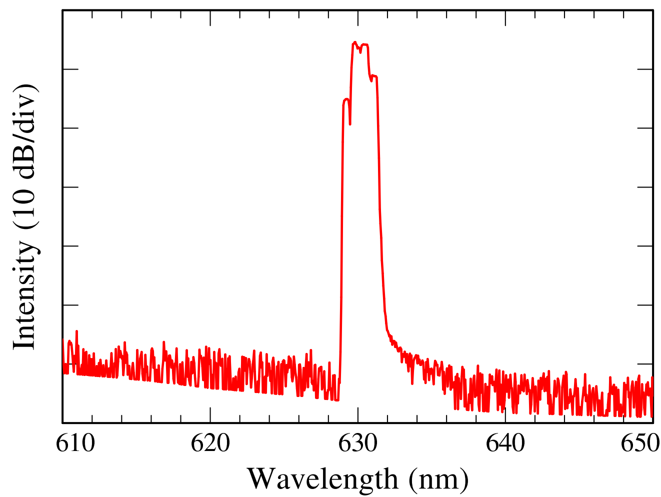

Figure 4.34: Spectrum of SH output at 630 nm.

The efficiency of the SHG could be increased significantly by focusing the beam into the BBO crystal. Using a Z-shaped cavity, formed by three concave dielectric

reflectors (M1, M2, M3) in addition to the gain mirror, as shown in Fig. 4.35 [29, 30], a small beam waist can be located inside the nonlinear material. This focus depends on M1 and M2, but is independent of the pump spot size. This should allow for SH output powers about one order of magnitude higher than demonstrated here. This cavity design would also allow access to a collimated area of the fundamental VECSEL mode between mirrors M2 and M3, which would allow a Fabry-Prot etalon to be used to fix the lasing wavelength, necessary for optimum phase-matching at all pump powers. However, due to a lack of suitable mirrors we did not investigate this further.

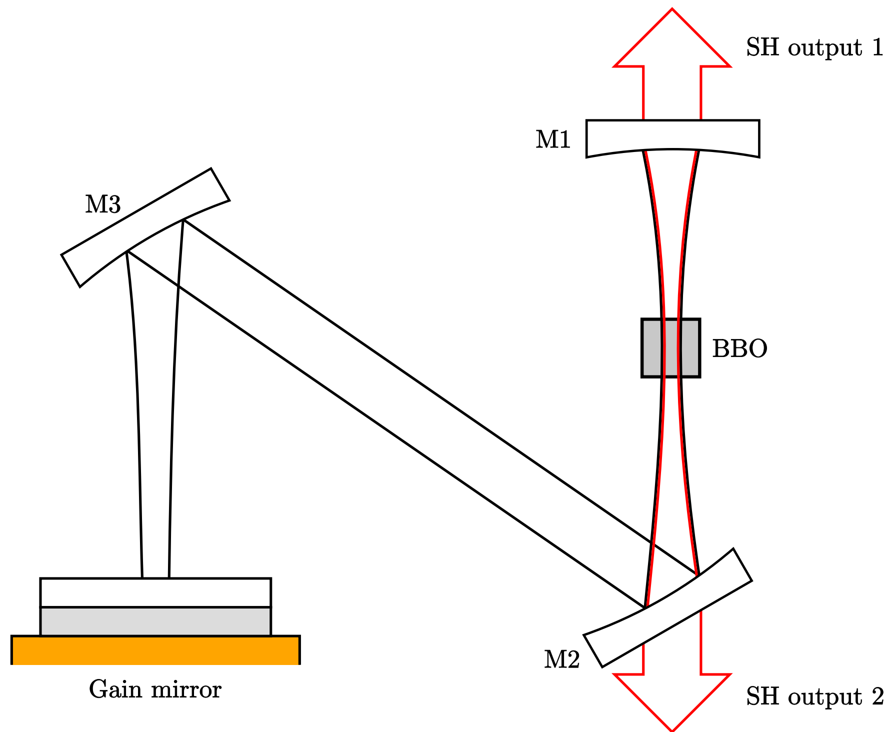

Figure 4.35: Possible VECSEL cavity design for efficient SHG.

4.4 Conclusions

This chapter discussed the design of a QD VECSEL, starting with the gain mirror. Two competing active region designs, one derived from our VCSEL experiments, the other a RPG structure, were discussed. The requirements for the external mirror for different pump sources were discussed and suitable mirrors were chosen based on the calculated values.

The MBE grown structures were first characterized by FITR reflectance and PL emission measurements. VECSEL setups were built for a Ti:Sapphire and high power diode laser pump. The lasing performance of both gain mirrors was compared and found to consistently favor the RPG design. This was attributed to better heatsinking due to the thicker GaAs subcavity when compared to the VCSEL-based design.

Close to 400 mW of output power was achieved, which is the highest reported power from a QD VECSEL with emission wavelength over 1200 nm, despite other researchers using expensive diamond intra-cavity heat spreaders to improve performance. Threshold pump power densities of below 1 $kWcm^{-2}$ were observed, less than half of the previously published record and about one quarter of GaInNAs-based devices, which compete in this wavelength range. The VECSEL output was linearly polarized along the [110] crystal direction.

CW operation over a temperature range from 0 to 50°C was achieved. Thanks to thickness variation across the substrate, lasing operation could be demonstrated from 1220 nm to 1280 nm.

Finally, intra-cavity frequency-doubling was demonstrated using a BBO crystal. Over 10 mW at 630 nm were emitted from one facet of the non-linear material, at a wavelength of 630 nm. To our knowledge, this is the first successful SHG from a QD

VECSEL. Doubling efficiency and output power could be increased significantly by redesigning the cavity to focus the light inside the non-linear crystal.

References

[1] M. A. Hadley, G. C. Wilson, K. Y. Lau, and J. S. Smith. High single-transverse-mode output from external-cavity surface-emitting laser diodes. *Applied Physics Letters*, 63(12):1607–1609, 1993.

[2] M. Kuznetsov, F. Hakimi, R. Sprague, and A. Mooradian. High-power (>0.5-W CW) diode-pumped vertical-external-cavity surface-emitting semiconductor lasers with circular TEM00 beams. *Photonics Technology Letters, IEEE*, 9(8):1063–1065, Aug. 1997.

[3] JunHo Lee, SangMoon Lee, Taek Kim, and YongJo Park. 7 W high-efficiency continuous-wave green light generation by intracavity frequency doubling of an end-pumped vertical external-cavity surface emitting semiconductor laser. *Applied Physics Letters*, 89(24):241107, 2006.

[4] Li Fan, Ta-Chen Hsu, Mahmoud Fallahi, James T. Murray, Robert Bedford, Yushi Kaneda, Jörg Hader, Aramais R. Zakharian, Jerome V. Moloney, Stephan W. Koch, and Wolfgang Stolz. Tunable watt-level blue-green vertical-external-cavity surface-emitting lasers by intracavity frequency doubling. *Applied Physics Letters*, 88(25):251117, 2006.

[5] Jennifer Hastie, Stephane Calvez, Martin Dawson, Tomi Leinonen, Antti Laakso, Jari Lyytikäinen, and Markus Pessa. High power CW red VECSEL with linearly polarized TEM00 output beam. *Opt. Express*, 13(1):77–81, 2005.

[6] VLOC Subsidiary of II-VI Incorporated. Yttrium aluminum garnet laser materials, February 2009. `http://www.vloc.com/PDFs/YAGBrochure.pdf`.

[7] J.-M. Hopkins, S.A. Smith, C.W. Jeon, H.D. Sun, D. Burns, S. Calvez, M.D. Dawson, T. Jouhti, and M. Pessa. 0.6 W CW GaInNAs vertical external-cavity surface emitting laser operating at 1.32 μm. *Electronics Letters*, 40(1):30–31, Jan. 2004.

[8] J. Rautiainen, A. Härkönen, V.-M. Korpijärvi, P. Tuomisto, M. Guina, and O. G. Okhotnikov. 2.7 W tunable orange-red GaInNAs semiconductor disk laser. *Opt. Express*, 15(26):18345–18350, 2007.

[9] A. Strittmatter, T.D. Germann, J. Pohl, U.W. Pohl, D. Bimberg, J. Rautiainen, M. Guina, and O.G. Okhotnikov. 1040 nm vertical external cavity surface emitting laser based on InGaAs quantum dots grown in Stranski-Krastanow regime. *Electronics Letters*, 44(4):290–291, 14 2008.

[10] T. D. Germann, A. Strittmatter, J. Pohl, U. W. Pohl, D. Bimberg, J. Rautiainen, M. Guina, and O. G. Okhotnikov. High-power semiconductor disk laser based on InAs/GaAs submonolayer quantum dots. *Applied Physics Letters*, 92(10):101123, 2008.

[11] T. D. Germann, A. Strittmatter, J. Pohl, U. W. Pohl, D. Bimberg, J. Rautiainen, M. Guina, and O. G. Okhotnikov. Temperature-stable operation of a quantum dot semiconductor disk laser. *Applied Physics Letters*, 93(5):051104, 2008.

[12] J.V. Sandusky and S.R.J. Brueck. A CW external-cavity surface-emitting laser. *Photonics Technology Letters, IEEE*, 8(3):313–315, March 1996.

[13] A. Garnache, A. A. Kachanov, F. Stoeckel, and R. Houdré. Diode-pumped broadband vertical-external-cavity surface-emitting semiconductor laser applied to high-sensitivity intracavity absorption spectroscopy. *J. Opt. Soc. Am. B*, 17(9):1589–1598, 2000.

[14] Frank H. Peters and W.L. Gore and Associates. Vertical Version 1.1 Beta, 1996.

[15] M. Y. A. Raja, S. R. J. Brueck, M. Osinski, C. F. Schaus, and J. G. McInerney. Novel wavelength-resonant optoelectronic structure and its application to surface-emitting semiconductor lasers. *Electronics Letters*, 24:1140–1142, September 1988.

[16] Brigham Young University. Optical absorption coefficient calculator, February 2009. `http://www.ee.byu.edu/cleanroom/OpticalCalc.phtml`.

[17] E. D. Palik. *Handbook of optical constants of solids*. Academic Press Handbook Series, New York: Academic Press, 1985, edited by Palik, Edward D., 1985.

[18] Joseph T. Verdeyen. *Laser Electronics*. Prentice-Hall, Englewood Cliffs, N.J. :, 1995.

[19] Y. Li, Y. C. Xin, H. Su, L. F. Lester, A. L. Gray, S. Luong, K. Sun, Z. Zou, and J. Zilko. Photoluminescence characterization of quantum dot laser epitaxy. In D. L. Huffaker and P. K. Bhattacharya, editors, *Society of Photo-Optical Instrumentation Engineers (SPIE) Conference Series*, volume 5734 of *Society of Photo-Optical Instrumentation Engineers (SPIE) Conference Series*, pages 138–145, April 2005.

[20] W. Diehl, P. Brick, B. Kunert, S. Reinhard, K. Volz, and W. Stolz. Low threshold 1260 nm (GaIn) (NAs) semiconductor disk laser. *Applied Physics Letters*, 91(7):071103, 2007.

[21] Saulius Marcinkeviius. Dynamics of Carrier Transfer into In(Ga)As Self-assembled Quantum Dots. In *Self-Assembled Quantum Dots*, volume 1 of *Lecture Notes in Nanoscale Science and Technology*, pages 129–163. Springer New York, 2008.

[22] V. Daneu, A. Sanchez, T. Y. Fan, H. K. Choi, G. W. Turner, and C. C. Cook. Spectral beam combining of a broad-stripe diode laser array in an external cavity. *Opt. Lett.*, 25(6):405–407, 2000.

[23] M. E. Straumanis, J. P. Krumme, and M. Rubenstein. Thermal expansion coefficients and lattice parameters between 10° and $65°C$ in the system GaP-GaAs. *Journal of The Electrochemical Society*, 114(6):640–641, 1967.

[24] Thomas J. Rotter. *Growth and properties of self assembled InAs quantum dash laser active regions*. PhD thesis, The University of New Mexico, July 2007.

[25] Gyoungwon Park, O.B. Shchekin, and D.G. Deppe. Temperature dependence of gain saturation in multilevel quantum dot lasers. *Quantum Electronics, IEEE Journal of*, 36(9):1065–1071, Sep 2000.

[26] P. A. Franken, A. E. Hill, C. W. Peters, and G. Weinreich. Generation of optical harmonics. *Phys. Rev. Lett.*, 7(4):118–119, Aug 1961.

[27] D.A. Roberts. Simplified characterization of uniaxial and biaxial nonlinear optical crystals: a plea for standardization of nomenclature and conventions. *Quantum Electronics, IEEE Journal of*, 28(10):2057–2074, Oct 1992.

[28] Arlee Smith. Snlo v44, January 2009. `http://www.as-photonics.com/SNLO`.

[29] Antti Härkönen, Jussi Rautiainen, Mircea Guina, Janne Konttinen, Pietari Tuomisto, Lasse Orsila, Markus Pessa, and Oleg G. Okhotnikov. High power frequency doubled GaInNAs semiconductor disk laser emitting at 615 nm. *Opt. Express*, 15(6):3224–3229, 2007.

[30] M. Jacquemet, M. Domenech, G. Lucas-Leclin, P. Georges, J. Dion, M. Strassner, I. Sagnes, and A. Garnache. Single-frequency cw vertical external cavity surface emitting semiconductor laser at 1003 nm and 501 nm by intracavity frequency doubling. *Applied Physics B: Lasers and Optics*, 86:503–510, February 2007.

Chapter 5

Conclusions

Self-assembled InAs QDs have been very successfully employed in edge-emitting semiconductor lasers to extend the emission wavelength of GaAs based devices to 1300 nm. In this dissertation, we investigated the use of QDs in surface-emitting lasers. There are several challenges to overcome in the design of VCLs with QD active regions: The extremely short cavity length in the vertical direction combined with the small dimensions and areal density of the QDs result in very low available gain. To overcome this, the number of quantum dot layers needs to be increased compared to the case of facet-emitting lasers. However, because of the larger lattice constant of InAs grown on the GaAs substrate, too much InAs will result in increased strain, lowering the crystalline quality of the semiconductor material.

A second important design parameter is the reflectivity of the cavity mirrors used in the device. Typically, reflectance values over 99% are needed, which is achievable with multi-layer DBR designs. We investigated the properties and manufacturability of dielectric, selectively oxidized, and all semiconductor mirrors. Experiments with dielectric DBRs were limited, due to the poor material quality and low damage threshold. Mirrors formed by selective oxidation of AlAs allow for very reasonable

MBE growth times, but require additional processing; the design, operation, and characterization of the wet oxidation system were discussed. AlAs/GaAs semiconductor DBRs can be employed as-grown, but the larger thickness results in additional challenges during MBE growth.

Our development of QD VCSELs began with an optically pumped structure, requiring only simple processing to form the oxide DBRs. Lasing operation at room temperature was achieved, with an emission wavelength of 1310 nm.

For electrically injected VCSEL devices, an elaborate design was utilized to allow for selective oxidation of top and bottom DBR and formation of a current aperture in a single wet oxidation step. Since oxide mirrors are not electrically conducting, current was supplied via two intra-cavity contacts, requiring doping and metal contacts close to the QD active region. We believe the diffusion of Be doping may have caused electrical problems as well as a shift of the gain peak away from the cavity mode wavelength. This may be to blame for the lack of success with this device design.

Semiconductor DBR VCSEL structures with an increased number of QD active layers at slightly shorter wavelength were designed and grown. The simplified processing resulted in devices with output powers close to 1 mW at room temperature, and a lasing wavelength between 1200 nm and 1240 nm. Device threshold currents below 250 μA were observed. Threshold current densities below 500 A/cm^2 for larger area devices are believed to be the lowest reported for QD and QW VCSELs in this wavelength range. The low thresholds are likely a result of the reduced density of states in the QD active region.

By replacing the top DBR with an external mirror, a VECSEL is created. This allows for a larger in-plane area of the lasing mode, enabling increased output powers compared to VCSELs, while still retaining the excellent beam characteristics. Two

different active region designs with twelve DWELL layers each, grown on top of an all semiconductor DBR, were investigated. Even without the use of an expensive diamond intra-cavity heat spreader, close to 400 mW of output power around 1260 nm was achieved in CW operation, which we believe to be the highest reported power from a QD VECSEL with emission wavelength over 1200 nm.

Since a VECSEL allows one to access the inside of the laser cavity, a BBO crystal can be used to frequency-double the QD emission. First experiments resulted in over 10 mW of visible light at 630 nm, the ideal wavelength for the red channel of full-color laser projectors. We believe this to be the first demonstration of SHG from a QD VECSEL. The efficiency of frequency conversion could be improved significantly with a different cavity design. Also, QD VECSELs are promising for mode-locking, due to the wide emission spectrum from the non-uniform QD size distribution.

Appendix A

ICP Reflectance Monitor

A.1 Introduction

The processing of semiconductor devices oftentimes involves etching off one or multiple layers of the epitaxial layer structure, usually only in certain parts of the device as defined by photolithography. Typically, the etch depth needs to be well controlled to enable good device performance. In some cases, if the material composition changes at the required depth, a selective wet-chemical etch can be used [1]. However, for multi-layer structures like DBRs, this becomes very tedious, and for small features undercutting can become a problem.

Dry etch processes, on the other hand, have little or no selectivity for the semiconductor material composition. To overcome this limitation, several approaches for monitoring dry etch progress have been explored: One can monitor the chemical composition of the etch products by mass spectroscopy [2] or optical emission spectroscopy [3]. Unfortunately, these techniques have a few drawbacks, like high cost, slow response (limited by diffusion of etch products and memory effect in the chamber), and a fairly large amount of material required to obtain a detectable sig-

nal. A different approach is to use optical techniques like laser interferometry [4] or reflectometry, and ellipsometry [5]. The latter requires optical access from two sides of the etch chamber as well as many expensive optical and mechanical components and is therefore not easy to implement.

Laser interferometry only requires access perpendicular to the sample surface. Two laser beams are sent to the sample, one onto an area that is being etched, and a reference beam on a protected area (e.g. PR). The resulting interference signal is detected and are monitored. This technique works for any material structure but requires precise alignment. Problems arise if the surface at which the reference beam gets reflected is also attacked by the etch, which is the case for almost all mask materials commonly used. Even if this can be prevented, the resolution of this technique is limited, since the difference in optical path length is simply the step height of the etch in air ($n = 1$), so a resolution on the order of a quarter of the laser wavelength is realistic.

A.2 Reflectometry

Laser reflectometry can overcome most of these limitations for a large variety of situations. It only requires perpendicular optical access as a single laser beam is sent to the sample, where it is partially reflected at the sample surface and also by any changes in index of refraction (layer composition) inside the sample, which is schematically shown in Fig. A.1. Only interfaces close enough to the sample surface can produce a signal, at greater depth all of the incoming light has been absorbed or reflected already. While this rules out any sample with thick layers of uniform composition, this technique has several advantages: Since the interference is caused by the difference in optical path length inside the semiconductor, the resolution is on the order of $\lambda/4\mathrm{n}$, with $\mathrm{n} \approx 3$ for AlAs/GaAs devices. In addition, anytime an

interface with a change in index of refraction surfaces during the etch, the reflectance signal changes as well, allowing even layers much thinner than the laser wavelength to be observed. Reliable monitoring of 0.5 nm thick GaInPAs QWs in InP has been reported [6], using a wavelength of 670 nm. The technique is so powerful that it is even used for realtime-monitoring of MBE and MOCVD growth [7].

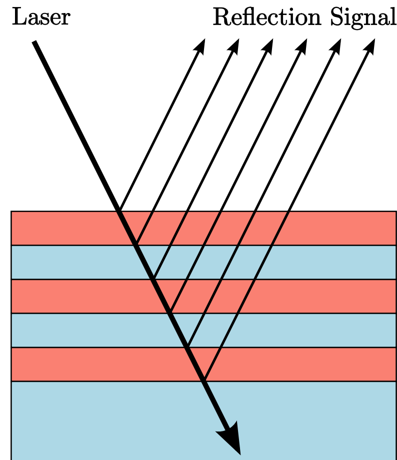

Figure A.1: Schematic diagram of laser beam reflected of sample surface and internal interfaces. Note that the actual measurement is performed under normal incidence, the angle was added for clarity.

A.3 Experimental Setup

A reflectance monitor was set up for CHTM's PlasmaTherm ICP etcher, a schematic diagram of the system in shown in Fig. A.2. A laser diode module with an emission wavelength of 650 nm and output power of 1 mW is mounted on a two-axis translation stage on top of the ICP chamber. The beam passes through a non-polarizing beam splitter cube and through a window into the chamber and onto the sample. The reflected light passes back out through the same window and is partially reflected by the beam splitter onto a silicon photo diode. The laser power is square-wave

modulated at a frequency of approximately 200 Hz so the detector output can be detected with a lock-in amplifier, largely rejecting the influence of room lights or the plasma inside the chamber. The signal from the lock-in as a function of time is plotted in real-time with a computer program. As the system has not been interfaced with the ICP control computer, it is left up to the user to end the etch process once the reflectance signal indicates the required etch depth when compared to a simulation.

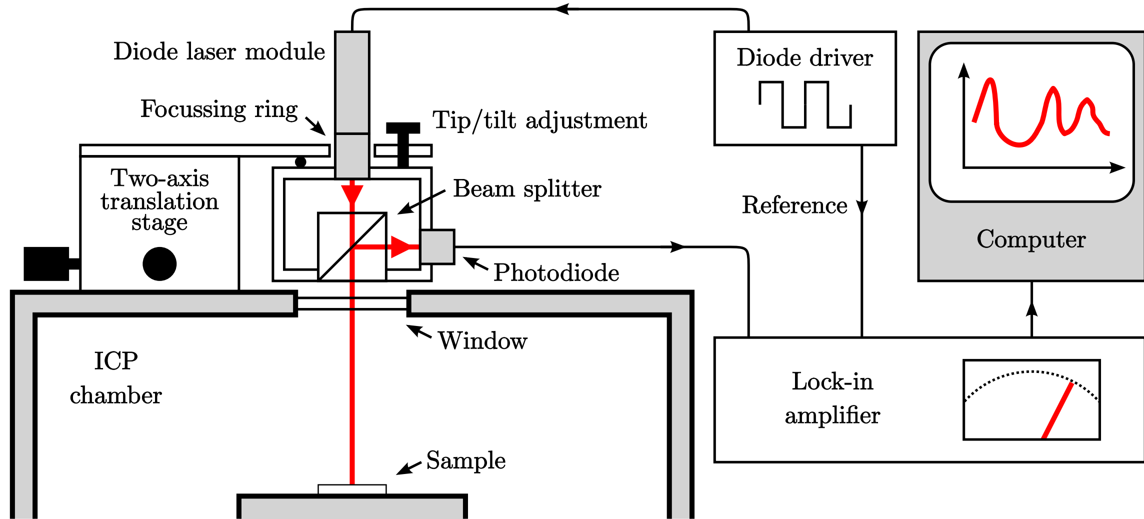

Figure A.2: Schematic diagram of ICP reflectance monitor.

A.4 Examples

In this section, a few examples of reflectance measurements during ICP etches are shown, with additional details provided in the figure captions. Any simulations included were prepared using the software “Vertical” [8].

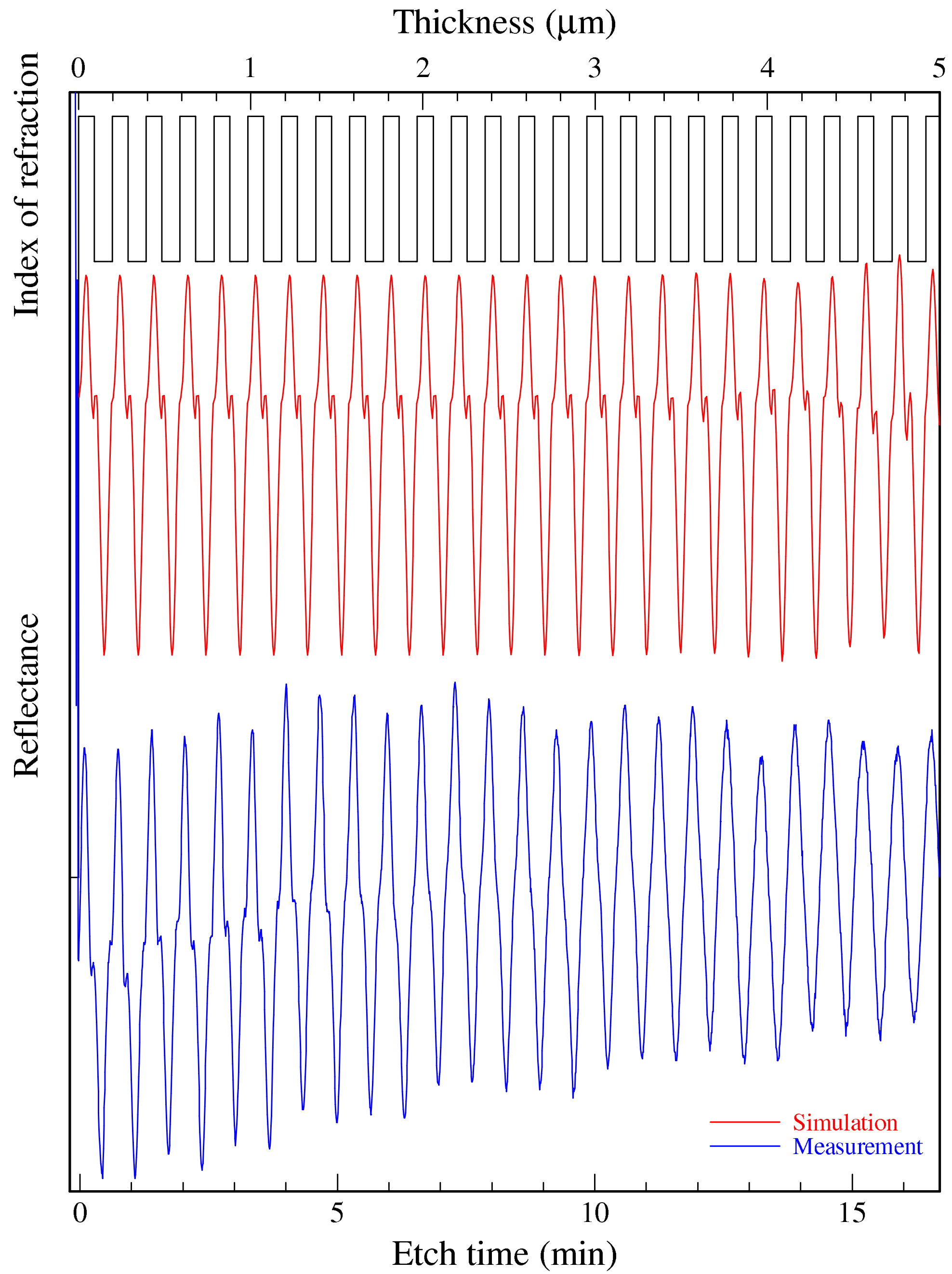

Figure A.3: 26 AlAs/GaAs DBR pairs designed for a wavelength of 1250 nm showing non-uniformity of layer thickness due to drift in MBE growth rates.

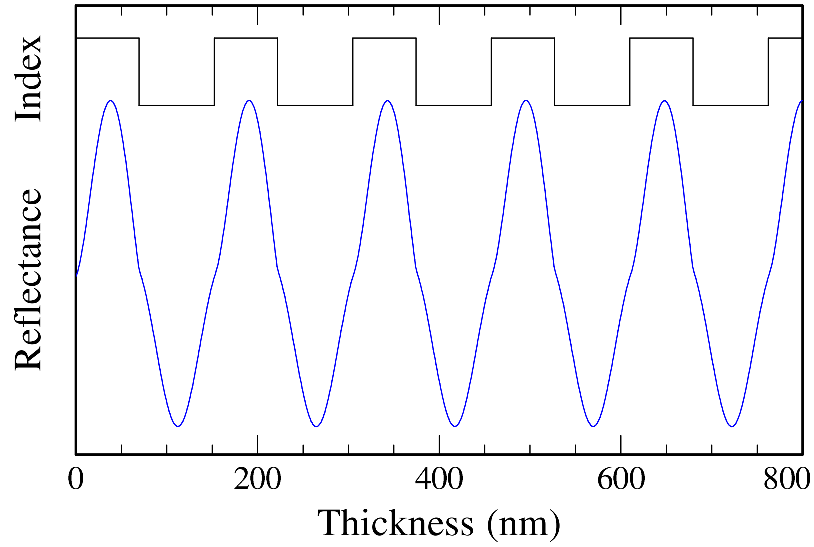

Figure A.4: Simulation for AlAs/GaAs DBR designed for 980 nm.

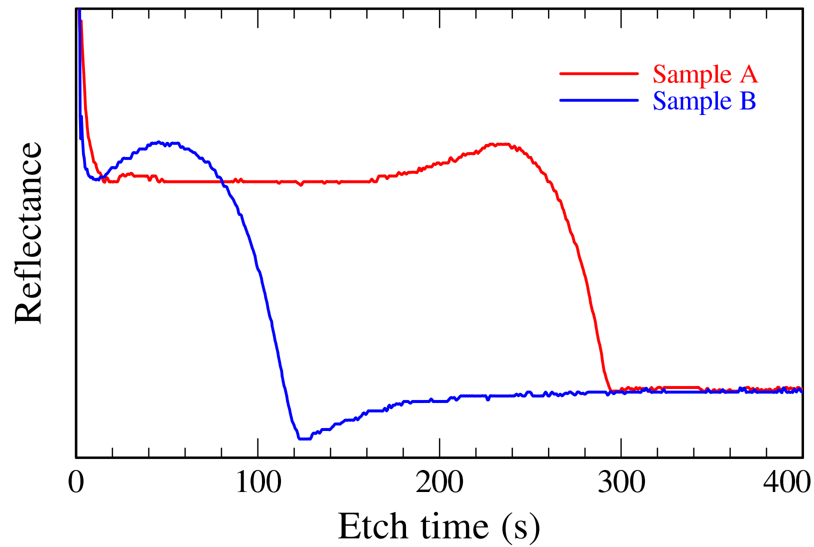

Figure A.5: Reflectance measurements from etching two different thickness MnAs layers on top of GaAs substrate. While no simulation was available, it seems quite clear, where the metallic MnAs layer ends and the substrate starts. Also, since sample A requires a longer etch, it can be inferred that its MnAs thickness is greater than in sample B.

A.5 Standard Operating Procedure

1. Turn on power strip behind computer cart.
2. Turn on computer (∇ on keyboard).
3. Turn on lock-in amplifier.
4. Turn on laser with switch on diode driver.
5. Follow regular ICP procedures to load your sample and start the batch process.
6. Wait for the sample to be moved into the process chamber and the clamp to lock it it place.
7. Using the x/y-stage, move the laser beam onto your sample, you should see two red spots on the window (laser going in, reflected signal coming out).
8. Check if the two spots are the same size, adjust focus by turning the laser module if necessary.
9. Using the tip/tilt adjustment, overlap the two spots on the window.
10. Watching the signal on the lock-in amplifier, maximize the amplitude by carefully adjusting to the tip/tilt mount.
11. Using the x/y-stage, move the laser spot to the position on your sample where you want to measure the etch progress. Make sure to avoid any areas covered by PR or metal.
12. Open the ICP Labview program on the desktop and start it.
13. Set the desired time interval for measurement. One second is good for most cases.
14. Wait for the ICP pump-and-purge cycles to end.

15. While the process gas mixture stabilizes (starting 60 seconds before the etch) push the reset and then the start button in the ICP Labview program.

16. Watch the reflectance signal on the monitor and compare it to your simulation to determine when to stop the etch process.

17. After the process has ended, stop the recording and save the reflectance measurement.

18. If you have other samples to etch, go to step 5.

19. Close the ICP Labview program and shut down the computer (click on desktop, then chose “Special” and “Shut down”).

20. Turn off laser with switch on diode driver.

21. Turn off lock-in amplifier.

22. Turn off power strip behind computer cart.

23. Under “Remarks” in the ICP log sheet, include “Refl. setup”.

References

[1] Clawson A.R. Guide to references on III-V semiconductor chemical etching. *Materials Science and Engineering: R: Reports*, 31:1–438(438), 15 January 2001.

[2] Fidorra F Schmid H and Grtzmacher D. *Gallium Arsenide and Related Compounds 1988 (Inst. Phys. Conf. Ser. 96)*. ed J Harris (Bristol: Institute of Physics), 1989.

[3] P. Collot, T. Diallo, and J. Canteloup. Dry-etch monitoring of III–V heterostructures using laser reflectometry and optical emission spectroscopy. *Journal of Vacuum Science & Technology B: Microelectronics and Nanometer Structures*, 9(5):2497–2502, 1991.

[4] M. Sternheim, W. van Gelder, and A. W. Hartman. A Laser Interferometer System to Monitor Dry Etching of Patterned Silicon. *Journal of The Electrochemical Society*, 130(3):655–658, 1983.

[5] Roland Müller. In situ etching depth monitoring for reactive ion etching of InGaAs(P)/InP heterostructures by ellipsometry. *Applied Physics Letters*, 57(10):1020–1021, 1990.

[6] A Stano, C Coriasso, and G Meneghini. High-resolution depth monitoring of reactive ion etching of InP/InGaAs(P) MQWs using reflectance measurements. *Semiconductor Science and Technology*, 11(6):968–973, 1996.

[7] W.G. Breiland. In situ reflectance monitoring of epitaxial growth. *Electronic-Enhanced Optics, Optical Sensing in Semiconductor Manufacturing, Electro-Optics in Space, Broadband Optical Networks, 2000. Digest of the LEOS Summer Topical Meetings*, pages II19–II20, 2000.

[8] Frank H. Peters and W.L. Gore and Associates. Vertical Version 1.1 Beta, 1996.

Appendix B

Oxidation Furnace Standard Operating Procedure

The following procedure was used for Al(Ga)As wet oxidation using the Thermco furnace installed in CHTM room 132 (cleanroom chase):

Startup

- Make sure both glass flasks in the exhaust lines are empty. One is located on the right side behind the furnace, the other one on the left of the shelf.
- Make sure the relief valve is open. It is located on the left of the shelf.
- Check water level in the bubbler flask in the bottom shelf left of the furnace. It should be filled approximately to the black mark on the glass.
- If you need to refill DI water: Open the cap on the refill line. Slowly pour in DI water, check that it does not flow into the nitrogen line to the left. Carefully tighten the cap, slightly more than hand-tight.

- Check fluid level in the heat bath. Open the little lid next to the heater. The level should be slightly below the lowest part of the metal on the left. Refill with ethylene glycol:water 70:30.

- Turn on heat bath by switching on the power strip on the shelf. Do not adjust the settings of the bath. This also provides power to the heat tape around the exposed part of the tube.

- Turn on nitrogen supply with the valve on the wall left of the furnace (flow = 14.5). With the compressed air valve on the furnace closed, this allows dry nitrogen to flow through the tube.

- Turn on the furnace cooling fan using the switch attached to the lower right of the furnace.

- Turn on the main power disconnect on the wall left of the furnace. Do not lean on or bump into the shelf with the bubbler as it might break the bubbler flask or the glass tube of the furnace.

- Check the zone settings on the left ANA-Lock controller on the furnace (see table B.1).

- Turn on the controller power. Wait till the instruments are steady.

- Turn on the zone breakers.

- Wait two hours for the furnace and heat bath temperature to stabilize.

- Check heat bath temperature (95°C).

- Check furnace temperature.

- Set MAIN switch to ON and leave the VALVE switch on PURGE.

- Close the relief valve.

- Turn on compressed air supply with the green valve on the front of the shelf.
- Open compressed air valve. This switches the nitrogen flow from the tube to the bubbler.
- Set VALVE switch to FLOW. This sends steam from the bubbler into the tube. Check the nitrogen flow (10).
- Wait 30 minutes to allow the steam lines from the bubbler to the tube to warm up.
- Set VALVE switch to PURGE. This sends the steam into the exhaust.
- Close compressed air valve. This switches the nitrogen flow from the bubbler to the tube.
- Pull boat to the end of the furnace but not out into the exposed part of the tube.
- Wait 5 minutes for the boat to cool down a little and the tube to dry.

Oxidation

1. Load sample. Be careful: The boat, tube and glass rod are hot.
2. Push boat into the center of the furnace as marked on glass rod.
3. Wait 14 minutes for the boat and sample to get to temperature.
4. Open compressed air valve. This switches the nitrogen flow from the tube to the bubbler.
5. Wait 1 minute for the steam to stabilize.
6. Set VALVE switch to FLOW. This sends steam from the bubbler into the tube.

7. Run for the desired time.

8. Set VALVE switch to PURGE. This sends the steam into the exhaust.

9. Close compressed air valve. This switches the nitrogen flow from the bubbler to the tube.

10. Wait 10 minutes to get a more uniform oxidation.

11. Pull boat to the end of furnace but not out into the exposed part of the tube.

12. Wait 5 minutes for the boat and sample to cool down a little.

13. Unload sample. Be careful: The boat, tube and glass rod are hot.

14. Go to step 1 for further samples.

Shutdown

- Turn off heat bath.
- Open the relief valve.
- Set MAIN switch to OFF.
- Turn off the zone breakers.
- Turn off the controller power.
- Turn off the main power disconnect.
- Wait 3 hours while the tube is being purged with dry nitrogen.
- Turn off nitrogen.
- Turn off the furnace cooling fan.

ANA Lock controller			Temperature (°C)
Left	Center	Right	
550	003	465	425
550	018	465	440
550	034	465	450
550	055	465	470
550	090	465	500
550	100	465	520
550	110	465	525

Table B.1: Historical documents suggest that these temperature controller setting result in the given temperatures, with good uniformity throughout the furnace.

Appendix C

Silicon CCD Spectral Response

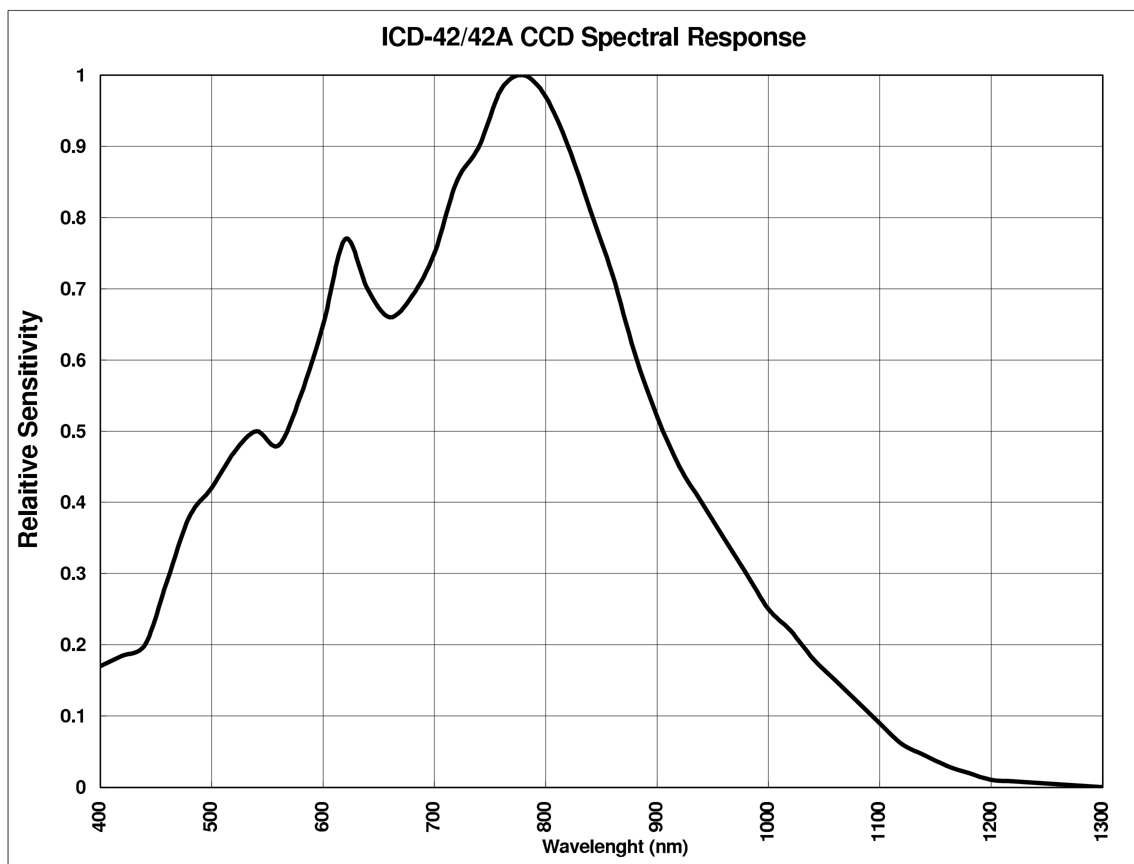

Figure C.1: Spectral response of Si CCD used in the Ikegami ICD-4220 camera.